PHORESIS OF A SOLID PARTICLE IN REAL FLUID

by

YUAN TING WU

Presented to the Faculty of the Graduate School of

The University of Texas at Arlington in Partial Fulfillment

of the Requirements

for the Degree of

DOCTOR OF PHILOSOPHY

THE UNIVERSITY OF TEXAS AT ARLINGTON

August 2015

Acknowledgements

I would like to express my deep gratitude to Professor Bo Yang, my research supervisor, for his patient guidance and enthusiastic encouragement of my entire doctoral study. I would also like to thank Dr. Yiping Zhao and Dr. Manoj Manjare for their inspiration and insight for this work. My grateful thanks are also extended to Dr. Hao Jiang and Mrs. Hongsheng Wang for their professional help and co-work within our lab.

Finally, I wish to thank my family and Pan Hsuan Huang for their support and encouragement throughout my years at U.T. Arlington.

November 24, 2014

Abstract

PHORESIS OF A SOLID PARTICLE IN REAL FLUID

Yuan Ting Wu, PhD

The University of Texas at Arlington, 2014

Supervising Professor: Bo Yang

For micro- and nano-scale particles driven by interfacial non-contact forces in fluid, known as phoresis, this dissertation provides a general formulation and a systematic investigation. It starts with an analytical continuum-mechanics formulation that covers various important aspects of an interfacial structure, including viscosity and mass density variations as well as a body force field, in real fluid. It then reduces to specific solutions due to characteristic mechanisms. A closed-form analytical solution to the case of viscosity variation (which manifests itself as Navier's slip boundary condition) is derived. Furthermore, a novel mechanism for thermophoretic mobility driven by near-surface phase transition is introduced. It is shown that when a particle adsorbs a liquid film around its surface, and when the liquid flows along the surface due to osmosis, normal vapor fluxes in and out of the liquid film are generated. It can result in a term of thermophoretic motility inversely scaled with particle size, in contrast to classical terms with a scaling law either constant or linear with particle size. It means that this new mechanism can be powerful, especially to propel nanoparticles, as demonstrated numerically with the water-steam system modeled by using a continuum equation of state. Last, the interfacial structure of water at a solid surface is examined by using molecular dynamics simulation. It reveals interesting features that are not predicted by the above equation-of-state approach, especially in the case of a hydrophilic surface where water

strongly interacts with the surface. For example, there appears to be significant anisotropic pressure in the interfacial zone, which relates to the interfacial tension. It is shown that the thermophoretic mobility due to the anisotropic pressure is as important as that of interfacial body forces with the same scaling law.

Table of Contents

List of Figures

List of Tables

Chapter 1

Introduction

1.1 Challenges in Propelling Micro/Nanoscale Motors/Robots in Fluid

Transport of colloidal particles in micro/nano fluid has been an active research area for the recent decades. It can find important applications in biological systems, such as transports of nutrition, chromosome, and protein, which are vital to sustaining the lives. Meanwhile, micro/nanoscale artificial motors/robots have been fabricated, which mimic the life forms. The micro/nano fluidic transport can find applications in such devices for biomedical treatments, such as precise drug delivery, functionalized marker, sensing, and missionary particle/robot tasking.

Powering and propelling a micro/nanoscale motor immersed in fluid are always challenging. The reason is that the drag from the fluid environment is linearly scaled with particle size meanwhile the power typically follows a higher-order scaling law. For example, the typical drag coefficient of a spherical particle at low Reynolds number is $6\pi\eta a$ where η is the fluid viscosity and a is the particle radius that makes the drag coefficient scales with a. In contrast, assuming that the power propelling the particle is from a magnetic source and scales with its volume, which is $\frac{4}{3}\pi a^3$, the speed of this particle would scale with a^2. It implies that a 1 μm particle would be a million times slower than a particle of size 1 mm. Even if we consider the case of electrical power source from surface charges where the speed scales with the particle radius, it is still a thousand times slower. Thus, directly pushing or pulling a device is not viable.

Another challenge is inherent in the scallop theorem (Purcell 1977). The Scallop theorem states that in order to achieve propulsion by body motion at low Reynolds number in Newtonian fluids a swimmer must perform in a way that is not invariant under time-reversal. As in its name, for example, a scallop-like structure that only opens and closes reciprocally with two rigid components will only move back and forth at the same place. It is because of the nature of

low Reynolds number hydrodynamics. The Reynolds number is a dimensionless measure of the relative importance of inertia and viscosity effects. It is defined as $Re = \frac{\rho UL}{\eta}$, where ρ is the fluid density, U is the characteristic fluid velocity, L is the characteristic geometry size, and η is the fluid viscosity. Usually, micro- and nano-scale particles and artificial motors that are immersed and move in typical viscous fluid are at low Reynolds number, in which the inertia effect is much smaller than the viscosity effect. Consequently, the Navier-Stokes equation reduces to the linear Stokes creeping flow theory. In this case, an invariant reciprocal motion would cause the device to cancel all the effects and to revolve around the original position.

Therefore, as evidenced by the natural selection, as shown in Figure 1-1, microorganisms and nano- and micro-scale organelles in living systems have to choose either a flexible moving part to propel themselves around the scallop theorem, or other mechanisms that require no body motion. Flagella and cilia are the most common ways that cells use to propel themselves. Having a flagellum means that the cell rotates its whip-like tail to move. A cilium is shorter than a flagellum but works similarly to generate motility essential to lives.

Since rotation is the only way that a rigid body can achieve propulsion without constraint by the scallop theorem, many researchers tried to develop devices mimicking the structure of a flagellum. The micro- and nano-structure can be built by different ways, such as etching (Zhang, Abbott et al. 2009), atom deposition (Gibbs and Zhao 2009), or self-assembled micro-/nano-particles (Dreyfus, Baudry et al. 2005). Flexible structures can also be achieved (Dreyfus, Baudry et al. 2005), but apparently this is more difficult. When using body motion to propel a micro/nanoscale motor, generally, an external powering source is required, such as a magnetic field. Thus, the device, as a receiver, will receive power that scale with its volume as a^3. As mentioned above, it would generally lead to the particle speed scaling with a^2 and slowing down rapidly when downsizing.

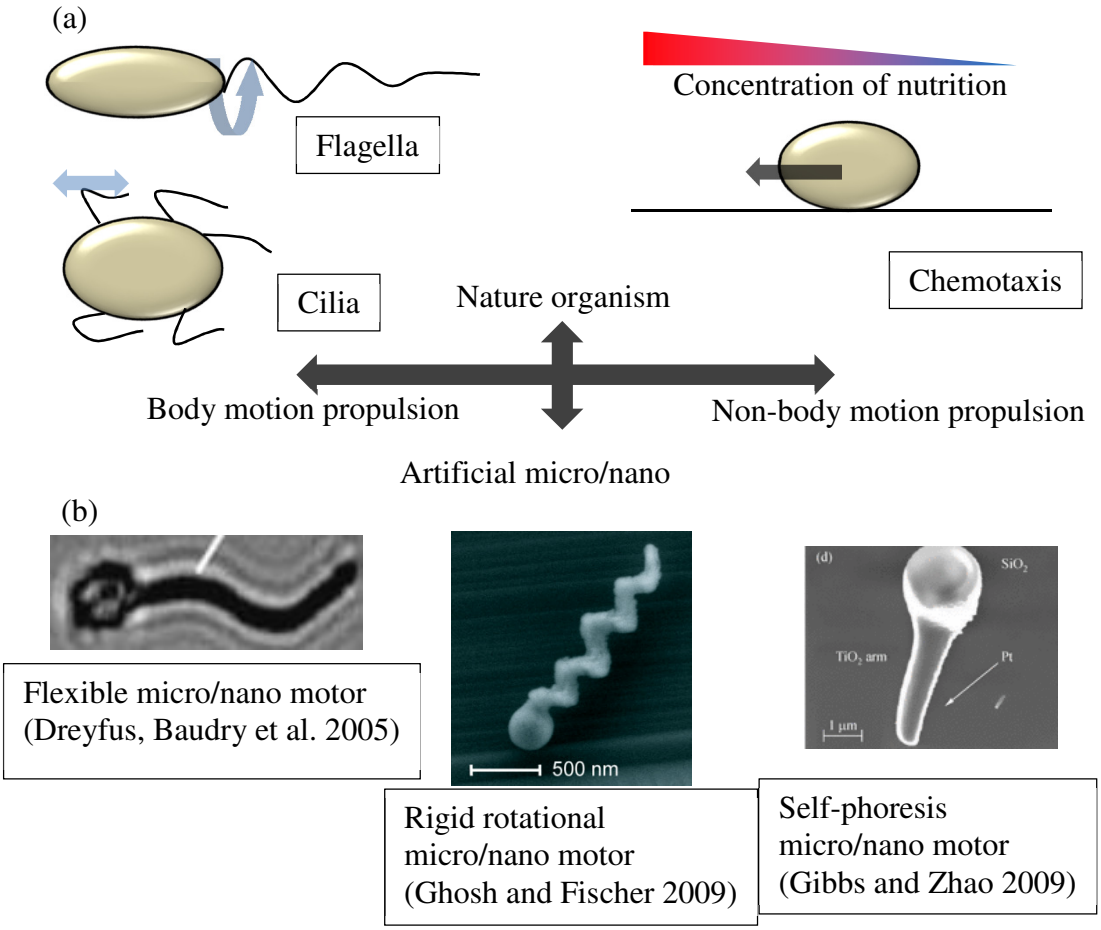

Figure 1-1 Illustration of different approaches of (a) micro/nanoscale living body moving, (b) associated artificial propulsion method that mimic the nature live

Among the approaches not using body motion, most involve the mechanism of phoresis due to action of a non-contact force field rather than direct pushing or pulling. Phoresis draws energy from the environment through the gradient of interfacial non-contact body forces. Due to the difference of interfacial structure transmitting the interfacial body forces to drive phoresis, researchers have found various scaling laws with particle size, such as a^1 (Duhr and Braun 2006), a^0 (Braibanti, Vigolo et al. 2008), and even a^{-1} (Ebbens and Howse 2011). Recently, a special class of motors has been actively studied that can generate an asymmetrical local field

to move themselves with it, namely, autonomous Janus motors (Paxton, Sen et al. 2005; Wang, Duan et al. 2013). Since the field is generated locally, it exhibits unique characteristics. For example, the local concentration gradient can be much higher than conventionally achievable since the surface is in direct contact to the source or sink. With those various scaling laws in hand, phoresis can be a promising propulsion method at the micro/nanoscales. However, the underlying physics is largely elusive.

1.2 Phoresis: Definition, Historical Review, and Scientific Applications

Phoresis is a very common motion phenomenon of micro/nanoscale colloidal particles. It has been so far understood as a result of the particle surface interacting with surrounding fluid through an interfacial non-contact force field. Since the non-contact force field can be changed by many other bulk fields, a colloidal particle can move towards either higher or lower such field when it is uneven, due to the corresponding uneven force field. Depending on the driving field, phoresis can be sub-categorized into many "-phoresis", e.g., electrophoresis (Ünlü, Morgan et al. 1997; Boguth, Harder et al. 2000), thermophoresis (Goren 1977; Talbot, Cheng et al. 1980), or diffusiophoresis (Derjaguin 1987; Anderson and Prieve 1991), due to uneven electrical potential, temperature, and chemical concentration, respectively, as the source of loading. The phoretic motion is unique because the propulsion originates from a self-balanced interactive force field in a narrow interfacial layer between the particle and the fluid. If a control volume is defined around the particle with far enough a boundary, the net force within it is equal to zero. There are also other phenomena named after phoresis, for example, barophoresis, in which the driving gradient field is pressure. In such a case, the net force in the control volume is not necessarily zero. The present study is focused on those cases with self-balanced active forces confined in the thin interfacial layer of a solid particle and surrounding fluid. It might be worth noting that for the case of electrophoresis, the driving force field may be due to an external electric field.

However, since the net charge near the particle is balanced by counterions, the net force is still zero.

The motion phenomenon is always relative, as shown in Figures 1.2(a) and (b). Relative to a surrounding fluid, the particle motion driven by a field gradient is termed phoresis, as discussed above. On the other hand, the local flow field accompanying the particle motion, certainly, caused by the same field gradient, is termed osmosis. Many times, since the solid surface can be reasonably assumed stationary, only the osmosis is discussed. In the same way as how the phoresis is classified, there are electro-osmosis following electric field (Pretorius, Hopkins et al. 1974), thermo-osmosis following temperature field (Denbigh and Raumann 1952), and osmosis without any prefix or capillary-osmosis though conventionally referred to flow following active agent concentration (Derjaguin, Dukhin et al. 1972). Even though the present study is focused on the phoresis, the osmosis always accompanies, which is often said to be the driving force for the former.

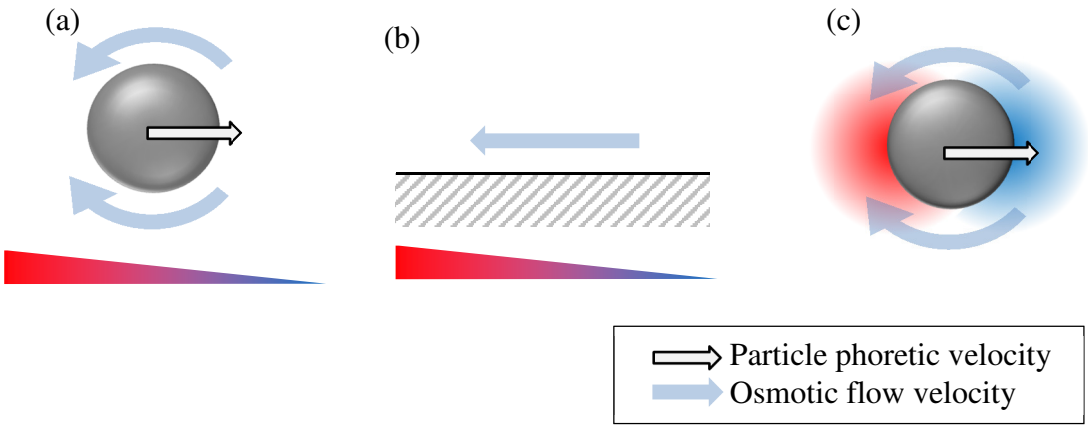

Figure 1-2 Illustration of different viewpoints of interfacial flow phenomenon: (a) assuming the far field fluid is stationary, particle motion is termed as phoresis; (b) assuming the solid surface is stationary, the near-surface flow is termed as osmosis; (c) a self-phoresis phenomenon of a particle driven by a self-generated local field.

Recently, there has been actively explored a special class of motors, called self-phoretic motor, that can generate an asymmetrical local field of chemical concentration, temperature and/or electrical field, and can move themselves with it. Its illustration is given in Figure 1-2c. Since the field is generated locally, it shows different characteristics from conventional phoretic phenomena on many different scales. For example, the local concentration gradient can be much higher than conventionally achievable when externally applied since the surface is in direct contact to the source or sink.

1.2.1 Electrophoresis

Electrophoresis is the motion of a charged colloid particle under the influence of a spatially uniform electric field. Because of the effect of the double layer (Helmholtz 1853), the entire ion-particle assembly can be considered hold zero net charge. Thus the force applied by the external electric field has no net force in this system. However, due to the forces are applied at different locations of the fluid system, it drives the surrounding fluid to flow in one direction and the particle to move in the opposite direction. The conceptual depiction can be found in Figure 1-3a. Electrophoresis has been observed as early as 1807 (Ferdinand Frederic Reuss). It has attracted major research attention since its capability of separating chemicals (Tiselius 1937) , especially in biochemical area, such as DNA sequencing.

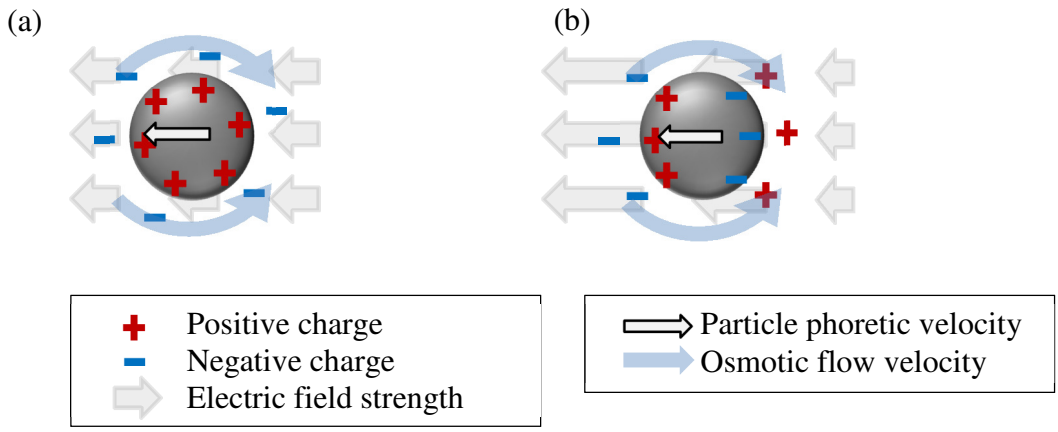

Figure 1-3 Schematic of (a) electrophoresis (b) dielectrophoresis

A sub-type of electrophoresis is called dieletrophoresis (Pohl and Pohl 1978) in which a dielectric particle moves along with the gradient of electric field, as shown in Figure 1-3b. Since dielectricphoresis does not require the particle to be charged on its surface, any particle can be consider moveable with dielectrophoresis. However, the dielectrophoretic speed is proportional to the dielectric constant of the particle, which can be very small for some material.

A more recent design of micro-/nano-motor is self-electrophoresis. It was designed to self-generate a local electric field to propel the device with electrophoresis (Jaffe, Robinson et al. 1974). The electric field can be generated by local catalytic reaction (Golestanian, Liverpool et al. 2007; Gibbs and Zhao 2009; Ibele, Mallouk et al. 2009; Baraban, Tasinkevych et al. 2011), absorbing electromagnetic wave (Sen, Ibele et al. 2009), or any other methods that can transform energy into an electric field.

1.2.2 Diffusiophoresis

Diffusiophoresis is defined as colloidal particle motion that move toward or against the concentration gradient of one or more specific solute. It also has been known as “cross diffusion” when considering a large quantity of colloids. The specific concentration that particle follows, so

called active agent, change the interfacial body forces, thus a concentration gradient of active agent will introduce an asymmetrical interfacial body force field around the particle. It cause the interfacial flow and as a result, diffusiophoresis. Diffusiophoresis was theoretically predicted and experimentally demostrated by Derjaguin and others in 1947.

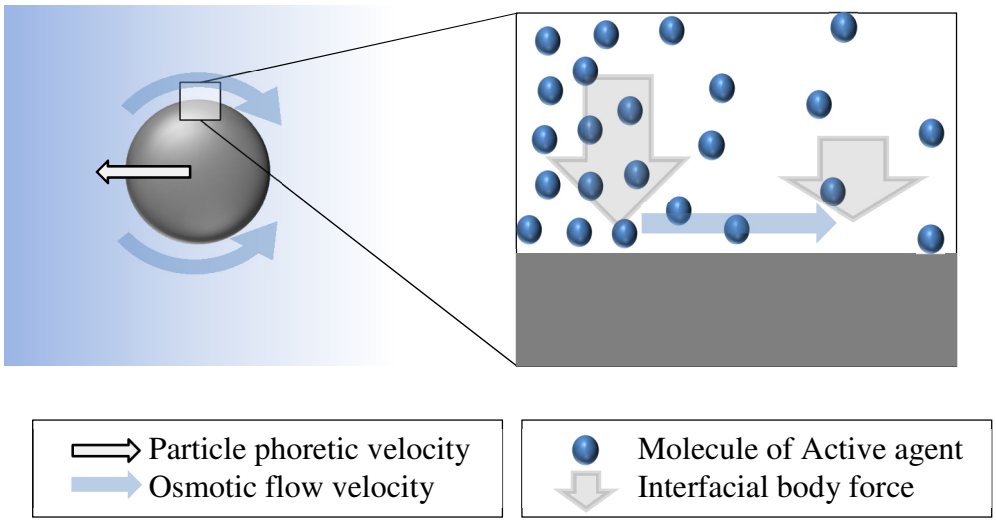

Figure 1-4 Schematic of diffusiophoresis

Researchers found diffusiophoresis can be important for living body systems, such as chemotaxis. Chemotexis is defined as the phenomenon that an organism move in respond to the surrounding concentration gradient of active agent, such as bacteria moves toward nutrition or sperm moves toward egg through tracking calcium concentration (Roegiers, McDougall et al. 1995). There also studies suggest that self-diffusiophoresis can be found in biological system, such as chromosome can depolarize its end node and releasing a local concentration gradient to propel its self with self-diffusiophoresis during bacterial mitosis (Banigan, Gelbart et al. 2011).

Diffusiophoresis is also used in artificial micro/nanoscale devices. Through the use of semipermeable membrane, one can control the active agent concentration dynamically by changing the fluid on the other side of the membrane, hence controlling the particle motion through diffusiophoresis. Diffusiophoresis also can be introduced by electric field induced electrolyte concentration gradient. The idea of self-diffusiophoresis is also been used with propelling artificial micro-/nano-motor. The motor is designed asymmetrically, i.e, a Janus particle, and induce an uneven concentration gradient of active agent, mostly using catalytic reaction.

1.2.3 Thermophoresis

Thermophoresis is defined as colloid particle motion under the effect of temperature gradient. Similar to diffusiophoresis, temperature difference will cause the density of the fluid change, which cause the interfacial body force also change, hence thermophoresis. The effect also called the Soret effect, however, the term Soret effect is mostly reserved for the combination result of diffusion and thermophoresis. An example that may be observed by the naked eye is when the hot surface of an electric heater is surrounded by tobacco smoke. The smoke stay away and leave an immediate vicinity of the hot surface. In this example, the equilibrium of local smoke particle concentration can be put as $D\nabla\chi = -D_T\chi\nabla T$, where D is the diffusivity of smoke particle, χ is the smoke particle concentration, and T is the temperature. The D_T is the thermophoretic mobility defined as $U = -D_T\nabla T$ where U is the phoretic speed. It is very clear that the equilibrium is built on the balance of diffusivity and thermophoresis. Thus the Soret coefficient is define as the quotient of diffusivity and thermophoretic mobility as $S_T = D_T/D$. Up to doday, most of the experiments that measuring thermophortic mobility of small particles, i.e., few tens nanometer size, are based on measuring the concentration of particles and find the thermophoretic mobility through Soret coefficient.

Just as self-electrophoresis and self-diffusiophoresis, self-thermophoresis is also been introduced. Researchers used gold or Silver as irradiant for ambient light and create local temperature gradient. Since many activities may involve releasing thermo energy, the self-thermophoresis should be considered in many cases, such as Janus catalytic particle.

1.3 Interfacial Structures that Impact Phoresis Mobility

Since the phoresis event is all about how to channeling the bulk energy difference into the fluid dynamic motion near the interface, the interfacial structure paly crucial role. While scientists keep digging down to small scale, the understanding of interfacial structure is much more improved than the time that phoresis equations has been put. Thus, one goal of this dissertation is to find out how those interfacial structures would impact the phoresis mobility and surface osmosis flow.

1.3.1 Electric Double Layer

Electric double layer is when an ionized or charged surface immersed in a fluid solution of ions, the ions in fluid will be adsorbed onto the surface and form a layer by layer structure. It has been proposed by Helmholtz (1853). Since then, many scientists improved the model to be more flexible to relate the observation of electrophoresis experiments (Chapman 1913). Usually, the first layer is assumed to be completely adsorbed that have no mobility. Starting from the next layer, ions aggregate and distribute following the Boltzmann distribution. However, in the general sense, highly aggregated ions should change the fluid nature, such as viscosity, density. In this point of view, the immobile layer can be considered a result of very high viscosity.

1.3.2 Hydrophilic and Hydrophobic Surfaces

Hydrophobicity is easy to observe and quantify by the experiment of contact angle; however, in the case of phoresis, we need more information than a simple contact angle. Till today, how the interfacial structure link to hydrophobicity is still under debate. While the

experiment of X-ray indicates the observation of the near surface depletion (Mezger, Reichert et al. 2006). If the depletion thickness is the main reason of hydrophobicity, it can be link to the length scale of the interfacial potential. For most cases, a hydrophobic surface is holding no charge and is not ionized, thus water molecules are more attracted by themselves, due to its highly polar molecule structure. In this assumption, hydrophobicity links to the attraction strength of the interfacial potential.

There is a class of surface that been categorized as super hydrophobic surface. It is usually built with micro-/nano-structure that can hold air or other gas in between water and the surface. In this case the water is basically detached to the surface.

1.3.3 Slip Boundary Condition

Boundary slippage is another important effect that should be considered. The very early model of boundary slip is proposed by Navier (1823). The definition of "slip legth", l_s, has been proposed. Slip length is defined as the thickness of a virtual layer that connect real fluid field and surface, which the thickness is specified to match no slip boundary condition with the same viscosity of the bulk fluid. Therefore, ls = 0 indicates the boundary is fully sticky, and $l_s = \infty$ means it is fully slippery. However, most of the experimental agreements with this approach are curve-fitting in nature without linking to the fundamental physics behind it. Also, the theory is yet a first-order approximation that may not work in every case. The slip length of water-solid interface could set between zero and a few tens nanometers for an atomically smooth surface, or hundreds to thousands nanometers for a micro-/nano-structured surface (Lauga, Brenner et al. 2007; Bocquet and Charlaix 2010). Researchers indicated many causes that could lead to a large slip length, e.g., in large Kudsen number fluid (Morris, Hannon et al. 1992), with water on highly hydrophobic surface (Tretheway and Meinhart 2002), with high-concentration dissolved gas in liquid, and with nano-bubbles attached to a surface (Lauga, Brenner et al. 2007). Researchers have analyzed the boundary slip effect on unconstrained bodies in fluid, which is the case of phoretic motor. The drag coefficient of a spherical particle floating in unconfined fluid

is analytically found by Basset (1888). More numerical calculations have been done for various situations, e.g., two spheres (Luo and Pozrikidis 2008), and a Janus particle with non-slip/slip coating (Swan and Khair 2008).

1.4 Summary and Objective

Phoresis including self-phoresis can be an effective way to propel micro-/nanometer scale motors in fluid. In order to gain in-depth understanding of the underlying mechanism and to realize the technological applications, a sophisticated theory taking into account important characteristic features is required. For various potential applications involving more complicated interfacial structures than the ideal gas law, the classical theory based on Boltzmann distribution and on no-slip boundary condition is no longer adequate. Therefore, in the present dissertation, we aim to reformulate the continuum theory of osmosis/phoresis by taking into account a general interfacial structure comprising viscosity variation and mass density variation as well as a non-contact body force field. Within the formulation, we examine intriguing interfacial phenomena due to Navier's boundary slip, to near-surface phase transition, and to an anisotropic interfacial pressure field (i.e., interfacial tension).

1.5 Organization of this Dissertation

In Chapter 2, we review three analytical approaches of phoresis. 1. The most classic theory of phoresis in an incompressible fluid and with no-slip boundary condition. 2. Maxwell-Navier's boundary condition that improved the first model with Navier's slip boundary condition. This model considered the near surface viscosity change with the shear stress provided by the bulk hydrodynamic drag. 3. The improved slip boundary condition that considered the shear stress from interfacial force. This model improved Maxwell-Navier's slip boundary condition with the consideration of interfacial force can highly change the slip velocity since it is the driving force of the phoresis.

In Chapter 3, we present a general formulation of phoretic mobility in real fluids by taking into account near-surface viscosity variation, mass density variation and noncontact forces. The problem is solved analytically by applying the reciprocal theorem. We also present the solution to the special case of a spherical particle with uniform slip length where the auxiliary solution is available. Further, the solution is expanded in multipole series.

In Chapter 4, we present the solution with active agent (with which the particle surface interact to generate the noncontact body force) following the Boltzmann distribution. The cases of both diffusiophoresis and thermophoresis are discussed. We also investigate how the solution reacts to a Lenard Jones style, 3-9, surface potential.

In Chapter 5, we employed a real equation of state of water to study how phase transition would impact phoresis. We solved the interfacial structure and found the temperature dependency of the adsorbed water film thickness. With the analytical solution given in Chapter 3, we analyzed how phase transition would impact the magnitude and size dependency of phoresis.

In Chapter 6, a molecule dynamics simulation is used to find the interfacial structure. By the stress result of simulation and analytical solution form Chapter 3, we found the phoretic speed that from both interfacial body forces and the pre-accumulated stress from the interfacial structure.

Chapter 2

Phoretic Mobility Approaches Used in Past Studies

In this Chapter, we summarize existing theoretical approaches for phoresis that were used in past studies. It will be the starting point of our new approach. All the theories listed below start with a near-surface body force field. The source of the body force is not specified to generalize the description for all different kinds of phoresis. With different interfacial structure assumptions, researchers found different solutions for the body force-induced flow field, which is known as osmotic flow. By balancing that momentum change, the particle motion in the opposite direction can be solved.

To start with, the strictest assumption is a feature-less interfacial structure with uniform viscosity and uniform mass density fields where the near surface flow follows the Stokes flow equations with a simple no-slip boundary condition. The result is a velocity discontinuity across the interface, given by (Derjaguin 1987). $\boldsymbol{u}|_{r=a} - \boldsymbol{U} = \boldsymbol{u}'^{b.f.}$, where $\boldsymbol{u}$ is fluid velocity, $\boldsymbol{U}$ is the solid surface velocity, and $\boldsymbol{u}'^{\boldsymbol{b.f.}}$ is the lumped velocity discontinuity from the layer containing the body forces. In most cases, $\boldsymbol{u}'^{b.f.}$ is assumed to be proportional to the gradient of a field that carries the body forces, such as temperature gradient and concentration gradient. The phoretic velocity can be found by the area average velocity discontinuity as (Anderson and Prieve 1991) $\boldsymbol{U} = -\langle \boldsymbol{u}^{b.f.} \rangle$, where the arrow bracket is the operator of area average. A relaxed assumption is that there is an interfacial structure with varying viscosity. When the varying viscosity effect is also lumped, it results in a summation of classical Navier's slip boundary condition (Navier 1823) $\boldsymbol{u}'^{Nv}$, and the velocity discontinuity form body force $\boldsymbol{u}'^{b.f.}$ as the Maxwell-Navier boundary condition of (Maxwell 191X): $\boldsymbol{u}|_{r=a} - \boldsymbol{U} = \boldsymbol{u}'^{Nv} + \boldsymbol{u}'^{b.f.} = \frac{ls}{\eta}[(\boldsymbol{I} - \boldsymbol{nn}) \cdot (\boldsymbol{n} \cdot \boldsymbol{\sigma})] + \boldsymbol{u}'^{b.f.}$, where ls is the slip length, and η is the (bulk) viscosity. It implies that the shear stress, $(\boldsymbol{I} - \boldsymbol{nn}) \cdot (\boldsymbol{n} \cdot \boldsymbol{\sigma})$, is assumed to be invariant across the interfacial zone of varying viscosity. In most studies, the shear stress is taken to be the asymptotic value from the bulk fluid (Talbot, Cheng et al. 1980).

In some recent studies, Ajdari and Bocquet (2006) and Morthomas and Würger (2009) combined it with the effect of the interfacial body force field – the same force field facilitating the driving force for phoresis. By realizing that ls can be huge in many systems, Ajdari and Bocquet termed the resulting phoresis "*giant*" by assuming the contribution from remote shear stress is trivial. However, the assumption of invariant shear stress across the interfacial zone of varying viscosity is generally invalid. In the following, we summarize these existing models. They represent the state-of-the-art status of this area of research in phoresis, and they provide the starting point for the present dissertational work.

2.1 Model with No-slip Boundary Condition

The fluid environment is assumed to be incompressible and at very low Reynolds number. The Reynolds number is defiend by $Re = \rho U a/\eta$, where ρ is the mass density, and a is the particle radius. In a typical case of our interest, a particle of radius a = 1 μm would move at speed U = 1 μm/s in water of viscosity η = 10^{-3} Pa s. The corresponding Reynolds number is ~ 10^{-6}, which is much smaller than one unit. Thus, the flow would follow the equation set of Stokes creeping flow theory as

$$\boldsymbol{\sigma} = -p\boldsymbol{I} + \eta(\nabla\boldsymbol{u} + (\nabla\boldsymbol{u})^T) \tag{2.1}$$

$$\nabla \cdot \boldsymbol{\sigma} = -\boldsymbol{b} \quad , \tag{2.2}$$

$$\nabla \cdot \boldsymbol{u} = 0 \tag{2.3}$$

where $\boldsymbol{\sigma}$ is the stress tensor, $\boldsymbol{b}$ is the body force density, $\boldsymbol{I}$ is identity tensor, and p is the pressure. The interfacial model is built under a local near-surface coordinate system as shown in Figure 2-1. Substituting Eq. (2.1) in Eq. (2.2), one obtains, in the local reference frame,

$$\sigma_{ZX,X} + \sigma_{ZZ,Z} = -p_{,Z} + \eta\left(u_{Z,XX} + u_{Z,ZZ} + u_{X,ZX} + u_{Z,ZZ}\right) = -b_Z, \tag{2.4}$$

$$\sigma_{XX,X} + \sigma_{XZ,Z} = -p_{,X} + \eta\left(u_{X,XX} + u_{X,ZZ} + u_{X,XX} + u_{Z,XZ}\right) = 0 \tag{2.5}$$

where the subscript index indicates the component in that direction, and the subscript comma indicates the partial differentiation with respect to the indices that follow. By assuming the local

velocity has value only along tangential direction X and its partial differentiation only has value toward normal direction Z. Thus, Eq. (2.4) and Eq. (2.5) can be reduced to

$$p_{,Z} = b_Z, \tag{2.6}$$

$$p_{,X} = \eta u_{X,ZZ} \tag{2.7}$$

By integrating Eq. (2.6), the local pressure can be found as

$$p(Z) = p^{\infty} - \int_Z^{\infty} b_Z dZ. \tag{2.8}$$

Also, integrating Eq. (2.7) would yield the osmotic flow rate as (Derjaguin, Dukhin et al. 1972)

$$u'^{b.f.} = u_X^{\infty} - u_X^0 = \frac{1}{\eta}\int_0^{\infty} Z \frac{\partial p}{\partial X} dZ$$

$$= -\frac{1}{\eta}\int_0^{\infty} Z \int_Z^{\infty} \frac{\partial b_Z}{\partial X} dZ\, dZ.$$

$$= -\frac{1}{2\eta}\int_0^{\infty} Z^2 \frac{\partial b_Z}{\partial X} dZ \tag{2.9}$$

where $u^{b.f.}$ is the velocity discontinuity between the solid surface and the bulk fluid. Since the interfacial layer is small compared to any dimension of the bulk fluid, the upper limit in both integrals of Eqs. (2.8) and (2.9) is taken to be the infinity. The superscripted b.f. indicates it is induced by the body forces.

By assuming that the interfacial velocity discontinuity is a material property, independent of remote loading condition, it allows for a solution to the phoretic speed as (Anderson and Prieve 1991)

$$\boldsymbol{U} = -\langle \boldsymbol{u}'^{b.f.} \rangle, \tag{2.10}$$

where the arrowed bracket denotes an area average. For a spherical particle, we have $\frac{\partial b_Z}{\partial X} = \frac{\partial b_r}{a\partial\theta} = \sin(\theta)\frac{\partial b_r}{\partial z}$, in the coordinate systems as defined in Figure 2-2. Thus, Eq. (2.10) can be rewritten into

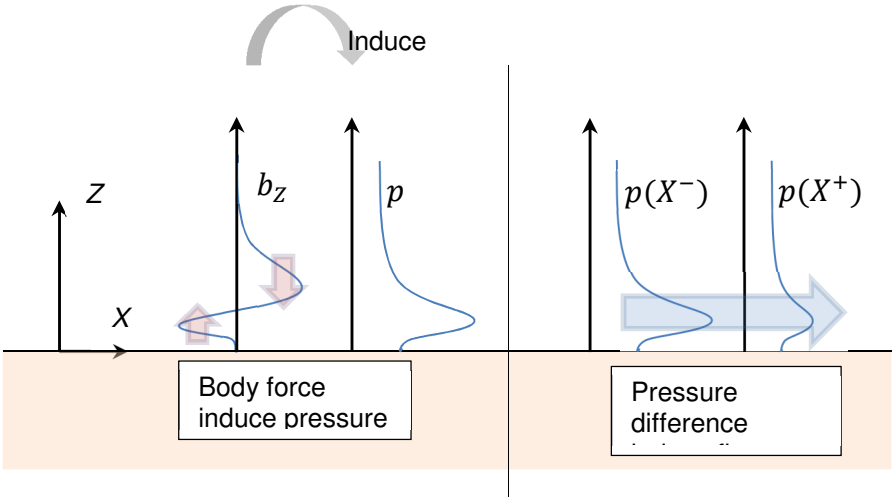

Figure 2-1 Schematic showing how body forces induce near-surface flow

$$U = \frac{1}{4\eta}\int_0^{\pi} \sin^3(\theta) \int_0^{\infty} Z^2 \frac{\partial b_r}{\partial z} dZ d\theta. \tag{2.11}$$

Assuming that $\frac{\partial b_r}{\partial z}$ is uniform over the particle surface, Eq. (2.11) can be further reduced to

$$U = \frac{1}{3\eta}\int_0^{\infty} Z^2 \frac{\partial b_r}{\partial z} dr. \tag{2.12}$$

It represents the solution of the phoretic speed of a spherical solid particle by the velocity discontinuity model. It can be seen that this solution involves no size effect of phoretic mobility. However, strong size effect of phoretic mobility has been experimentally observed in various systems (Würger 2013).

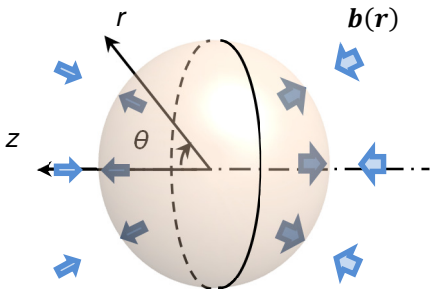

Figure 2-2 Coordinate systems of a spherical particle subjected to an interfacial force field

2.1.1 Active Agent of Boltzmann Distribution

Anderson developed the model of Eqs. (2.10) and (2.12) for diffusiophoresis. He assumed that the body force is introduced by the interaction of active agent with a surface and that the active agent follows the Boltzmann distribution as $c = C^{\infty}e^{-\frac{\Phi}{k_BT}}$. In the expression, Φ is the mean-force potential of active agent, and C^{∞} is defined as the concentration of active agent far enough away from the surface and not affected by the surface interaction. Typically, the surface potential can extend its effect up to tens of nanometers. Assuming that Φ is only a function of radial distance *r*, the force induced by this potential can expressed as $\boldsymbol{b} = -C\nabla\Phi = -\hat{\boldsymbol{r}}C\frac{d\Phi}{dr}$. By assuming that only the radial component is nontrivial, it can be further expanded as

$$b_r = -C^{\infty}e^{-\frac{\Phi}{k_BT}}\frac{d\Phi}{dr}. \tag{2.13}$$

By substituting Eq. (2.13) into Eq. (2.12), the phoretic velocity can be derived as

$$U = \frac{1}{3\eta}\frac{\partial}{\partial z}\left(C^{\infty}\int_0^{\infty}Z^2e^{-\frac{\Phi}{k_BT}}\frac{d\Phi}{dr}dZ\right),$$

$$= \frac{2}{3\eta}k_BT\frac{\partial}{\partial z}(C^{\infty}\bar{M}_2),$$

$$\text{with } \bar{M}_2 = \int_0^{\infty}\left(e^{-\frac{\Phi}{k_BT}} - 1\right)ZdZ \tag{2.14}$$

where $\bar{M}_2$ is the normalized second force moment.

For most cases of diffusiophoresis, the potential should be considered as "mean-force" potential; it represent a sum all forces that from the surface to the fluid finite volume, instead of the active agent molecules only. The assumption implied here is that the summed force is proportional to the concentration of active agent. This assumption should be taken with cautious.

2.2 Model with the Maxwell-Navier Slip Boundary Condition

Back in late 1800s and early 1900s, researchers found that flow may exhibit velocity discontinuity at a solid surface and that the velocity discontinuity is responsive to the local shear stress. It was suggested to be due to the reduced viscosity near the surface. Integrating the viscosity variation effect results in Navier's boundary condition. With the assumption of that change range is small comparing with all the bulk length scale, the difference between real velocity and expected velocity as if the viscosity is uniform can be expessed as

$$\boldsymbol{u}'^{Nv} = \int_0^\infty \left(\frac{1}{\eta} - \frac{1}{\eta^\infty}\right) dZ \, (\boldsymbol{I} - \boldsymbol{nn}) \cdot (\boldsymbol{n} \cdot \boldsymbol{\sigma}) = \frac{l_s}{\eta^\infty} (\boldsymbol{I} - \boldsymbol{nn}) \cdot (\boldsymbol{n} \cdot \boldsymbol{\sigma}). \tag{2.15}$$

where $ls \left(\equiv \int_0^\infty \left(\frac{\eta^\infty}{\eta} - 1\right) dZ\right)$ is the slip length, $(\boldsymbol{I} - \boldsymbol{nn}) \cdot (\boldsymbol{n} \cdot \boldsymbol{\sigma})$ is the shear stress assumed to be constant across the space of viscosity variation, and superscript "Nv" indicates that the velocity discontinuity is caused by Navier's slip. This is only a first order approximation to the nonlinear near-surface behavior. Researchers found it is applicable in many situations (Lauga, Brenner et al. 2007). In gas, the slip length is mostly corresponding to the mean free path. In liquid, the slip length can hold a value from zero to few tens of nanometer if the solid surface is smooth. It can even go up to several tens of micrometers if the surface is designed with super-hydrophobic nano-structures.

Combing the velocity discontinuities in Eq. (2.9) and Eq. (2.15), the total velocity discontinuity can be written as

$$\boldsymbol{u}|_{r=a} - \boldsymbol{U} = \boldsymbol{u}'^{Nv} + \boldsymbol{u}'^{b.f.}. \tag{2.16}$$

The above equation is called the Maxwell-Navier slip boundary condition (Maxwell 1879). It reflects the interfacial structure of body forces and viscosity variation, as shown in Figure 2-3. It is assumed that the body force dose not contribute any shear stress to the slip boundary condition. The only shear stress acting on the slip boundary condition is the hydrodynamic drag from the bulk fluid.

If the slip length is uniform over the particle surface, the particle phoretic speed can be derived as (Talbot, Cheng et al. 1980)

$$\boldsymbol{U} = \frac{-1}{(1+2\frac{l_s}{a})}\langle \boldsymbol{u}'^{b.f.} \rangle \quad . \tag{2.17}$$

The model was originally developed for thermophoresis and took into account some other parameters such as the thermal conductivity. However, Eq. (2.17) was its main merit.

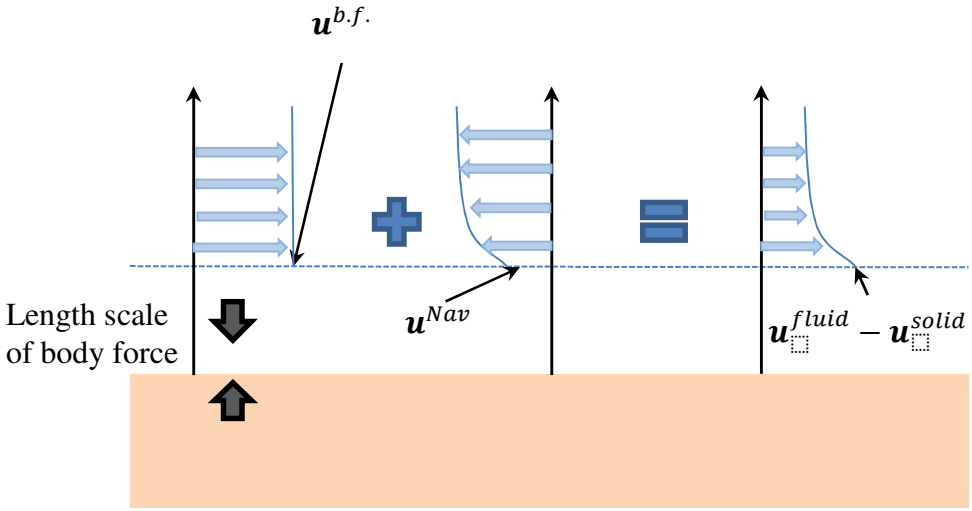

Figure 2-3 Schematic showing the interfacial structure implied in Eq. (2.16).

By comparing Eq. (2.17) with Eq. (2.10), it is easy to see that with increasing ratio of slip length to particle radius, l_s/a, the phoretic speed would decrease/diminsh in this model, if the slip length is positive. This model introduced the size effect into the phoretic speed, and

indicated that the smaller the particle, the slower the speed, which is not always true in experiments.

2.3 Model with Navier's Slip Boundary Condition and Body-force induced Interfacial Stress

In the classical Maxwell-Navier slip boundary condition, the shear stress is taken to be the asymptote from the bulk fluid, and is assumed to be constant across the interfacial layer of viscosity variation. This assumption may not be always correct, since the shear stress does change due to the interfacial body forces that generate the osmotic flow. Ajdari and Bocquet (2006) pointed out the possible enhancement of phoresis due to the interfacial slip with molecule dynamics simulation. They proclaimed that the osmotic flow and phoretic speed can be significantly enhanced. Assuming that the local viscosity η is only different from its bulk value in a small range from the surface and holds a much smaller value than the bulk value, the inverse of local viscosity η can be approximated as a Dirac delta function that at the location that $Z = 0$, which will take all the shear stress change, $\Delta\tau$, that provided by the interfacial body force. Since the interfacial slip adds a term $l_s\Delta\tau/\eta^{\infty}$, proportional to the slip length, to the velocity discontinuity, and since l_s can be large in many micro- and nano-systems. Following them, researchers (Morthomas and Würger 2009) derived analytical solution of phoretic speed based on modified Maxwell-Navier's boundary condition. It can be written as

$$\boldsymbol{U} = \frac{-1}{(1+2\frac{l_s}{a})}\langle \boldsymbol{u}'^{b.f.} + \frac{l_s\Delta\tau}{\eta^{\infty}}\rangle. \quad . \tag{2.18}$$

One can see that when the slip length approach infinity, the particle speed no longer dimishes as in Eq. (17). Instead, it approaches to an asymptotic value of $a\Delta\tau/6\eta$.

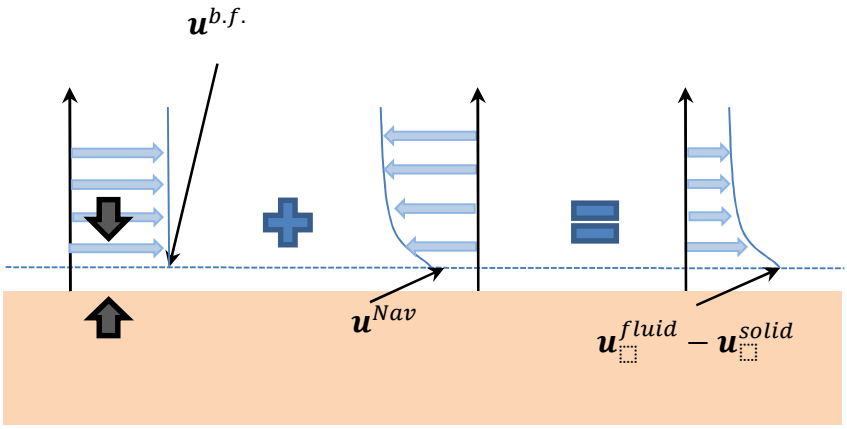

Figure 2-4 Illustration the interfacial structure implied in Eq. (2.18) that the slip boundary condition considered the effect of body force

Chapter 3

Continuum Mechanics Formulation of Phoresis

We consider the problem of a (spherical) solid particle in fluid, as shown in Figure 3-1. At the nanometer scale, the solid surface may exert long-range, noncontact forces on the fluid molecules, leading to a nonlocal body force field acting in the fluid near the interface. The sum of forces, including all forces acting on the solid and the fluid, is equal to zero. However, due to the force nonlocality and to the nature of the fluid, interfacial osmotic flow may be induced, if the force field is nonuniform around the particle surface. By the law of momentum conservation, the particle would move too, which is termed "phoresis". The nonuniform interfacial force field may be due to a nonuniform temperature field if the forces are a function of temperature or due to a nonuniform solute concentration field if the forces are responsive to the solute. As shown in Figure 3-1, the most general case of a continuum description of the surrounding fluid would include varying mass density $\rho(\boldsymbol{r})$ and varying viscosity $\eta(\boldsymbol{r})$. The asymptotic bulk values are indicated by ρ^{∞} and η^{∞}. Both of the viscosity variation and density variation, as well as the interfacial force field, can affect the phoretic mobility, as shown next. In Section 3.1, the problem is formulated. In Section 3.2, the general analytical solution is found for a particle with generally varying mass density, viscosity and body force fields by applying the reciprocal theorem. In Section 3.3, the special case with uniform Navier's hydrodynamic slip is considered. The multipole approach is also introduced.

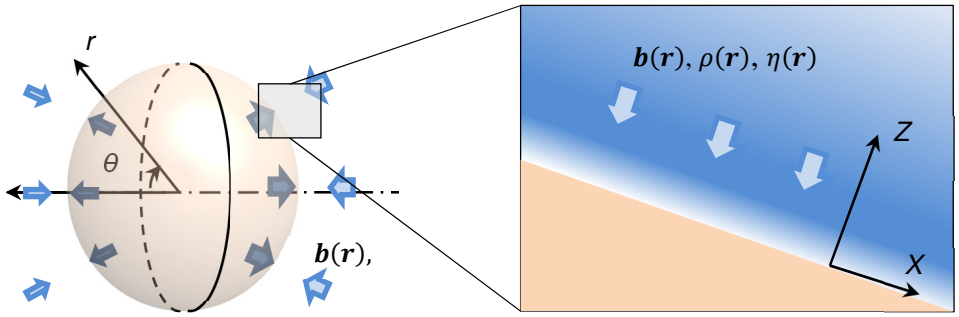

Figure 3-1 Schematic showing a general interfacial structure with a body force field and varying mass density and viscosity.

3.1 Problem Statement

Due to the small size and the relatively slow motion of a particle under consideration, the Stokes creeping flow theory neglecting the inertia effect is employed to describe the flow around the particle. The equilibrium condition requires

$$\nabla \cdot \boldsymbol{\sigma} + \boldsymbol{b} = 0, \tag{3.1}$$

where $\boldsymbol{\sigma}$ is the stress tensor, $\boldsymbol{b}$ is the body force density, ∇ is the del operator, and the dot denotes the dot product. $\nabla \cdot \boldsymbol{\sigma}$ means the divergence of stress. The fluid is assumed to be Newtonian and isotropic, satisfying the constitutive law:

$$\boldsymbol{\sigma} = -p\boldsymbol{I} + \eta(\nabla \boldsymbol{u} + (\nabla \boldsymbol{u})^T) + \boldsymbol{\sigma}^0, \tag{3.2}$$

where $\boldsymbol{u}$ is the velocity, p is the hydrostatic pressure, η is the viscosity, $\boldsymbol{I}$ is the identity tensor, the superscript T denotes the matrix transpose, and $\boldsymbol{\sigma}^0$ is the pre-stress. $\boldsymbol{\sigma}^0$ may be present prior to the viscous flow. The flow, represented in the second term on the right-hand side of Eq.

(3.2), may occur to relax $\boldsymbol{\sigma}^0$ and other loads. The last governing equation is the mass conservation law, which is given by

$$\frac{\partial \rho}{\partial t} = -\nabla \cdot (\rho \boldsymbol{u}), \tag{3.3}$$

where ρ is the mass density, and t is the time.

At the fluid-solid interface, Navier's slip condition is imposed:

$$\boldsymbol{u}|_{r=a} - \boldsymbol{U} = \boldsymbol{\beta} \cdot (\boldsymbol{n} \cdot \boldsymbol{\sigma}) \tag{3.4}$$

where $\boldsymbol{\beta}$ is the tensorial frictional coefficient, $\boldsymbol{u}$ is the flow velocity on the fluid side, and $\boldsymbol{U}$ is the particle velocity. At the interface, the traction is assumed to be continuous.

It should be remarked that in a typical Stokes flow formulation, as used in Chapter 2, the mass density ρ is assumed to be constant, both spatially and in time. It leads to the incompressibility condition, $\nabla \cdot \boldsymbol{u} = 0$. It is taken to replace the mass conservation law, Eq. (3.3) to complete the formulation. Furthermore, uniform viscosity is often assumed, leading to the commonly adopted governing equation, $-\nabla p + \eta \nabla^2 \boldsymbol{u} + \boldsymbol{b} = 0$. In the present study, both of the mass density and the viscosity can vary significantly near the fluid-solid interface. Meanwhile, those aforementioned assumptions can still be made over the bulk fluid. The following investigation is tasked to derive efficient solutions of particle speed by accounting for these properties.

3.2 Reciprocal Theorem

The reciprocal theorem can be a powerful tool to solve certain linear or weakly nonlinear problems as long as the corresponding auxiliary solution is available. This is applicable to our case of a spherical particle propelled by a confined force field near the particle surface. The auxiliary solution of a spherical particle subjected to a concentrated force in Stokes flow is available. The alternations to material properties, which are the viscosity and the mass density in the present case, are also confined in a thin interfacial layer.

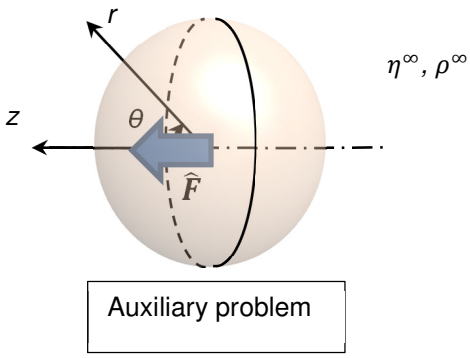

Figure 3-2 Schematic showing the auxiliary problem used in the reciprocal theorem

In the auxiliary problem, the fluid around a spherical particle is assumed to be uniform. It satisfies the following equilibrium equation, the constitutive law of Newtonian flow, and the incompressibility condition:

$$\nabla \cdot \hat{\boldsymbol{\sigma}} = 0, \tag{3.5}$$

$$\hat{\boldsymbol{\sigma}} = -\hat{p}\boldsymbol{I} + \eta^\infty(\nabla\hat{\boldsymbol{u}} + (\nabla\hat{\boldsymbol{u}})^T), \tag{3.6}$$

$$\nabla \cdot \hat{\boldsymbol{u}} = 0, \tag{3.7}$$

where the over-cap indicates the association of a quantity to the auxiliary problem, and η^∞ is the uniform viscosity. The same Navier slip condition at the fluid-solid interface as in the target problem is applied, which is written as

$$\hat{\boldsymbol{u}}|_{r=a} - \hat{\boldsymbol{U}} = \boldsymbol{\beta} \cdot (\boldsymbol{n} \cdot \hat{\boldsymbol{\sigma}}) \tag{3.8}$$

Also, the traction is assumed to be continuous across the interface.

Applying double dot product of $\eta^\infty(\nabla\hat{\boldsymbol{u}} + (\nabla\hat{\boldsymbol{u}})^T)$ to both sides of Eq. (3.2), applying double dot product of $\eta(\nabla\boldsymbol{u} + (\nabla\boldsymbol{u})^T)$ to both sides of Eq. (3.6), and realizing $(\nabla\hat{\boldsymbol{u}} + (\nabla\hat{\boldsymbol{u}})^T) : (\nabla\boldsymbol{u} + (\nabla\boldsymbol{u})^T) = (\nabla\boldsymbol{u} + (\nabla\boldsymbol{u})^T) : (\nabla\hat{\boldsymbol{u}} + (\nabla\hat{\boldsymbol{u}})^T)$, one may obtain

$$\begin{aligned}\hat{\boldsymbol{\sigma}} &: \eta(\nabla\boldsymbol{u} + (\nabla\boldsymbol{u})^T) + \hat{p}\boldsymbol{I} : \eta(\nabla\boldsymbol{u} + (\nabla\boldsymbol{u})^T) \\ &= (\boldsymbol{\sigma} - \boldsymbol{\sigma}^0) : \eta^\infty(\nabla\hat{\boldsymbol{u}} + (\nabla\hat{\boldsymbol{u}})^T) + p\boldsymbol{I} : \eta^\infty(\nabla\hat{\boldsymbol{u}} + (\nabla\hat{\boldsymbol{u}})^T).\end{aligned} \tag{3.9}$$

Due to the property of the identity matrix **I**, the following equations hold:

$$\boldsymbol{I} : (\nabla \boldsymbol{u} + (\nabla \boldsymbol{u})^T) = 2\nabla \cdot \boldsymbol{u}$$

$$\boldsymbol{I} : (\nabla \hat{\boldsymbol{u}} + (\nabla \hat{\boldsymbol{u}})^T) = 2\nabla \cdot \hat{\boldsymbol{u}} \tag{3.10}$$

Effecting these identities and the symmetry condition of stress, and applying Eq. (3.7), one may reduce Eq. (3.9) to:

$$\hat{\boldsymbol{\sigma}} : \nabla \boldsymbol{u} + \hat{p}\nabla \cdot \boldsymbol{u} = \frac{\eta^{\infty}}{\eta}(\boldsymbol{\sigma} - \boldsymbol{\sigma}^0) : \nabla \hat{\boldsymbol{u}}. \tag{3.11}$$

Splitting the right-hand-side term yields

$$\hat{\boldsymbol{\sigma}} : \nabla \boldsymbol{u} + \hat{p}\boldsymbol{I} : \nabla \boldsymbol{u} = \boldsymbol{\sigma} : \nabla \hat{\boldsymbol{u}} - \boldsymbol{\sigma}^0 : \nabla \hat{\boldsymbol{u}} + \frac{\eta^{\infty} - \eta}{\eta}(\boldsymbol{\sigma} - \boldsymbol{\sigma}^0) : \nabla \hat{\boldsymbol{u}}. \tag{3.12}$$

Applying the chain rule, Eq. (3.1), and Eq. (3.5), one may recast Eq. (3.12) as

$$\nabla \cdot (\hat{\boldsymbol{\sigma}} \cdot \boldsymbol{u}) + \hat{p}\nabla \cdot \boldsymbol{u} = \nabla \cdot (\boldsymbol{\sigma} \cdot \hat{\boldsymbol{u}}) + \boldsymbol{b} \cdot \hat{\boldsymbol{u}} - \boldsymbol{\sigma}^0 : \nabla \hat{\boldsymbol{u}} + \frac{\eta^{\infty} - \eta}{\eta}(\boldsymbol{\sigma} - \boldsymbol{\sigma}^0) : \nabla \hat{\boldsymbol{u}}. \tag{3.13}$$

Applying volume integral over the fluid domain on both sides of Eq. (3.13), and applying the divergence theorem, one may obtain

$$\begin{aligned} &\iint_S \boldsymbol{n} \cdot \hat{\boldsymbol{\sigma}} \cdot \boldsymbol{u} dS + \iiint_V \hat{p}\nabla \cdot \boldsymbol{u} dV \\ &= \iint_S \boldsymbol{n} \cdot \boldsymbol{\sigma} \cdot \hat{\boldsymbol{u}} dS + \iiint_V \boldsymbol{b} \cdot \hat{\boldsymbol{u}} dV - \iiint_V \boldsymbol{\sigma}^0 : \nabla \hat{\boldsymbol{u}} dV + \iiint_V \frac{\eta^{\infty} - \eta}{\eta}(\boldsymbol{\sigma} - \boldsymbol{\sigma}^0) : \nabla \hat{\boldsymbol{u}}\, dV. \end{aligned} \tag{3.14}$$

Applying the interfacial traction continuity condition and velocity discontinuity condition in Eqs. (3.4) and (3.8), one may further derive

$$\begin{aligned} &\iint_S \boldsymbol{n} \cdot \hat{\boldsymbol{\sigma}} \cdot \boldsymbol{u} dS = \boldsymbol{U} \cdot \iint_S \boldsymbol{n} \cdot \hat{\boldsymbol{\sigma}} dS + \iint_S \boldsymbol{n} \cdot \hat{\boldsymbol{\sigma}} \cdot (\boldsymbol{\beta} \cdot (\boldsymbol{n} \cdot \boldsymbol{\sigma})) dS, \\ &\iint_S \boldsymbol{n} \cdot \boldsymbol{\sigma} \cdot \hat{\boldsymbol{u}} dS = \hat{\boldsymbol{U}} \cdot \iint_S \boldsymbol{n} \cdot \boldsymbol{\sigma} \cdot dS + \iint_S \boldsymbol{n} \cdot \boldsymbol{\sigma} \cdot (\boldsymbol{\beta} \cdot (\boldsymbol{n} \cdot \hat{\boldsymbol{\sigma}})) dS. \end{aligned} \tag{3.15}$$

Assuming that $\boldsymbol{\beta} = \boldsymbol{\beta}^{\boldsymbol{T}}$, and substituting $\iint_S \boldsymbol{n} \cdot \hat{\boldsymbol{\sigma}} dS = \hat{\boldsymbol{F}}$ and $\iint_S \boldsymbol{n} \cdot \boldsymbol{\sigma} \cdot dS = -\iiint_V \boldsymbol{b} dV$ (assuming that no force is applied at remote boundary), one may finally arrive at

$$\hat{\boldsymbol{F}} \cdot \boldsymbol{U} = \iiint_V \left(\hat{\boldsymbol{u}} - \hat{\boldsymbol{U}}\right) \cdot \boldsymbol{b} dV + \iiint_V \frac{\eta^{\infty} - \eta}{\eta}(\boldsymbol{\sigma} - \boldsymbol{\sigma}^0) : \nabla \hat{\boldsymbol{u}} dV - \iiint_V \boldsymbol{\sigma}^0 : \nabla \hat{\boldsymbol{u}} dV - \iiint_V \hat{p}\nabla \cdot \boldsymbol{u} dV. \tag{3.16}$$

On the right hand side, the first term represents the effect of the interfacial body force field. The second term represents the effect of varying viscosity. The third term represents the effect of preloaded stress field. The last term represents the effect of fluid "compressibility". These terms are all volumetric integrals. Fortunately, in the present case of phoresis, all of these forces and viscosity and mass density variations are confined within a thin layer at the interface. Also, note that in the second and the last terms, $\boldsymbol{\sigma}$ and $\boldsymbol{u}$ are both unknown. However, since these near-interface fields should be largely induced by the nearby body force $\boldsymbol{b}$, they can be approximated by the classical local solutions as outlined in Chapter 2. Given the auxiliary solution, Eq. (3.16) can be applied to derive the phoretic speed in various specific conditions within the continuum mechanics framework.

3.3 Multipole Approach in Special Case

Following Eq (3.16), which is the most general form of phoresis speed, here we present a special case of a spherical particle phoresis in the fluid that the density is assume to be uniform, and the variation of viscosity is lumped to surface as slip length, which are the similar assumptions that made in Eq. (2.18). The different between Eq. (2.18) and the solution we derived later is that the shear stress variation has been solved under the global coordinate. This allowed us not to make unnecessary assumptions about how to solve the shear stress locally. Furthermore, we derived the solution into multipole expansion by the Taylor series. The multipole solution show simple and clear of how the particle relied on the slip length, particle size, and the body force profile that represented by multipole

In the case of a spherical particle with uniform, scalar slip constant (i.e., uniform $\boldsymbol{\beta} = \beta\boldsymbol{I}$) over the interface, the auxiliary solution is available in an analytical form, which is presented below. With this auxiliary solution, the first term on the right-hand side of Eq. (3.16) can be ambiguously expanded in a multipole form to elucidate how the force field works, alongside the Navier slip condition, to propel the particle in a viscous fluid environment.

The auxiliary solutions are given by (Happel and Brenner 1983)

$$\hat{u}_r = \hat{U}\cos(\theta)\left(\frac{3}{2}\frac{2\frac{l_S}{a}+1}{3\frac{l_S}{a}+1}\frac{a}{r} - \frac{1}{2}\frac{1}{3\frac{l_S}{a}+1}\frac{a^3}{r^3}\right), \tag{3.17}$$

$$\hat{u}_\theta = -\hat{U}\sin(\theta)\left(\frac{3}{4}\frac{2\frac{l_S}{a}+1}{3\frac{l_S}{a}+1}\frac{a}{r} + \frac{1}{4}\frac{1}{3\frac{l_S}{a}+1}\frac{a^3}{r^3}\right), \tag{3.18}$$

$$\hat{F} = 6\pi\eta^\infty a\hat{U}\left(\frac{2\frac{l_S}{a}+1}{3\frac{l_S}{a}+1}\right), \tag{3.19}$$

$$\hat{p} - \hat{p}^\infty = \frac{3}{2}\frac{2\frac{l_S}{a}+1}{3\frac{l_S}{a}+1}\eta^\infty a\hat{U}\cos(\theta)\frac{1}{r^2}. \tag{3.20}$$

where slip length $l_s \equiv \beta/\eta^\infty$. In the auxiliary problem, the remote hydrostatic pressure $\hat{p}^\infty$ plays no role. It can also be found that the remote hydrostatic pressure can be removed from Eq. (3.16) if the surface does not have normal direction velocity discontinuity.

Assuming that both the viscosity and mass density are uniform and that there is no pre-stress field, Eq. (3.16) is reduced to

$$\boldsymbol{U}\cdot\hat{\boldsymbol{F}} = \iiint_V \boldsymbol{b}\cdot\left(\hat{\boldsymbol{u}} - \hat{\boldsymbol{U}}\right)dV. \tag{3.21}$$

By substituting the auxiliary solutions, Eqs. (3.17)-(3.19) into Eq. (3.21), the following expression of particle speed can be found

$$U = \frac{1}{6\pi\eta a}\iiint_V \left[\cos(\theta)\left(\frac{3}{2}\frac{a}{r} - \frac{1}{2}\frac{1}{2\frac{l_S}{a}+1}\frac{a^3}{r^3} - \frac{3\frac{l_S}{a}+1}{2\frac{l_S}{a}+1}\right)b_r - \sin(\theta)\left(\frac{3}{4}\frac{a}{r} + \frac{1}{4}\frac{1}{2\frac{l_S}{a}+1}\frac{a^3}{r^3} - \frac{3\frac{l_S}{a}+1}{2\frac{l_S}{a}+1}\right)b_\theta\right]dV \tag{3.22}$$

Given the body force $\boldsymbol{b}$, slip length l_s and particle size a, the above equation can be used to compute the particle phoretic speed. In most cases under consideration in the literature, there is only the radial component of body force, b_r.

Since all kinds of phoresis hold different profiles of a body force field, in this sub-section we discuss the special case that commonly holds by diffusiophoresis and thermophoresis, which is case that the body forces only act on radio direction. In this case, Eq. (3.30) can be reduced into

$$U = \frac{1}{6\pi\eta a}\iint_A \cos(\theta)\int_a^\infty \left(\frac{3}{2}\frac{a}{r} - \frac{1}{2}\frac{1}{2\frac{l_S}{a}+1}\frac{a^3}{r^3} - \frac{3\frac{l_S}{a}+1}{2\frac{l_S}{a}+1}\right)b_r\frac{r^2}{a^2}drdA. \tag{3.31}$$

The expression of Eq. (3.31) reduced the volumetric integral into a surface integral by sorting the outward direction integration as surface properties.

2.3.1 Muiti-pole Expansion of the Navier's Slip Model

To further analyze this, we followed its nature of phoresis that the body force in this analysis is only active within couple nanometers, thus we expand the integral that alone radius with Taylor expansion at the position of $r = a$. To be more concise, the local coordinate Z has been employed, which is related to local normal outward as Figure 3-3.

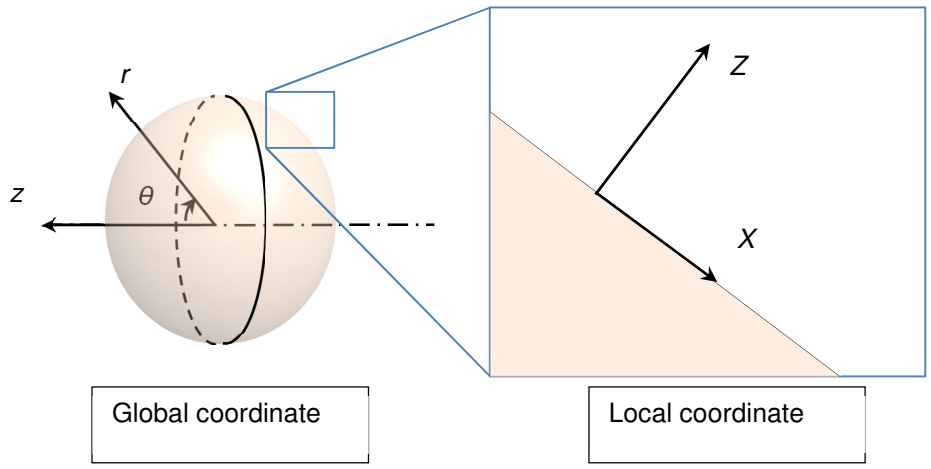

Figure 3-3 Illustration of the definition of global coordinate and local coordinate

Then, the integral term of radius direction can be defined as a function N and written as

$$\int_a^\infty \left(\frac{3}{2}\frac{a}{r} - \frac{1}{2}\frac{1}{2\frac{l_s}{a}+1}\frac{a^3}{r^3} - \frac{3\frac{l_s}{a}+1}{2\frac{l_s}{a}+1}\right) b_r \frac{r^2}{a^2} dr = \int_a^\infty N(r) b_r \, dr = \int_0^\infty N(Z) b_r(Z) \, dZ.$$

$$\text{where } N = \left(\frac{3}{2}\frac{r}{a} - \frac{1}{2}\frac{1}{2\frac{l_s}{a}+1}\frac{a}{r} - \frac{3\frac{l_s}{a}+1}{2\frac{l_s}{a}+1}\frac{r^2}{a^2}\right), \text{ and } Z = r - a \tag{3.32}$$

Taylor expansion of N at the position of $Z = 0$ can be written as

$$N = N(0) + N'(0)\frac{Z}{a} + \frac{1}{2}N"(0)\frac{Z^2}{a^2} + \cdots + O(\frac{Z^n}{a^n})$$

$$= -3\frac{\frac{l_S}{a}}{2\frac{l_S}{a}+1}\frac{Z}{a} - \frac{3}{2}\frac{Z^2}{a^2} + \sum_{n=3}^{\infty}(-1)^{n+1}\frac{1}{2}\frac{1}{2\frac{l_S}{a}+1}\frac{Z^n}{a^n}, \quad (3.33)$$

where $O(\frac{Z^n}{a^n})$ represent this expansion has an error that is on the scale of $\frac{Z^n}{a^n}$. Put this expansion into Eq (3.31), and we have

$$U = \frac{1}{12\pi\eta a}\iint_A \cos(\theta)\left[-6\frac{\frac{l_S}{a}}{2\frac{l_S}{a}+1}\frac{1}{a}M_1 - 3\frac{1}{a^2}M_2 + \sum_{n=3}^{\infty}(-1)^{n+1}\frac{1}{2\frac{l_S}{a}+1}\frac{1}{a^n}M_n\right]dA,$$

$$\text{where } M_n = \int_0^{\infty} Z^n b_r dZ \quad (3.34)$$

is the n-th normal force moment acted at the surface. Since the body force is only holding value near the range of $Z = d$, where d is the characteristic length of the body force, Eq. (2.34) can approach the real solution at the error of $O(\frac{d^n}{a^n})$ if the series have been cut at the (n-1) term.

In comparison to past study, we applied the assumption of a constant $\frac{\partial b_r}{\partial z}$ to the solution in Eq. (3.34), that made $b_r \cong {b_r}^o + a\cos(\theta)\frac{\partial b_r}{\partial z}$, where ${b_r}^o$ is the b_r function at $z = 0$, and $l_s = 0$ thus Eq. (3.34) can be rewrite as

$$U = \frac{1}{6\eta}\int_0^{\pi}\cos^2(\theta)\sin(\theta)\,d\theta\left[-3\frac{\partial M_2}{\partial z} + \sum_{n=3}^{\infty}(-1)^{n+1}\frac{1}{a^{n-2}}\frac{\partial M_n}{\partial z}\right]$$

$$= \frac{-1}{9\eta}\left[3\frac{\partial M_2}{\partial z} + \sum_{n=3}^{\infty}(-1)^n\frac{1}{a^{n-2}}\frac{\partial M_n}{\partial z}\right],$$

$$\text{where } \frac{\partial M_n}{\partial z} = \int_0^{\infty} Z^n\frac{\partial b_r}{\partial z}dZ. \quad \text{Eq. (3.35)}$$

The similarity of Eq (2.12) and Eq. (3.35) can be found at the non-size effective term, which is $\frac{\partial M_2}{\partial z}$ in Eq. (3.35). Equation (3.35) showed when $(\frac{d}{a})$ is small, the phoretic speed can less relate to particle size, which is similar with Eq. (2.12). Since the solution of Eq. (3.35) is rigorous, and all the expansions are orthogonal, this study recommend researchers use the first expansion of Eq. (3.35) to replace Eq. (2.12) for simple stokes flow phoresis in future study.

Chapter 4

Phoresis with Hydrodynamic Slip: An Analytical Solution

Since the time that phoresis has been observed, the near surface fluid flow of phoresis is always under debate. Due to the size and its moving nature, direct observation into the near surface region is not available. Thus even many researcher can find various intriguing behaviors of phoresis, such as phoresis with size dependency, temperature dependency, and surface dependency to greatly enhance or even change direction (Platten 2006). However, there is still missing a fundamental theory for predicting those behaviors with a thorough understanding of the near surface flow.

With the intensive study of micro-/nanometer fluid of the last decade, many new viewpoints have been made. Ajdari and Bocquet (2006) state there is a giant enhancement of apparent slip boundary condition to surface osmotic flow. Following them, Morthomas and Würger (2009) applied their theory on thermophoresis. However, the theory provide by Morthamos did not provide the link between body force and local shear stress, thus the solution has a remaining term of shear stress discontinuity. Also, since the solution is solved by local-global two step approach, there are assumptions that involved neglecting the stress translation across the surface. Finally, please note that the enhancement of the slip boundary required the mechanism that induced the slip to be shorter range to the surface than the body force field. The most possible interfacial structure that satisfies this assumption is the surface depletion layer as shown in Figure 4-1, which can be observed in many molecule level simulation (Sendner, Horinek et al. 2009). Some researchers relate the thickness of depletion with hydrophobicity and also the slip boundary condition (Poynor, Hong et al. 2006), but it is still under debate. Since there are many ways to induce the experimental slip condition (Lauga, Brenner et al. 2007) within finite thickness and there is no flow visualization technique that is able to ensure where the slip happened, the enhancement given by Ajdari and Bocquet has to be applied with caution.

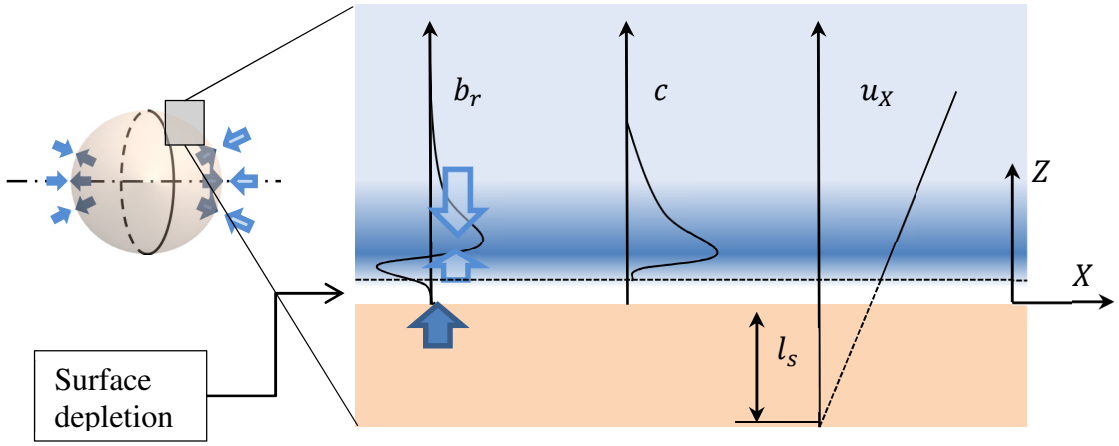

Figure 4-1 Near surface depletion induced slip boundary condition

In the case of the short range slip assumption is valid, there is still a missing piece before the theory can be applied to physical observation, which is how the nominal bulk properties, where the distance between the location from the particle surface is far enough that would not be affected by surface potential, affect the near surface structure and hydrodynamics. This link between bulk properties and local properties for the current state of art is not complete enough to explain the variety of abnormal behavior that we mentioned above. That is the reason we are here to solve the phoretic velocity by a complete analytical solution that solved in global coordinate, which avoid non-necessary assumptions that could potentially lead to misunderstanding of the nature of phoresis. In this chapter, two types of phoresis have been discussed. The two types of phoresis are thermophoresis and diffusiophoresis. The slip surface boundary condition will be considered. This chapter demonstrate how temperature, and slip boundary condition can affect the phoresis mobility.

4.1 Interfacial Structure of Boltzmann Distribution

Boltzmann distribution is an assumption taht molecules hold only repulsive interaction, which allows that all the molecules collision can be consider as elastic. With the Boltzmann Distribution assumption the local density can be written as

$$c = C^{\infty} e^{-\frac{\Phi}{k_B T}}. \tag{4.1}$$

Where c is the local concentration and C^{∞} is the concentration at where the potential Φ is defined as zero. For the case of surface, C^{∞} can be referred to the "bulk" concentration that far enough to not be affected by the surface potential. Typically, the surface potential shows no effect at few tens of nanometers. Also, k_B is Boltzmann constant and T is the local absolute temperature. Eq. (4.1) can be relate to ideal gas model easily by the link of body force, $b = -c\nabla\Phi$, and pressure, $\nabla p = b$.

The appropriate situation that can be assumed as Boltzmann distribution should be dilute enough for its thermodynamic condition to be far from phase change, which means low temperature or highly aggregated active agent will not be applicable, such as liquid phase fluid.

Before applying the Boltzmann distribution, here are some understandings that have to be clear. First, assuming there is no pressure gradient along any direction within the fluid, the changing of one concentration of the solution must affect others; for example, in ideal gas, the sum of the partial pressure is the total pressure, thus a gradient of one concentration must lead the partial pressure of the other mixed solute having a gradient toward the opposite direction. With this idea, it can be found that diffusiophoresis must be a phenomenon of everything within the fluid. However, usually researchers can find the effect of single active agent that dominates the event, which the effect of other solute is already integrated by to their concentration dependency. Another picture should be introduced before starting to solve this problem, which the concentration gradient indicates the existence of diffusion flux within the fluid. This means if the environment has a steady concentration gradient, there should be a source and sink somewhere to keep the concentration profile steady, thus the concentration profile can be

solved by the diffusion equations. For the simplest case that there is a bulk concentration gradient $\frac{\partial C^{\infty}}{\partial z}$ around the infinity outer boundary, the profile on a sphere particle has a profile of $\frac{1}{2}\frac{\partial C^{\infty}}{\partial z}$ on the particle surface. Since there is no flux across the surface, the concentration near the surface does not change much along the radio direction. Thus starting here, the term of "bulk concentration" refers to near surface concentration unless further noticed.

Assuming the particle has uniform surface material that makes the surface potential a function of distance between the active agent and surface only, which can be written as $\Phi(r)$, the force induced by this potential can expressed as $\boldsymbol{b} = -C\nabla\Phi = -\hat{\boldsymbol{r}}C\frac{d\Phi}{dr}$, which can be further expand with Eq. (4.1) as

$$b_r = -C^{\infty}e^{-\frac{\Phi}{k_BT}}\frac{d\Phi}{dr}. \tag{4.2}$$

For the case of most solutions, the potential should be changed into the "mean-force" potential; it is a sum of the two forces, the force from surface to the solute and the water void that had been occupied by the solute. And after the assumption that the solute is dilute enough that it is not able to change the water structure, and dilute enough that can be approached by the Boltzmann distribution, then we can use the same technique to estimate speed.

To further understand how the surface potential link to Eq. (4.1) and Eq. (4.2), we employed an artificial surface potential, 3-9 surface potential (Israelachvili 2011). The 3-9 surface potential is an integrated version of Lenard- Jones potential, which assumed all the material is distributed uniformly and continuously within the surface. A 3-9 surface potential can be written as $\Phi = \frac{\varepsilon}{2}\left[\left(\frac{\delta}{Z}\right)^9 - 3\left(\frac{\delta}{Z}\right)^3\right]$, where ϵ and δ are defined as the depth of the potential well and the location of the potential well, which represent the strength and the length scale of the 3-9 potential.

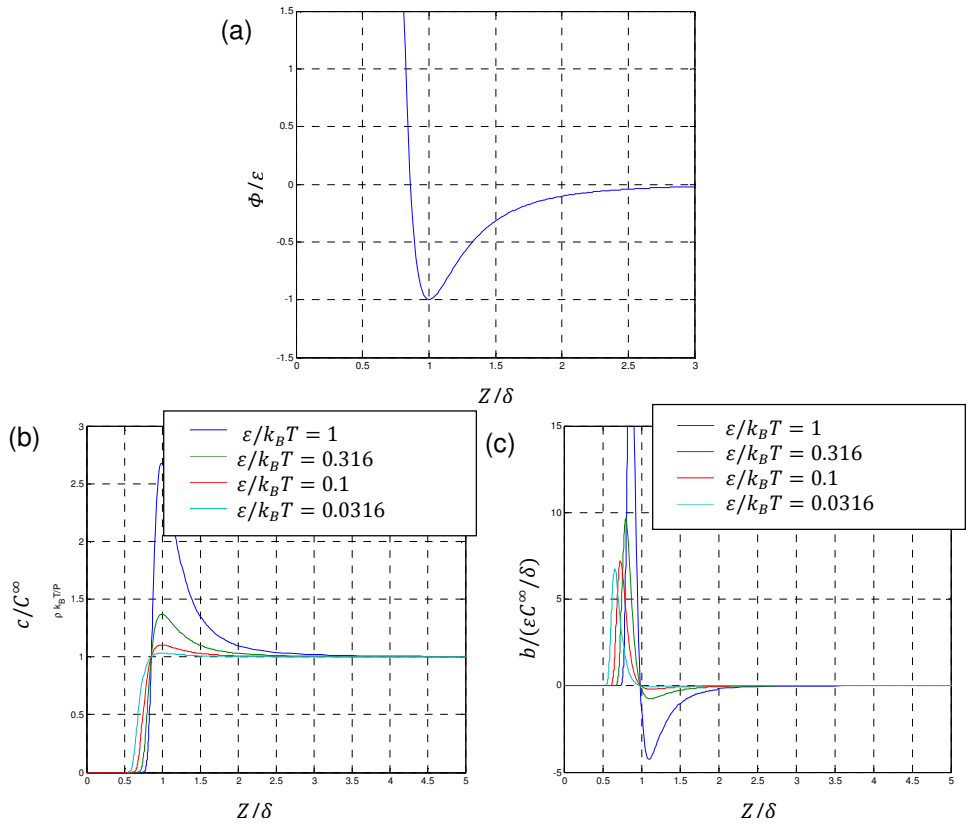

Figure 4-2 Near surface structure following Boltzmann distribution (a) 3-9 surface potential of $\Phi = \frac{\varepsilon}{2}\left[\left(\frac{\delta}{Z}\right)^9 - 3\left(\frac{\delta}{Z}\right)^3\right]$, (b) near surface concentration, and (c) near surface body force density

Some typical structure is shown in Fig 4.2. Solving the differential equation of Boltzmann distribution with bulk concentration as boundary condition will result that the bulk concentration is acting as supply and feed of the local potential until the diffusion flux is equilibrium with the flux provide by the surface potential. We used a numerical integral approach to illustrate the profile, which is backward difference in mesh size of 0.001 nm. As a result, in Figure 4-2(a), the potential profile of $\Phi = \frac{\varepsilon}{2}\left[\left(\frac{\delta}{Z}\right)^9 - 3\left(\frac{\delta}{Z}\right)^3\right]$ is shown, which represent the repelling-attracting nature of the surface potential. Since the surface potential is defined as

per molecule, which means a higher bulk concentration will result in the entire profile arising proportionally, Figure 4-2(b) is normalized by the bulk concentration. The body force density profile can be found in Figure 4-2(c) that showed the attractive nature at far surface and repelling nature at near surface.

4.2 Analytical Solution for Phoresis with Surface Structure of Boltzmann Distribution

In this section, the approaches followed the global hydrodynamic approach from Chapter 3. For convenient, here we rewrite the most generalized form Eq. (3.16) as

$$\widehat{\boldsymbol{F}} \cdot \boldsymbol{U} = \iiint_V \left(\widehat{\boldsymbol{u}} - \widehat{\boldsymbol{U}}\right) \cdot \boldsymbol{b} dV + \iiint_V \frac{\eta^{\infty} - \eta}{\eta} \nabla \widehat{\boldsymbol{u}} : \boldsymbol{\sigma} dV - \iiint_V \hat{p} \nabla \cdot \boldsymbol{u} dV. \tag{4.3}$$

After the assumption of uniform viscosity (all the viscosity changing has been lumped onto Navier's slip boundary condition) and uniform density (again, all the density change assumed only happen at the surface depletion and being neglected), one can reduce Eq. (4.3) into

$$\widehat{\boldsymbol{F}} \cdot \boldsymbol{U} = \iiint_V \left(\widehat{\boldsymbol{u}} - \widehat{\boldsymbol{U}}\right) \cdot \boldsymbol{b} dV. \tag{4.3}$$

Please notice that even there is no slip boundary condition terms in Eq. (4.3), the equation already include the slip boundary effect. To apply different slip boundary condition, one need to use different auxiliary solution, which can be provided by

$$\hat{u}_r = \widehat{U} \cos(\theta) \left(\frac{3}{2} \frac{2\frac{l_S}{a}+1}{3\frac{l_S}{a}+1} \frac{a}{r} - \frac{1}{2} \frac{1}{3\frac{l_S}{a}+1} \frac{a^3}{r^3} \right), \tag{4.4}$$

$$\hat{u}_\theta = -\widehat{U} \sin(\theta) \left(\frac{3}{4} \frac{2\frac{l_S}{a}+1}{3\frac{l_S}{a}+1} \frac{a}{r} + \frac{1}{4} \frac{1}{3\frac{l_S}{a}+1} \frac{a^3}{r^3} \right), \tag{4.5}$$

$$\hat{F} = 6\pi\eta^{\infty} a \widehat{U} \left(\frac{2\frac{l_S}{a}+1}{3\frac{l_S}{a}+1} \right), \tag{4.6}$$

By putting Eq. (4.4), (4.5), and (4.6) into Eq. (4.3), also, with the Boltzmann distribution in Eq. (4.1) and (4.2), Eq. (4.3) can be rewrite as

$$U = \frac{1}{12\pi\eta a} \int \cos(\theta) \left[-6 \frac{\frac{l_S}{a}}{2\frac{l_S}{a}+1} \frac{1}{a} M_1 - 3 \frac{1}{a^2} M_2 + \sum_{m=3}^{\infty} (-1)^{m+1} \frac{1}{2\frac{l_S}{a}+1} \frac{1}{a^n} M_m \right] dA, \tag{4.7}$$

$$M_m = -\int_0^\infty Z^m C^\infty e^{-\frac{\Phi}{k_B T}} \frac{d\Phi}{dr} dZ$$

$$= k_B T C^\infty \int_{Z=0}^\infty Z^m d\left(e^{-\frac{\Phi}{k_B T}} - 1\right)$$

$$= k_B T C^\infty \left[Z^{m+1}\left(e^{-\frac{\Phi}{k_B T}} - 1\right)\Big|_{Z=0}^\infty - m\int_0^\infty \left(e^{-\frac{\Phi}{k_B T}} - 1\right) Z^{n-1} dZ \right]$$

$$= -m k_B T C^\infty \int_0^\infty \left(e^{-\frac{\Phi}{k_B T}} - 1\right) Z^{m-1} dZ \qquad \text{if } \Phi|_{Z=\infty} = 0. \tag{4.8}$$

For the detail of deduction of Eq. (4.7), please check Chapter 3. Here, a normalized force moment can be defined

$$\bar{M}_m = \int_{Z=0}^\infty Z^{m-1}(e^{\frac{-\Phi}{kT}} - 1) dZ. \tag{4.9}$$

By observing the Eq. (3.9), one can find that the normalized force moment $\bar{M}_m$ have unit of length unit to the m-th power, and it has the magnitude of the potential length scale, such as $O(d^m)$. With Eq. (4.9), Eq. (4.7) can be re write as

$$U = \frac{1}{12\pi\eta a}\int \cos(\theta)\, k_B T C^\infty \left[6\frac{\frac{l_S}{a}}{2\frac{l_S}{a}+1}\frac{1}{a}\bar{M}_1 + 6\frac{1}{a^2}\bar{M}_2 + \sum_{m=3}^\infty (-1)^m m \frac{1}{2\frac{l_S}{a}+1}\frac{1}{a^n}\bar{M}_m \right] dA. \tag{4.10}$$

where slip length ls is defined as $\boldsymbol{u}|_{r=a} = \boldsymbol{U} + \frac{ls}{\eta}[(\boldsymbol{I} - \boldsymbol{nn}) \cdot (\boldsymbol{n} \cdot \boldsymbol{\sigma})]$.

4.2.1 Analytical Solution for Diffusiophoresis with Active Agent of Boltzmann Distribution

Assume the near surface far field concentration is have a uniform gradient ∇C^∞; Eq (3.10) can be surface integrated by putting $C^\infty = a\cos\theta\, \nabla C$, and have

$$\boldsymbol{U} = \frac{2k_B T a^2}{3\eta}\left(\frac{\frac{l_S}{a}}{2\frac{l_S}{a}+1}\frac{1}{a}\bar{M}_1 + \frac{1}{a^2}\bar{M}_2 + \frac{1}{6}\sum_{m=3}^\infty (-1)^m m \frac{1}{2\frac{l_S}{a}+1}\frac{1}{a^n}\bar{M}_m \right)\nabla C. \tag{4.11}$$

By observing Eq. (4.11), the terms starting from $\bar{M}_3$ can be neglect since under the assumption of $0 \le l_s < \infty$, there is no way that the $\bar{M}_3$ term can overcome the ration between $\bar{M}_2$, which is d/a. However, the first two term can be comparable if there is the slip length is around the scale of the potential length scale, such as $l_s \sim d$, which means for a larger or smaller scale of slip length, the first two term can larger or smaller to each other, thus making both term should be take into account . After neglect the terms after $\bar{M}_3$, the following can be find

$$\boldsymbol{U} = \frac{2k_BTa^2}{3\eta}\left(\frac{\frac{l_s}{a}}{2\frac{l_s}{a}+1}\frac{1}{a}\bar{M}_1 + \frac{1}{a^2}\bar{M}_2\right)\nabla C. \tag{4.12}$$

And the Figure 4-2 is a demonstration of when $\bar{M}_1$ or $\bar{M}_2$ will dominate the equation. The upper left half of Figure 3-2 represent the part that this equation will reduce to classical approach where there is nearly no slip on the surface, and the lower right half is represent the slippage term dominate the equation. However, in most physical system of phoresis, $\left|\frac{\bar{M}_2}{a\bar{M}_1}\right|$ is around the scale of d/a, which is can be around ten to the minus three or smaller. Thus in most cases, we recommend that the classical approach is at least missing one term.

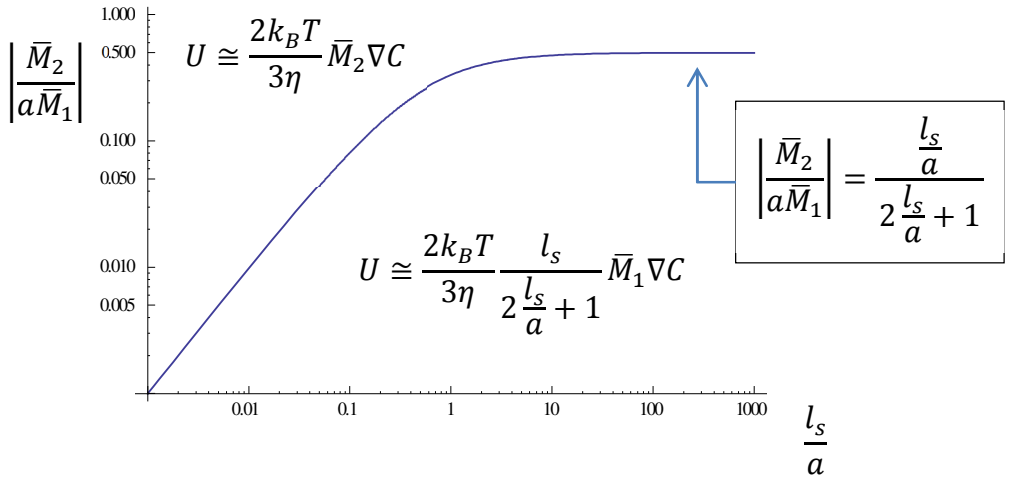

Figure 4-3 Asymptotic value of diffusiophoetic mobility as a function of first or second force moment in Eq. (4.12).

4.2.2 Analytical Solution for Thermophoresis of Active Agent of Boltzmann Distribution

Similar to Eq. (4.11), Eq. (4.10) can be surface integrated for thermophoresis by assume the temperature dependence $\left(\frac{\frac{l_s}{a}}{2\frac{l_s}{a}+1}\frac{1}{a}\bar{M}_1 + \frac{1}{a^2}\bar{M}_2\right)$ can be approached by linear as

$\left(\frac{\frac{l_S}{a}}{2\frac{l_S}{a}+1}\frac{1}{a}\bar{M}_1+\frac{1}{a^2}\bar{M}_2\right)=a\cos\theta\frac{\partial}{\partial T}\left(\frac{\frac{l_S}{a}}{2\frac{l_S}{a}+1}\frac{1}{a}\bar{M}_1+\frac{1}{a^2}\bar{M}_2\right)\nabla T$ around the particle surface. Eq. (4.10) can be rewrite as

$$\boldsymbol{U}=\frac{2a^2}{3\eta}p^{\infty}\frac{\partial}{\partial T}\left(\frac{\frac{l_S}{a}}{2\frac{l_S}{a}+1}\frac{1}{a}\bar{M}_1+\frac{1}{a^2}\bar{M}_2\right)\nabla T=\frac{2a^2}{3\eta}p^{\infty}\left(\frac{\frac{l_S}{a}}{2\frac{l_S}{a}+1}\frac{1}{a}\bar{M}_{1,T}+\frac{1}{a^2}\bar{M}_{2,T}\right)\nabla T. \tag{4.13}$$

Eq. (4.13) also neglect all the higher order term from $\bar{M}_{3,T}$ as the same reason in Section 4.2.1. Similar to Figure 4-3, Figure 4-4 shown the region map for where the normalized first force moment term, $\bar{M}_{1,T}$, or the normalized second force moment term, $\bar{M}_{2,T}$, will dominate Eq. (4.13) for thermophoresis.

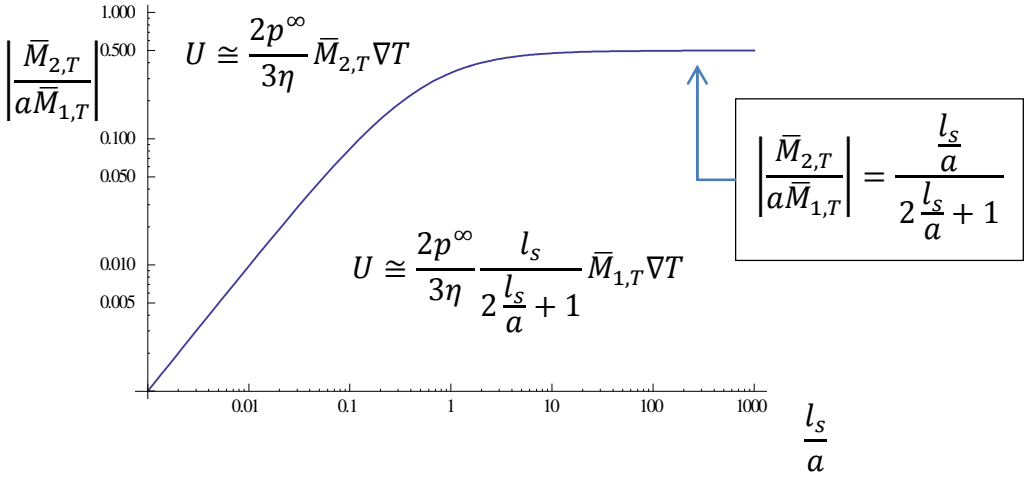

Figure 4-4 Asymptotic value of thermophoretic mobility as a function of first or second force moment in Eq. (4.13).

4.3 Analytical Solution for Phoresis of Solid Particle in Active Agent of Boltzmann Distribution: 3-9 Surface Potential

4.3.1: Non-Dimensional Muiltipole

By putting 3-9 potential, $\Phi = \frac{\varepsilon}{2}\left[\left(\frac{\delta}{Z}\right)^9 - 3\left(\frac{\delta}{Z}\right)^3\right]$, into $\bar{M}_1$ and $\bar{M}_2$, the length scale can be extract from it as

$$\frac{\bar{M}_1}{\delta} = \int_{Z=0}^{\infty}(e^{-\bar{\Phi}} - 1)dZ,$$

$$\frac{\bar{M}_2}{\delta^2} = \int_{Z=0}^{\infty} Z(e^{-\bar{\Phi}} - 1)dZ, \tag{4.14}$$

Therefore, the force moment now can present as non-dimensional parameter $\bar{M}_1/\delta$ and $\bar{M}_2/\delta^2$. In Figure 3-5, the profile of those non dimensional force moment $\bar{M}_1/\delta$ and $\bar{M}_2/\delta^2$ as function of normalized surface potential strength ε/k_BT. The profile is illustrated by numerical integral with built-in function in Matlab (Ref. XXXX). Please note that the force moment can range from positive to negative, and it does not required both to be on the same sign, which means, at the surface potential that hold different sign of first and second moment, there is a possibility that those modification in front of the first and second force moment can altering the solid particle to go to the opposite direction. In Eq. (4.12), those parameters that may hold the power to change particle moving direction are particle size and slip length.

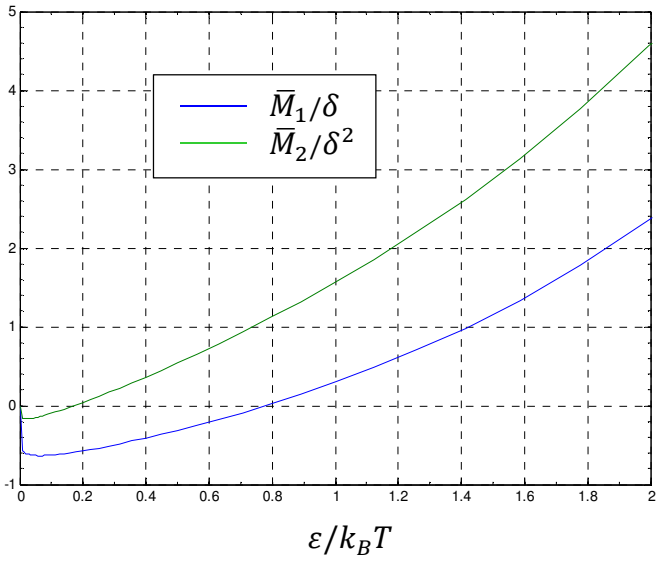

Figure 4-5 Profile of Non-dimensional force moment $\bar{M}_1/\delta$ and $\bar{M}_2/\delta^2$ as a function of normalized surface potential strength ε/k_BT

Similar non-dimensionalzation can be done to $\bar{M}_{1,T}$ and $\bar{M}_{2,T}$, and the result can be find in Figure 4-6. Since thermophoresis is relied on temperature change, Figure 4-6 use k_BT/ε instead of ε/k_BT as axis to insure better understanding.

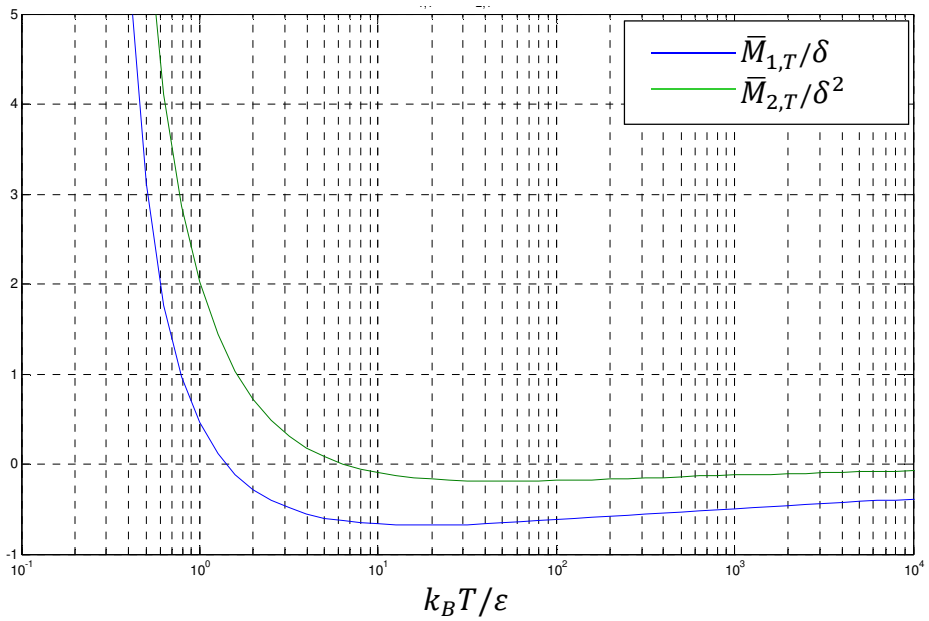

Figure 4-6 Profile of partial differentiation of the non-dimensional first and second force moment to temperature

4.3.2: Diffusiophoretic mobility

To exclude the effect of viscosity to the diffusiophoretic mobility, we here defined a poretic constant K from Eq. (4.12)

$$\boldsymbol{U} = \frac{-k_B T \delta^2}{3\eta} K \nabla C$$

$$K = K_1 + K_2 = -2\frac{\frac{l_S a}{\delta\delta}}{2\frac{l_S}{\delta}+\frac{a}{\delta}}\frac{\bar{M}_1}{\delta} - 2\frac{\bar{M}_2}{\delta^2}. \tag{4.15}$$

Now, the phoretic constant K is only function of three non-dimensional parameter, ε/k_BT, l_s/δ, and a/δ. By observing Eq (4.15), the concept of diffusiophoresis can be found that diffusiophoresis respond to the environment thermodynamic properties by the gradient of the osmotic pressure of the active agent, $k_BT\nabla C$, which can be consider as its driving source, but it

still have to multiply by the mechanism kernel $\delta^2 K/3\eta$, which include the material properties, hydrodynamic drag, and the size effect.

All the following result is computed by the body force given in Figure 4-5. Figure 4-7 illustrated how the phoretic constant K change with various range of l_s/δ. It is very clear that slip length impact the magnitude of the phoretic constant directly. The bundle indicate various particle size $a/\delta = 10^2 \sim 10^4$, it shows less impact comparing to slip length of the potential strength in this figure, however, please note that the size effect ramp up when the slip length is up. Due to the presentation reason that we want to keep the no-slip curve visible, Figure 4-7 only show l_s/δ up to 10.

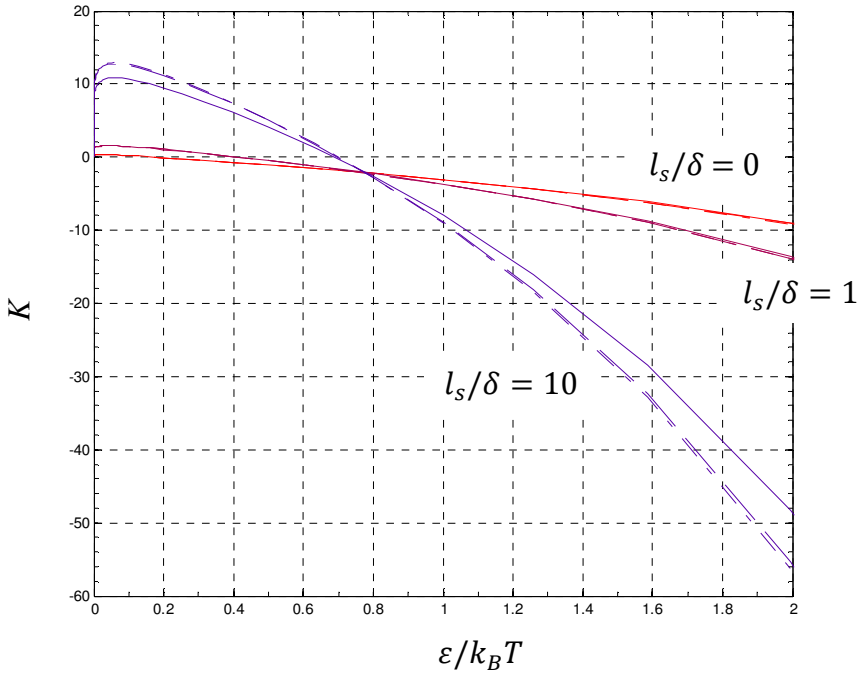

Figure 4-7 Phoretic constant K changing with various range of l_s/δ, the bundle represent different a/δ, which solid lines are for $a/\delta = 10^2$, longer dash lines are for $a/\delta = 10^3$, and shorter dash lines are for $a/\delta = 10^4$.

Figure 4-8 showed how the phoretic constant vary with the slip length. For all the surface potential strength, the size effect is clearer when slip length is larger according to the increases of the bundle width. The enlarged figure on the left of Figure 4-8 showed there is nearly no size effect when the slip length is low. It also show some special case that the phoretic constant is near zero by the balance of the slip and non-slip portion of it.

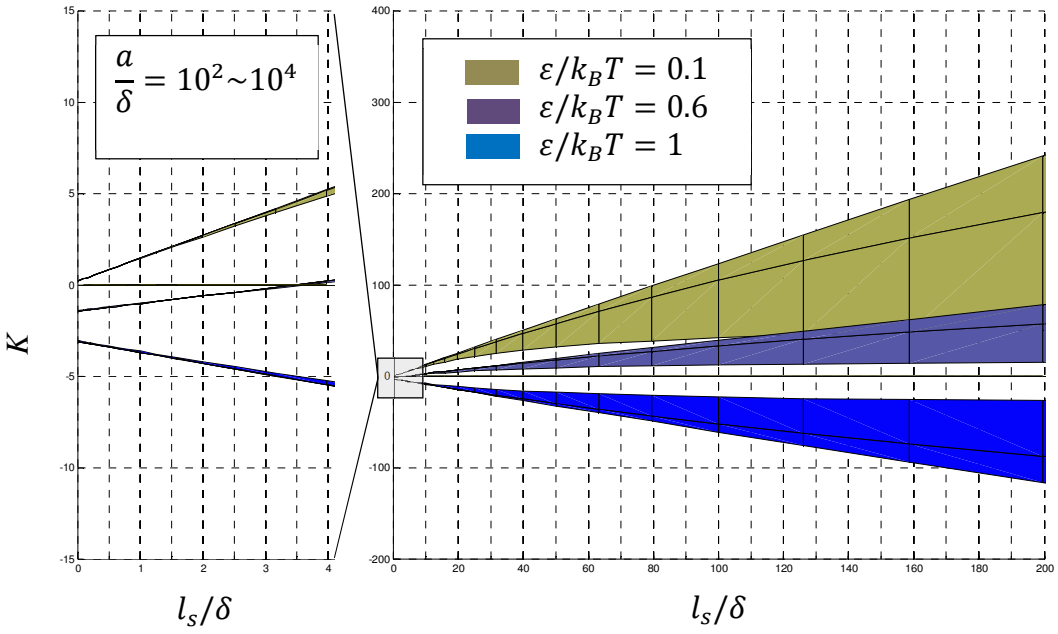

Figure 4-8 Phoretic constant with varying slip length and surface potential strength. The colored bundle show how it varied with difference size ratio of $\frac{a}{\delta} = 10^2 \sim 10^4$

.

Figure 4-9 is a closer look of how the phoretic constant K_1 and K_2 compare or balance with each other at the very special region of ε/k_BT~0.7. At that region, since $\bar{M}_1$ go crossed zero, the magnitude of K_1 is brought down, thus the profile is highly depend or altered by K_2.

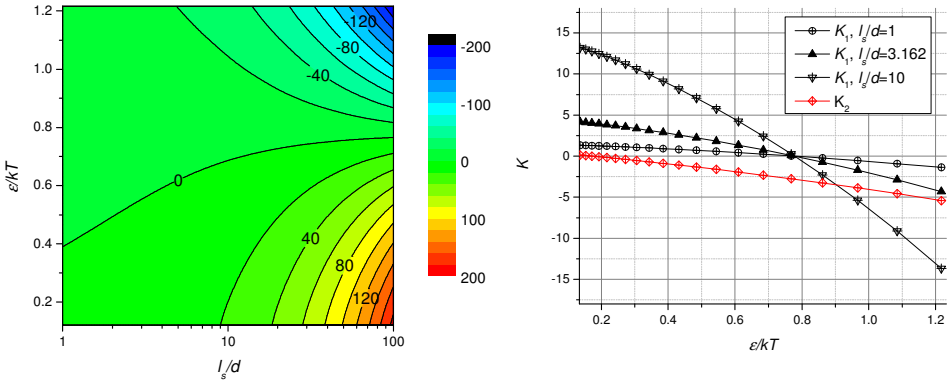

Figure 4-9 Phoretic constant at $a/\delta = 10^3$, with varying l_s/δ and ε/k_BT

4.3.2: Thermophoretic mobility

Similar to diffusiophoresis, thermophoresis under 3-9 surface potential can be estimate by putting Eq. (4.14) into Eq. (4.13), Eq. (4.13) can also be rewrite phoretic constant K as define in the previous section, but required slightly altered as

$$\boldsymbol{U} = \frac{-p^{\infty}\delta^2}{3\eta} K_{,T} \nabla T, \tag{4.16}$$

One can find the information of $K_{,T}$ in Figure 4-7, 4.8, and 4.9 from the partial differerntiation of temperature.

4.4 An Review of Modern Experiment of Thermophoresis with the Perspective of Master Curve

There is some understanding that has been made in the previous sections, which the phoretic velocity or direction rely on one or both of first and second force moment. Thus if we hold this idea and look back to Eq. (2.35), where the generalized thermophoresis with slip boundary condition (without the assumption of Boltzmann distribution and the surface potential can be arbitrary) can be expressed as

$$\boldsymbol{U} = -D_T \nabla T = \frac{1}{3\eta}\left(\frac{2l_s a}{2l_s+a} M_{1,T} + 2M_{2,T}\right)\nabla T, \tag{4.17}$$

where D_T is the thermophoretic mobility and $M_{1,T}$ and $M_{2,T}$ are presenting the contribution of first and second force moment. Another expression of measuring thermophoresis is by Soret coefficient, which described the overall distribution if there are a large number of colloid particle that thermo effect is pushing the particles back to diffusion equilibrium. By the definition Soret coefficient, $S_T \equiv D_T/D$, with diffusion constant $D = k_B T/\beta$, which is Einstein (1905) relation between drag coefficient and diffusion constant where β is drag coefficient of $\beta = 6\pi\eta a \frac{2l_s+a}{3l_s+a}$. Thus the Soret coefficient can be written as

$$S_T = \frac{D_T}{D} = \frac{4\pi a}{3k_B T}\left(\frac{3l_s a}{3l_s+a} M_{1,T} + \frac{6l_s+3a}{6l_s+2a} M_{2,T}\right), \tag{4.18}$$

With Eq. (3.17), Eq. (3.18), and the understanding above in hand, a new perspective to the experiments result of thermophoresis can be reached.

As the starting of this chapter stated, a great deal of work has been devoted to examining the dependence of D_T on various parameters such as temperature, particle size, particle surface property and solute composition. Some issues remain under active debate. For instance, some studies concluded that D_T is independent of particle size (Braibanti, Vigolo et al. 2008), whilst others reported clear size dependence (Duhr and Braun 2006). Various theoretical works were developed to interpret and support each of those controversial observations. While most studies showed that particles approach to the cold side (i.e., with a positive value of D_T), a few others indicated that they can also move towards the hot side (i.e., with a negative value of

D_T) at lower temperature. This thermophoretic directional reversal has also been observed when varying particle size (Braibanti, Vigolo et al. 2008). For the temperature dependency, Würger (2007) attributed the anomaly of water thermal expansion to this phenomenon, but there has been no theoretical explanation for the size-mediated directional switch.

Table 4-1 Published experiments of thermophresis in different surface conditions with fitted slip length and fitted force moments by Eq. (4.17)

Author	Duhr and Braun (2006)	Braibanti, Vigolo et al. (2008)		Eslahian and Maskos (2012)	Vigolo, Brambilla et al. (2007)
Particle material	polystyrene /w carboxyl coating	polystyrene /w carboxyl coating	polystyrene /w Triton	Polystyrene	Water /w Aerosol OT
Surrounding fluid	water	water	water	CsCl/ NaCl water solution	isooctane
Hydrophobic Surface	o	o	x	o	x
Fitted slip length	~500nm	~1nm	~0	0.5~1nm	~0
$2l_sM_{1,T}+M_{2,T}$	56.5fN/K	Figure 3-9	Figure 3-9	Figure 3-11	10.5fN/K
$M_{2,T}$	-1.16fN/K	Figure 3-9	Figure 3-9	Figure 3-11	-
note			Triton as surfactant		

As discussed above, for a typical colloidal particle, the first two terms in the series solution, the first and second force moment, would be sufficient to accurately represent the physical process. In the following, we use these two terms to fit some experimental data of Soret coefficient as a function of particle size *a* available from the literature. The curve fitting would result in estimates of slip length, l_s, and temperature derivatives of moments, $M_{1,T}$ and $M_{2,T}$. In order to conclude all those works at the same time, we define a dimensionless master curve as $\left(3\eta D_T - M_{2,T}\right)/2l_sM_{1,T}$. In Figure 3-10, that the nonlinear size effect from Duhr and Braun, Braibanti et al., and Eslahian and Maskos are fitted well to the master curve. Data from Duhr and Braun, aligned with the part of master curve that representing $l_s>>d$, thus leading the thermophoretic mobility almost proportional to the size. The experiment sets from Braibanti et al. has fitted the part of master curve that representing $l_s\geq d$;And as the theory predicted, after the

surfactant is into play, the particle will lose size dependency and go to the most right asymptotic since the slip length has been destroyed. Data from Eslahian and Maskos have only three data for each scenario of same surface condition, it can only fit a smaller portion on the master curve, however the trend is clear. Other researches that found no size dependence, including data from Vigolo et al and Braibanti et al. (with surfactant), are showed in the most right hand side asymptotic. Both of them are involving surfactant to strengthen the surface bounding, thus can be considered as no slip surface. Finally there are two set of data that involved size effect, data from Jiang et al. and data from Putnam et al., that we are not able to fit to the master curve. For the data from Jiang et al, there are only four data point and size dependency is not clear. For the work from Putnam et al., surface charge is a size dependent factor and will change the surface condition, thus not able to fit the master curve.

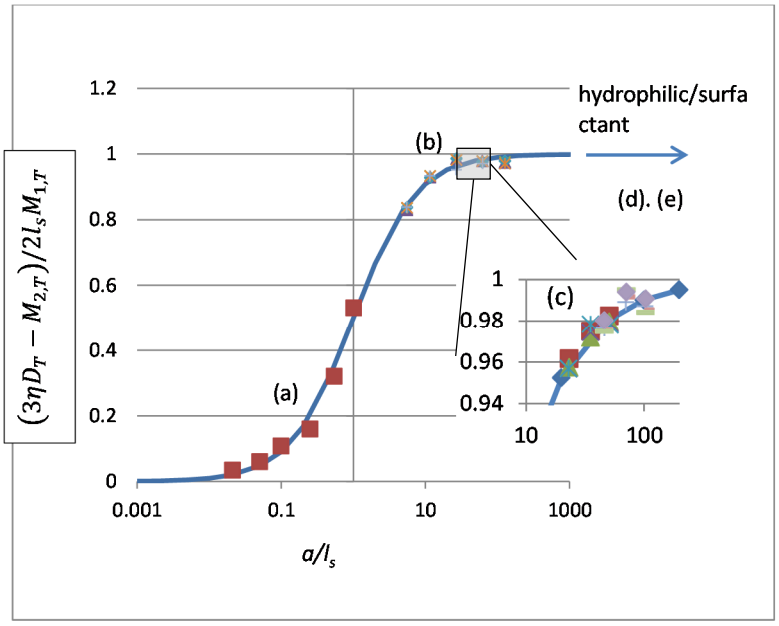

Figure 4-10 Thermophoretic mobility, D_T, of theoretical value from Eq. (3.17) and the fitted data of (a) Duhr and Braun (b) Braibanti et al. (no surfactant) (c) Eslahian and Maskos (d) Braibanti et al. (with surfactant) (e) Vigolo et al.

All the fitted slip length and surface condition can be found in Table 4.1. As we can see, all the hydrophobic surfaces are related to a finite slip length, as the hydrophilic/surfactant surfaces related to no slip length. Furthermore, according to the completed set of data provided by Braibanti et al., we can show the relationship of how the first and second moment related to temperature in Figure 4-11; they both ramp up when temperature rise. This can be related to the size mediated turn over once the upper and lower limit were in different sign.

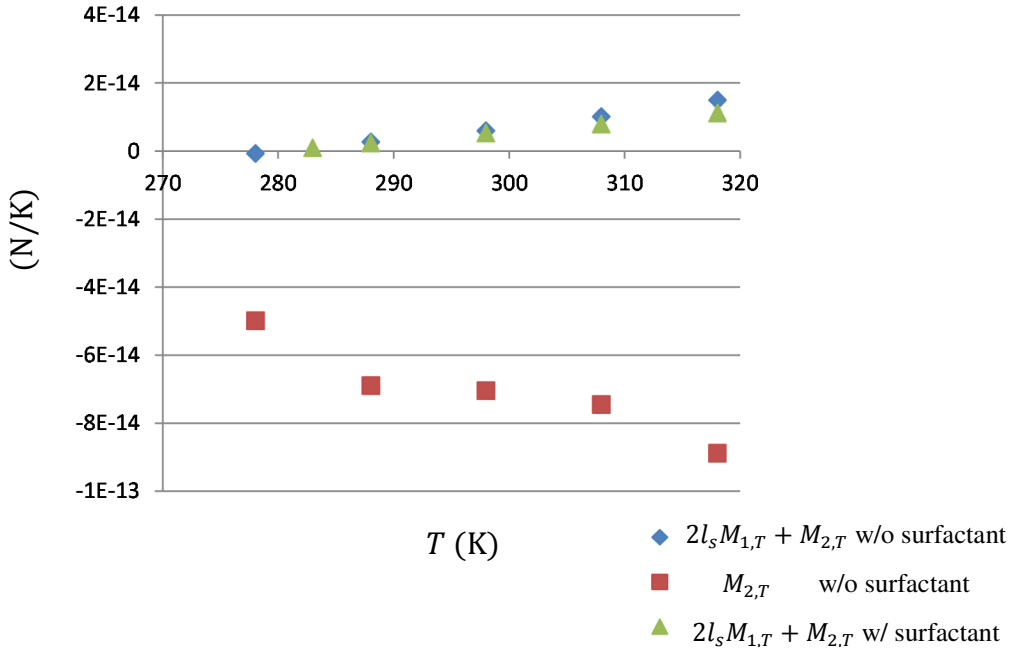

Figure 4-11 Fitted first moment and second forcemoment from Braibanti et al.at different temperature of both the case with or without surfactant

In summary of this section, we have derived a full, analytical solution of thermophoresis of a spherical colloidal particle with Navier's hydrodynamic slip by applying the reciprocal

theorem. The solution is further expanded in a full multipole-series form. It makes no assumption more than the Stokes creeping flow theory in contrast to the classical approximate boundary layer approach anchoring at the concept of slip velocity. We point out that in the classical approach of phoresis, the equilibrium condition is not generally satisfied within the whole boundary layer. A master curve of thermophoretic mobility is introduced as a function of particle size and slip length. Experimental data available from the literature are fitted to this curve. It demonstrates a profound role of Navier's slip underpinning the size effect of thermophoresis

4.5 Summary

This chapter provided an analytical solution that involved much lesser unnecessary assumption comparing to the solution given by previous studies. In comparison, this approach provides a continuum solution that cross the entire fluid domain at once. Thus for dealing with the highly skewed local stress profile, we provide a safer approach to avoid integrated mismatch from using local stress profile. This analytical solution also provide a direct link between radio direction body force with the phoresis speed including the impact of body force induced shear stress to slip boundary condition, which is also not provided by other studies.

The advantages of the analytical solution described above have been demonstrated with 3-9 surface potential. With the intriguing results, many phoresis event that hold size effect or temperature dependency can be reconsidered. As we do in Section 4.4, a review of the experimental work of thermophoresis has been done. Most of the event can be mapped onto the master curve.

Chapter 5

Phoresis with Near-surface Phase Transition

The theory of phoresis based on the Boltzmann distribution of active agents is able to describe most cases where active agents are dilute. If this is not the case, a real fluid model for active agent distribution around a particle is required. The term, real fluid, is referred to a deviation from ideal gas law, by which the Boltzmann distribution is derived. The ideal gas law is applicable to the case where molecules are dispersed purely by their thermal energy with the repulsive nature. In contrast, a real fluid model includes more than the pure repulsive collision interaction for the active agent molecules. It may include attractive of the active agent molecules or between active agent molecules and other solutions. Thus a real fluid model may show a non-linear relation between to temperature, pressure, and mass density, which may even include a lower energy state with phase transition. Real fluid behavior under external forces can generally deviate from ideal gas law, which has been well appreciated in the case of electrochemical double layer near a strongly charged surface(Helmholtz 1853). The deviation can perhaps be no more manifested than near the critical point of phase transition. It can result in significant changes of mass density, viscosity, and interfacial body force field that all can impact the phoretic event. For instance, a solid particle can adsorb vapor to form a thin liquid film on its surface, with thickness generally varying with temperature and pressure, as illustrated in Figure 5-1(a). When subjected to a temperature gradient, osmotic flow can be induced in the liquid film as well as in the surrounding vapor, as shown in Figure. 5.1(b). In order to maintain the equilibrium film thickness, an interesting phenomenon may occur where a normal vapor flux is generated in or out of liquid film surface to compensate the loss of liquid or to reduce the excessive liquid, depending on the direction of osmotic flux gradient, as shown in Figure 5-1(c). In this chapter, we investigate the phoresis in a near-critical water-steam system. Since the water-steam system only holds a single component, H_2O, we will only discuss the thermophoresis in this chapter; however, the concept should hold when dealing with

diffusiophoresis or electrophoresis with high active agent concentration. This phoretic problem due to interfacial forces is solved in two steps: (a) in section 5.1, we derive interfacial forces based on an equation of state (EOS) while holding off flow; (b) in section 5.2 and 5.3 we solve the interfacial flow problem for particle speed, the same as in the previous Chapter of ideal gas law.

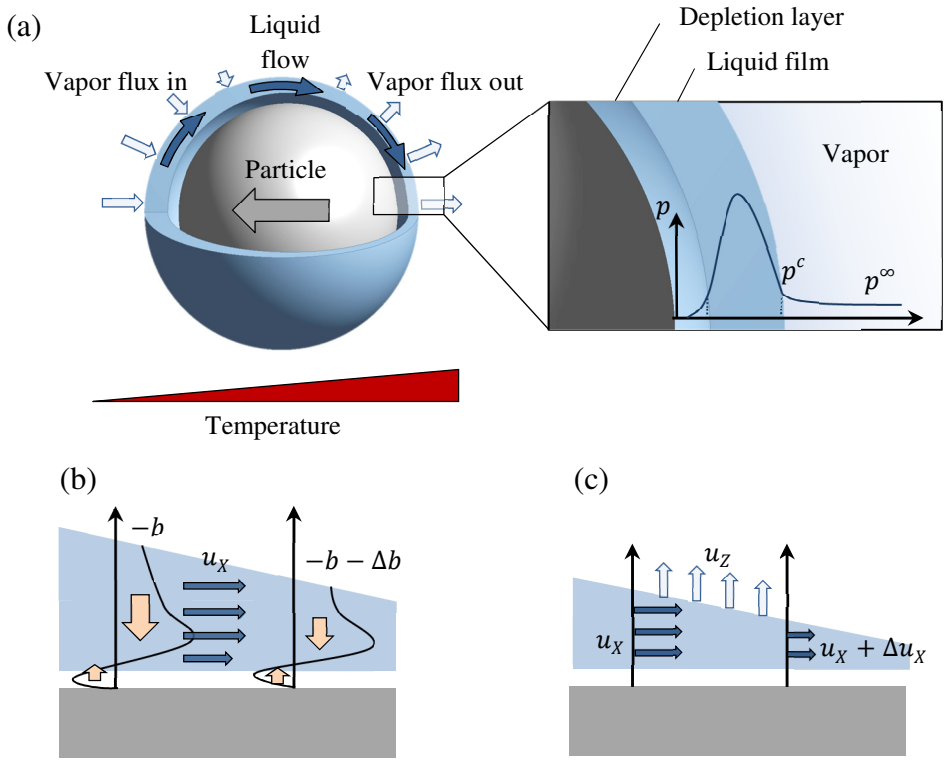

Figure 5-1 (a) Schematic showing a particle with near-surface phase transition moving in real fluid subjected to a temperature gradient; (b) Osmotic flow due to nonuniform interaction force field along particle surface; (c) Normal vapor flux due to mass flux gradient in liquid film.

5.1 Interfacial Structure of Water-Steam on a Solid Surface

Instead of assuming a Boltzmann-type force field, we derive the fluid-solid interaction force field based on the water/steam EOS, i.e., in real fluid. A hypothetical solid surface is though considered, which exerts forces on water/steam molecules by a reduced potential: $\Phi(Z)$, where Z is the normal distance apart from surface. By holding off flow, the equilibrium condition along the surface normal direction requires

$$p_{,Z} - b_Z = 0 \tag{5.1}$$

where p is the hydrostatic pressure, b_z is the body force density, and the subscript comma indicates the partial differentiation with respect to indices that follow. The body force density is given by

$$b = -\frac{\rho}{M}\Phi_{,z} \tag{5.2}$$

where ρ is the mass density and M is the molar mass of water. It is assumed that there is only normal force component resulting from the fluid-solid interaction. The water/steam EOS expressing ρ in terms of temperature T and p has been studied extensively; the version of Tanaka (2000) is adopted. An illustrative contour plot of Takana EOS, $p = p(\rho, T)$, is shown in Figure 5-2, where each line stands for the equilibrium state of a constant temperature. Figure 5-2(b) shows how phase change may occur with the EOS. Assuming uniform T along the surface normal direction, the above formulated problem can be solved for distribution of ρ, b_z and p given particle surface properties (δ and ε), T and remote p^{∞}.

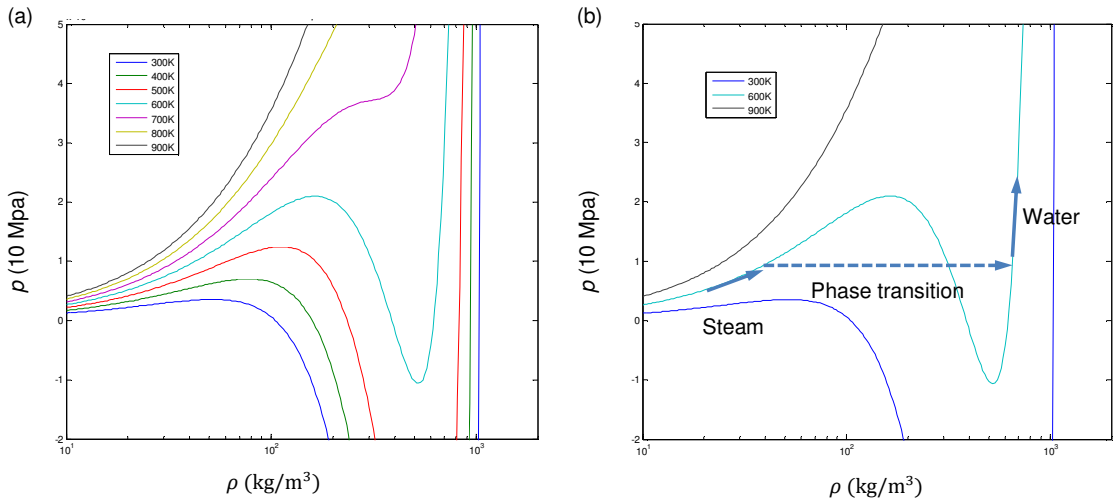

Figure 5-2 Equation of state for real water: Tanaka (2000) model (a) isothermal contour (b) path of phase transition

With the EOS, $p = p(\rho, T)$, the interfacial structure can be found by solving Eqs. (5.1) and (5.2). We present the solution with a L-J type surface potential of $\Phi = \frac{\varepsilon}{2}\left[\left(\frac{\delta}{z}\right)^9 - 3\left(\frac{\delta}{z}\right)^3\right]$. The solution was obtained by numerical integration of the equations from Z = 5 nm to 0 nm with an adaptive meshing size of no larger than 0.01 nm (backward difference). Figure 5-3 shows three types of a typical density profile with the surface potential of δ = 0.375 nm and ε = 1.73 kJ/mol under ambient pressure of 1 bar. As we know, the boiling temperature of 1 bar is at 100 °C; thus, the profile of 100 °C and 118 °C are easy to understand, which represent the water and steam forms, respectively, except at the vicinity of surface. Due to the strong short-range repulsive interaction, the pressure drops to zero near the surface, leaving a depletion vapor zone. However, in the case of temperature near saturation, like 106 °C and 118 °C, the surface force is able to abrogate high enough pressure to transform steam into a water film. The film thickness is dependent on temperature and strength of the surface. This film profile only

presents the case when the bulk pressure and temperature is slightly (depending on the strength of surface potential) above the condensation temperature.

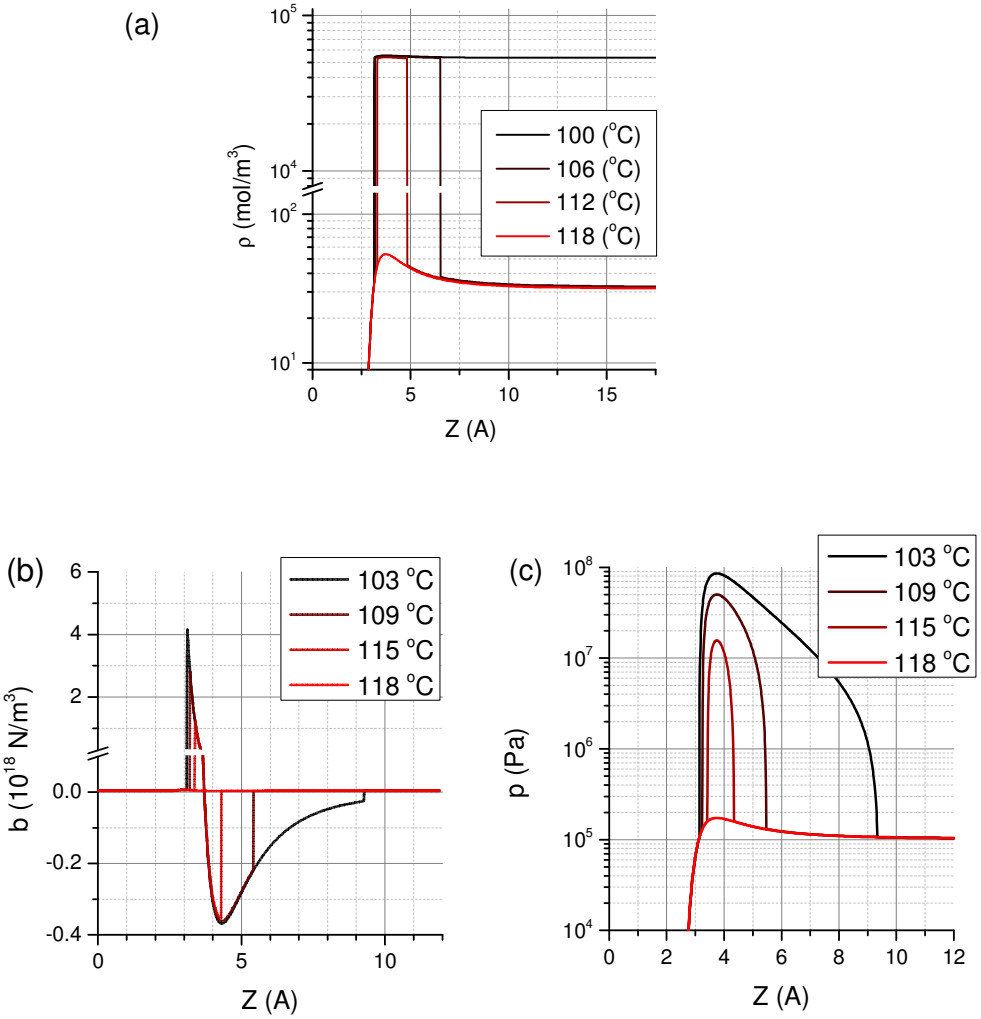

Figure 5-3 (a) Mass density, (b) body force density, (c) hydrostatic pressure, of near surface water-steam, with surface potential of δ = 0.375 nm, ε = 1.73 kJ/mol and the remote pressure p^{∞} = 1 bar.

Figure 5-4 shows the evolution of phase boundaries with temperature at three different surface potential strengths ε = 0.55, 1.73, and 5.5 kJ/mol, and with fixed δ = 0.375 nm and

p^{∞}=1 bar. It can be seen that the depletion layer thickness changes slightly from 0.312 nm to 0.342 nm, when ε and T change. In contrast, the water film thickness varies sensitively with temperature and surface potential strength, especially near the critical temperature. At condensation temperature T = 100 °C, the water thickness is infinite, as expected for a spontaneous phase transition around the surface. For the three surface potential strengths, the water film disappears at T = 104 °C, 114 °C, and 148 °C, respectively. These surface potential strengths could be related to the cases of highly hydrophobic, moderately hydrophobic and slightly hydrophilic surfaces, respectively (Trudeau, Jena et al. 2009). It might be worth noting that we intentionally confine our analysis in this range of surface conditions. For more hydrophilic surfaces, the ρ -p-T-based EOS adopted herein may be insufficient to capture the molecular structural changes, such as strong water molecule ordering near such a highly adsorbing surface (Argyris, Tummala et al. 2008).

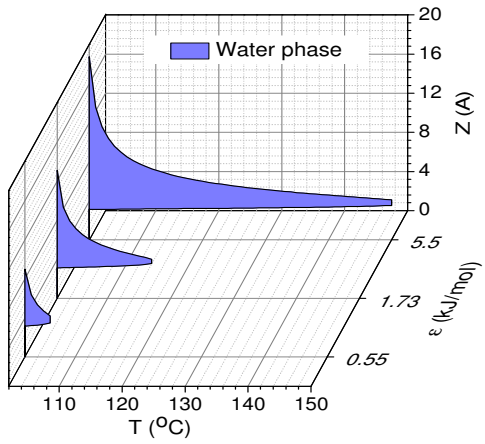

Figure 5-4 Diagram of vapor-water phase boundaries with varying temperature for surface potential strength ε = 0.55, 1.73, and 5.5 kJ/mol. The remote pressure p^{∞} = 1 bar. The surface potential parameter δ = 0.375 nm.

With the understanding of the near surface structure, we present below the derived loading parameters including the first and second moments of interfacial forces, $M_1 = \int_0^\infty Z b_r dZ$ and $M_2 = \int_0^\infty Z^2 b_r dZ$, as a function of temperature and remote pressure in the case of surface potential with δ = 0.375 nm and ε = 10 kJ/mol. Note that the force moments documented here do not fully determine the phoretic mobility in the case of a complex water film structure. While they are related to two terms of the phoretic mobility as shown in the previous chapter, there appears to be another important (possibly more important) term in the present case of a water film in steam.. Figs. 5.5(a-d) show the surface and contour plots of the first and second moments over the p-T domain with 233.15 K< T < 1100 K and 1 kPa< P < 100 MPa where Takana's EOS is accurate. It is shown that both M_1 and M_2 are much larger in magnitude while in water phase than in steam phase since they are proportional to the mass density and that of water phase is over a thousand times greater than the latter. From Eq. (3.17) we understand that the propelling force of thermophoresis is the partial derivatives of the first and second force moments with respect to temperature, $M_{1,T}$ and $M_{2,T}$. They are extremely large at the phase boundary between steam and water as it shifts when temperature changes. However, Eq. (3.17) with terms of $M_{1,T}$ and $M_{2,T}$ alone is not able to predict the phretic mobility since the abrupt variation of mass density at the phase boundary violates the incompressibility assumption in deriving Eq. (3.17) (and typically made in all previous approaches). Our novel approach to this situation will be introduced in the next section.

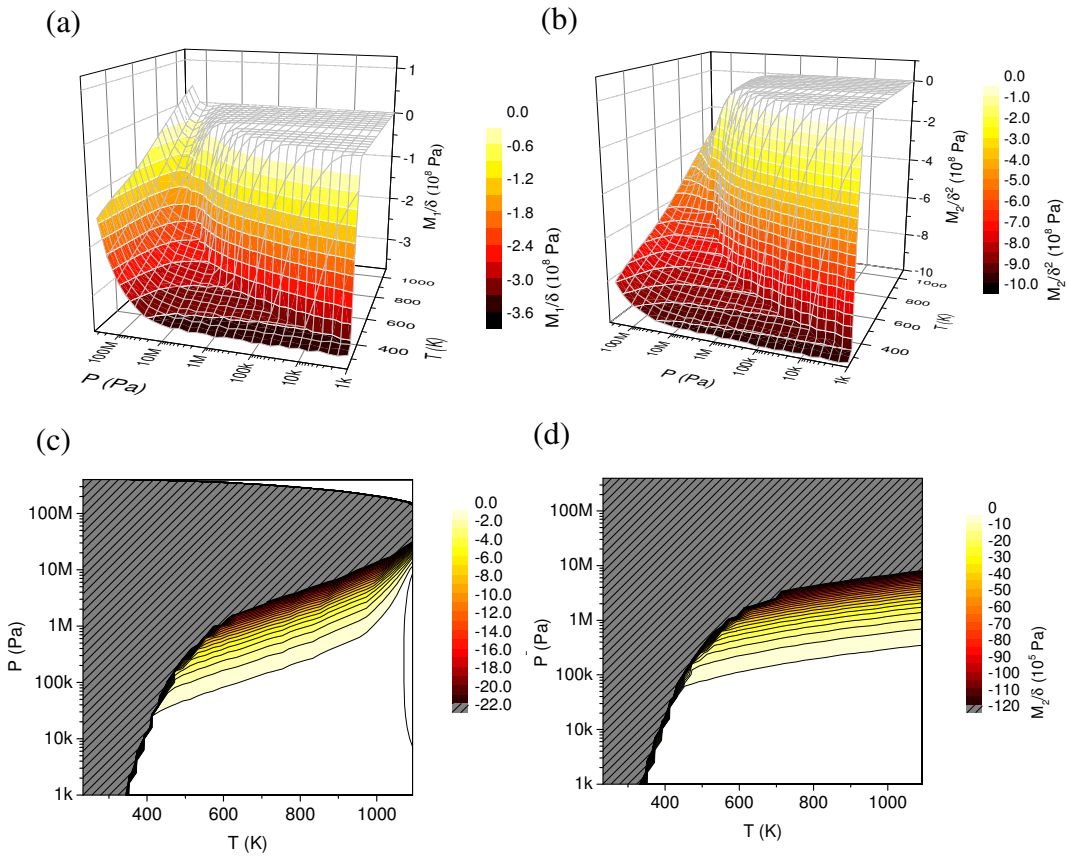

Figure 5-5 Surface and contour plots of the first and second force moments under surface potential well depth of ε=10 kPa/mol: (a) M_1, (b) M_2, (c) M_1 of steam only case, and (d) M_2 of steam only case

The above results are also plotted in 2D diagram in terms of temperature for various remote pressures, as shown in Figure 5-6. Figure 5-6 showed a close look of the merging zone between the steam and water region. Due to the highly incompressible of water phase, the force moment before phase change is stacked on each other. It is very clear that the magnitude of the partial difference of force moments, $M_{1,T}$ and $M_{2,T}$, is the largest within the merging zone, after

that is the pure water region, the force moment magnitude of pure steam region is nearly nothing comparing to the other two.

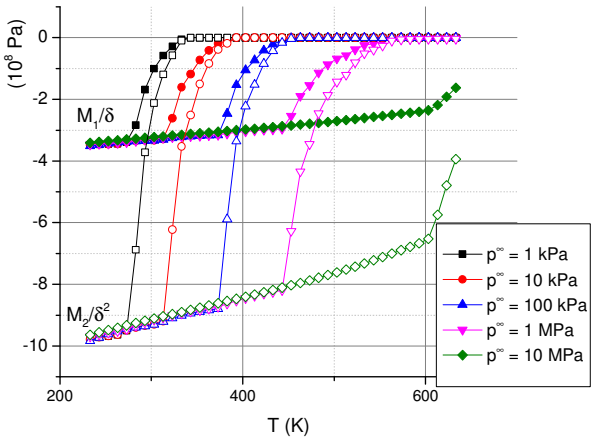

Figure 5-6 First and second moment under surface potential well depth of ε=10k Pa/mol

Here we investigate another issue which is how much difference would real gas make different from ideal gas if there is no any phase transition near the surface. The answer is in Figure 5-7, which list three different strength of surface potential, ε = 2 kJ/mol, 5 kJ/mol, and 10 kJ/mol. It is very clear that the deviation is larger when the temperature is lower, which the steam is closer to condensation. Also, higher remote pressure will push it closer or even cross the critical point, where the phase transition is not clear and ideal gas model prediction is not valid as we expected.

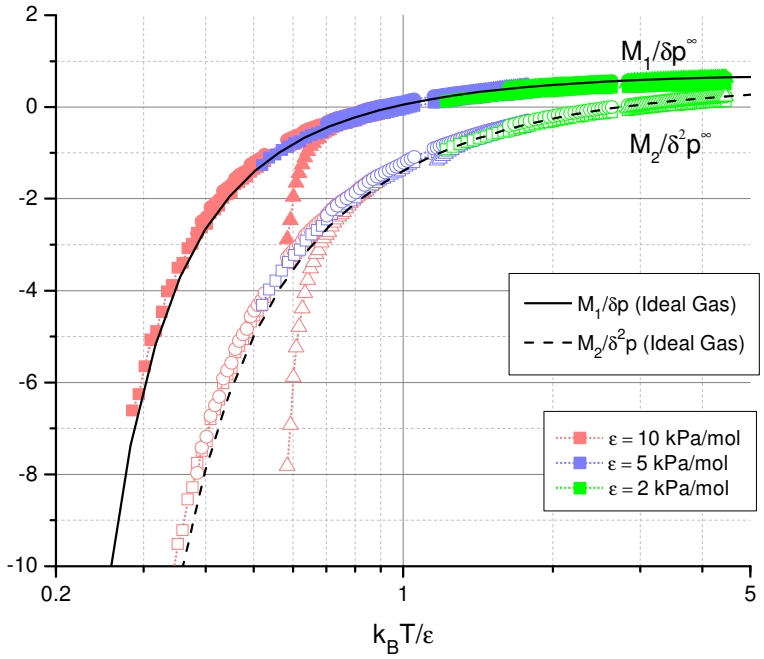

Figure 5-7 First and second moment of pure steam case with comparing to ideal gas model, ■ indicate profile of p^∞= 1 kPa, ⊙ is for p^∞ = 100 k Pa, and Δ is for p^∞ = 10 MPa

5.2 Thermophoresis with Near-surface Water Film

As we stated in the previous section, the thermophoresis involving the water film is largely change in fluid density and viscosity near the particle surface, thus Eq. (3.17) is not approximate since the violation of incompressible and uniform viscosity assumption. The illustrative of interfacial structure can be find in Figure 5-1. In this section we started with Eq. (3.16), which is the most general case that able to handle fluid with density and viscosity change. Here, we rewrite Eq. (3.16) just for convenient,

$$\widehat{\boldsymbol{F}}\cdot\boldsymbol{U}=\iiint_V\left(\widehat{\boldsymbol{u}}-\widehat{\boldsymbol{U}}\right)\cdot\boldsymbol{b}dV+\iiint_V\frac{\eta^\infty-\eta}{\eta}\nabla\widehat{\boldsymbol{u}}:\boldsymbol{\sigma}dV-\iiint_V\hat{p}\nabla\cdot\boldsymbol{u}dV. \tag{5.3}$$

In order to derive the particle phoretic speed without resorting to a full solution of the problem, we simplify the interfacial structure, as shown in Figure 5-8. The reduced interfacial structure consists of a depletion vapor layer of thickness equal to *d*, a water film of thickness equal to *h*, and bulk steam beyond. We assume that the mass density is uniform in both of the water film and the bulk steam, denoted by ρ^w and ρ^g, respectively.

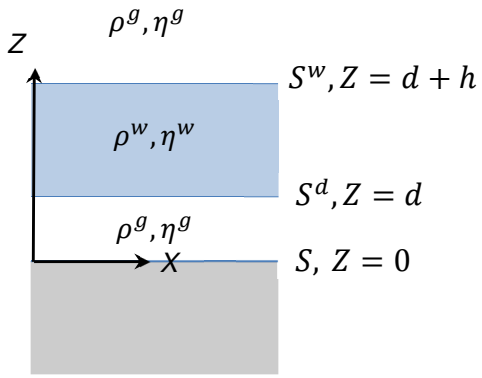

Figure 5-8 Simplified model of interfacial water-steam structure.

Under this assumption, the steady-state mass conversion law $\boldsymbol{\nabla} \cdot [\rho(\boldsymbol{u} - \boldsymbol{U})] = 0$ is reduced to $\boldsymbol{\nabla} \cdot \boldsymbol{u} = 0$, which is the incompressibility condition to close the Stokes flow formulation for both water and steam in their own domains. However, the mass conversion law at the phase boundary leads to

$$\rho^g(\boldsymbol{u}^g - \boldsymbol{U}) \cdot \boldsymbol{n}|_{S^w - S^d} - \rho^w \boldsymbol{\nabla}_S \cdot \left[\int_d^{d+h} (\boldsymbol{u} - \boldsymbol{U}) dZ\right] = 0, \tag{5.4}$$

assuming that *h* is small compared to the particle size, where $\boldsymbol{u}^g$ is the velocity of steam at the phase boundaries, $\boldsymbol{\nabla}_S$ is the two-dimensional del operator along particle surface *S*, $\boldsymbol{n}$ is taken to be the outward normal unit vector on *S*, and S^w and S^d are the upper and lower surfaces of the water film. It means that if film water flux $\rho^w h(\boldsymbol{u} - \boldsymbol{U})$ is non-uniform tangent to the film, there

would appear normal steam flux $(\boldsymbol{u}^g - \boldsymbol{U}) \cdot \boldsymbol{n}$ in or out of the film surfaces. This normal steam flux may become significant due to the huge ratio of ρ^w/ρ^g. The value of ρ^w/ρ^g = 1450 will be used in later calculation; it is calculated from ρ^w = 53650 mol/m^3 and ρ^g = 37 mol/m^3 at T = 100 ^{o}C and p = 1 bar. This phenomenon is essentially a result of the extremely high compressibility of water/steam near their critical point of phase transition. We also assume the viscosity is uniform in both of the steam (inside the depletion layer and in the bulk) and the water (in the water film), denoted by η^g and η^w, respectively This simplification is well justified by the fact that both η^g and η^w are sensitively dependent on T but not on p or ρ (Cooper and Dooley 2008). The empirical formulas of viscosity used later are given by $\eta^g = 8.45 + 0.0382T$ and $\eta^w = 481 - 2T$, where η is in μPa-s and T is in ^{o}C. They are obtained for 100 ^{o}C < T < 150 ^{o}C from Table 8 in Sengers and Kamgar-Parsi (1984). Under these assumptions, the last two terms on the right-hand side of Eq. (4.3) are reduced to surface integrals as

$$\iiint_V \frac{\eta^\infty - \eta}{\eta} \nabla\hat{\boldsymbol{u}} : \boldsymbol{\sigma} dV = \left(\frac{\hat{\eta}}{\eta^w} - \frac{\hat{\eta}}{\eta^g}\right) \iint_{S^{w-S^d}} \boldsymbol{n} \cdot \boldsymbol{\sigma} \cdot \left(\hat{\boldsymbol{u}} - \hat{\boldsymbol{U}}\right) dS, \text{ and} \tag{5.5}$$

$$-\iiint_V \hat{p} \nabla \cdot \boldsymbol{u} dV = -\iint_{S^{w-S^d}} \hat{p} (\boldsymbol{u}^g - \boldsymbol{U}) \cdot \boldsymbol{n} dS, \tag{5.6}$$

respectively. In the second term, the integral over S^w can be neglected because $\boldsymbol{n} \cdot \boldsymbol{\sigma}$ should be trivial at the upper water film surface. In the third term, $\hat{p}$ at S^w and S^d can be reasonably approximated by $\hat{p}$ at S so that the mass conservation condition at the phase boundary derived above can be substituted, which would result in

$$-\iiint_V \hat{p} \nabla \cdot \boldsymbol{u} dV = \frac{\rho^w}{\rho^g} \iint_S \hat{p} \boldsymbol{\nabla}_S \cdot \left[\int_d^{d+h} (\boldsymbol{u} - \boldsymbol{U}) dZ\right] dS. \tag{5.7}$$

Thus, we obtain

$$\hat{\boldsymbol{F}} \cdot \boldsymbol{U} = \iiint_V \frac{\hat{\eta}}{\eta} \boldsymbol{b} \cdot \left(\hat{\boldsymbol{u}} - \hat{\boldsymbol{U}}\right) dV + \left(\frac{\hat{\eta}}{\eta^g} - \frac{\hat{\eta}}{\eta^w}\right) \iint_{S^{w-S^d}} \boldsymbol{n} \cdot \boldsymbol{\sigma} \cdot \left(\hat{\boldsymbol{u}} - \hat{\boldsymbol{U}}\right) dS + \frac{\rho^w}{\rho^g} \iint_S \hat{p} \boldsymbol{\nabla}_S \cdot \left[\int_d^{d+h} (\boldsymbol{u} - \boldsymbol{U}) dZ\right] dS. \tag{5.8}$$

Similarly to the classical formulation of osmosis (Derjaguin, Dukhin et al. 1972), the stress and velocity fields in the interphase may be reasonably approximated by those resulting

from the interfacial force field $\boldsymbol{b}$ alone. The approximate expressions of σ, p, and $\boldsymbol{u}$ in terms of $\boldsymbol{b}$ (or $\boldsymbol{b}_{,X}$) are given in

$$p = -\int_Z^\infty b dZ \tag{5.9}$$

$$\tau = -\int_Z^\infty p_{,X} dZ \tag{5.10}$$

$$u_X = -\int_0^Z \frac{1}{\eta}\tau dZ \tag{5.11}$$

By substituting these approximate fields and the auxiliary solution of Eq. (3.17-20), we obtain the first term of Eq. (5.8) as

$$\frac{\eta^s}{\eta^w}\iiint_V \boldsymbol{b}\cdot\left(\widehat{\boldsymbol{u}}-\widehat{\boldsymbol{U}}\right)dV = -2\pi a\frac{\eta^g}{\eta^w}\left(\int_d^\infty Z^2 b_{,T} dZ\right)T_{,z}. \tag{5.12}$$

where the lower case z is define the same as in Chapter 3 is the direction of axial direction of spherical global coordinate, and same coordinate will apply on the following notation of θ. After put the auxiliary solution in, the second term of Eq. (4.8) can be written as

$$\begin{aligned}&-\iint_{S^d}\eta^g\left(\frac{1}{\eta^g}-\frac{1}{\eta^s}\right)\boldsymbol{n}\cdot\boldsymbol{\sigma}\cdot\left(\widehat{\boldsymbol{u}}-\widehat{\boldsymbol{U}}\right)dS^d\\ &=\left(1-\frac{\eta^g}{\eta^w}\right)\iint_{S^d}\left[\frac{-3}{2}\widehat{U}\cos\theta\left(\frac{d}{a}\right)^2(-p^c)+\frac{3}{2}\widehat{U}\sin\theta\left(\frac{d}{a}\right)\tau\right]dS^d.\end{aligned} \tag{5.13}$$

Since the pressure on the S^d is always the condensation pressure p^c, which makes little effect on this equation. The effect of the p^c induced term can be found in Figure 5-9, the definition of D_{T0} is comparable with the definition in Eq. (5.17) as $D_{T0} = -\frac{1}{3}\left(\frac{1}{\eta^g}-\frac{1}{\eta^w}\right)d^2 p^{cri}{}_{,T}$ that deduct from the first term of Eq. (5.13). One can compare the difference of the magnitude in the next section and find it negligible. In order to make to description more concise, it will be neglect in the next equation.

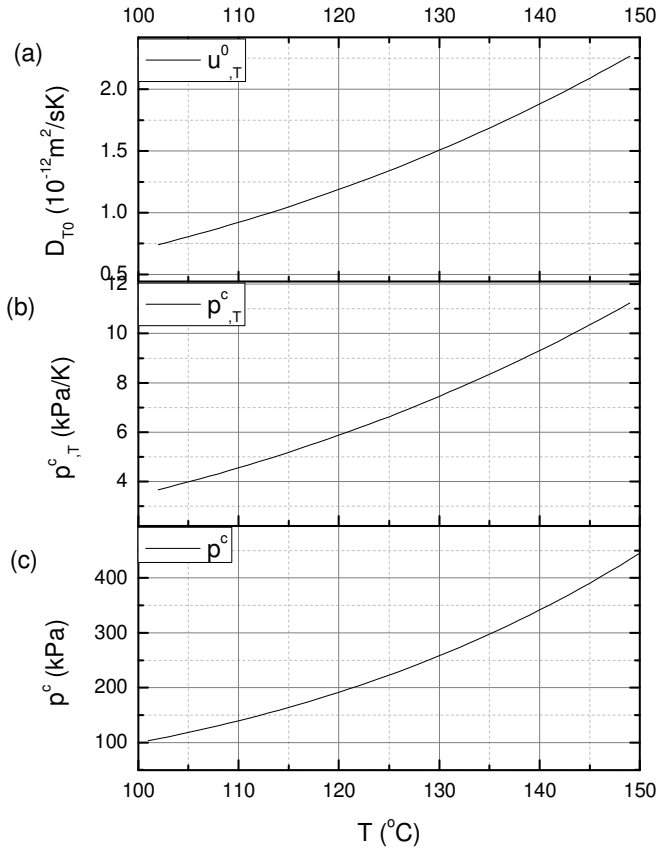

Figure 5-9 (a) Thermophorebility induced by condensation pressure on the lower end of the water film, and the relative (b) partial differentiation of condensation pressure to temperature and (c) the condensation pressure. All the profiles in p^{∞} = 1 bar.

Here we assume the local profile change is small that can by approximate by linear as $\tau|_{S^d} = -\int_d^{\infty} p_{,T} dZ\,(-\sin\theta)T_{,z}$ (higher order term will vanished when integrate), thus Eq. (5.13) can be further reduced by substitute the highest order Taylor's expansion term of auxiliary solution $\hat{u}_r - \hat{U}_r\big|_{Z=d} = \frac{-3}{2}\hat{U}\cos\theta\left(\frac{d}{a}\right)^2$ as

$$\left(1-\frac{\eta^g}{\eta^w}\right)\iint_{S^d}\left[\frac{3}{2}\widehat{U}\sin\theta\left(\frac{d}{a}\right)\tau\right]dS^d$$

$$=\left(1-\frac{\eta^g}{\eta^w}\right)\frac{3}{2}\widehat{U}\iint_{S^d}\left[\frac{d}{a}\sin^2\theta\int_d^{d+h}p_{,T}dZ\,T_{,z}\right]dS^d$$

$$=\left(\frac{\eta^g}{\eta^w}-1\right)2\pi a\widehat{U}\left(2d\int_d^{d+h}Zb_{,T}dZ\right)|\nabla T| \tag{5.14}$$

Also, Eq. (5.7) can be expressed into the local notation as

$$\boldsymbol{\nabla}_S\int_d^{d+h}(\boldsymbol{u}-\boldsymbol{U})dZ=\frac{-1}{2\pi a\sin\theta}\frac{\partial}{a\partial\theta}\left(2\pi a\sin\theta\int_d^h u_X dZ\right)\frac{\rho^w}{\rho^g}$$

$$=-\left(\frac{\cos\theta}{a\sin\theta}\int_d^h u_X dZ+\left(\int_d^h u_X dZ\right)_{,T}(-\sin\theta)T_{,z}\right)\frac{\rho^w}{\rho^g}$$

$$=\left(\frac{\cos\theta}{a\sin\theta}\left(\int_d^h\int_0^Z\frac{1}{\eta}\int_Z^\infty\int_Z^\infty b_{,T}\,dZdZdZdZ\right)(\sin\theta)T_{,z}+\left(\int_d^h\int_0^Z\frac{1}{\eta}\int_Z^\infty\int_Z^\infty b_{,TT}\,dZdZdZdZ\right)\sin^2\theta\,T_{,z}{}^2\right)\frac{\rho^w}{\rho^g}$$

$$=\left(\frac{\cos\theta}{a}\left(\int_d^h\int_0^Z\frac{1}{\eta}\int_Z^\infty\int_Z^\infty b_{,T}\,dZdZdZdZ\right)T_{,z}-\left(\int_d^h\int_0^Z\frac{1}{\eta}\int_Z^\infty\int_Z^\infty b_{,TT}\,dZdZdZdZ\right)\sin^2\theta\,T_{,z}{}^2\right)\frac{\rho^w}{\rho^g} \tag{5.15}$$

With the near surface approximated auxiliary solution of pressure, $\hat{p}\cong\frac{3}{2a}\eta^g\widehat{U}\cos\theta$, we have

$$-\iiint_V\hat{p}\nabla\cdot\boldsymbol{u}dV=-2\pi\eta^g\widehat{U}\left(\int_d^h\int_0^Z\frac{1}{\eta}\int_Z^\infty\int_Z^\infty b_{,T}\,dZdZdZdZ\right)\frac{\rho^w}{\rho^g}T_{,z} \tag{5.16}$$

Since all three terms of Eq. (5.8) are reduced into Eq. (5.12), (5.14), and (5.16), by substituting the last piece of auxiliary solution of $\widehat{\boldsymbol{F}}=6\pi a\eta^s\widehat{\boldsymbol{U}}$, we finally have

$$\boldsymbol{U}=-D_T\nabla T=-(D_{T1}+D_{T2}+D_{T3})\nabla T, \tag{5.17a}$$

$$D_{T1}=\frac{2d}{3}\left(\frac{1}{\eta^g}-\frac{1}{\eta^w}\right)\int_d^{d+h}Zb_{,T}dZ, \tag{5.17b}$$

$$D_{T2}=\frac{1}{3\eta^w}\int_d^{d+h}Z^2b_{,T}dZ, \tag{5.17c}$$

$$D_{T3}=\frac{1}{3a}\frac{\rho^w}{\rho^g}\int_d^{d+h}\int_0^Z\frac{1}{\eta}\int_Z^\infty\int_Z^\infty b_{,T}\,dZdZdZdZ, \tag{5.17d}$$

where D_T is termed the thermophoretic mobility. In deriving the above equation, it is assumed that the interfacial force $\boldsymbol{b}$ is only important within the water film and that it is only nontrivial normal to particle surface (denoted by *b*). Also, it is assumed that the temperature difference on particle surface is small so that the effects of all second derivatives of a field are trivial. It can be seen that D_{T1} and D_{T2} are due to the temperature derivatives of the first moment $M_1\equiv$

$\int_d^{d+h} ZbdZ$, and the second moment $M_2 \equiv \int_d^{d+h} Z^2 bdZ$, respectively. D_{T3}, which is more complicated, is due to the temperature derivative of a driving force equivalent to the third moment. The effectiveness of $M_{1,T}$ requires $\eta^g \neq \eta^w$, which essentially is what Ajdari and Bocquet (XXXX) have considered. It is scaled by d^3, but is proportional to $\left(\frac{1}{\eta^g} - \frac{1}{\eta^w}\right)$. The second term D_{T2} due to $M_{2,T}$ is the classical solution (Anderson XXXX). It is scaled by d^3. Finally, the last term D_{T3} is what we introduce newly in the present work. It is scaled by d^4/a, which is a rank lower (by d/a, typically $\ll 1$) than the previous two terms. However, the multiplier, ρ^w/ρ^g, which is huge (> 1000), may make up the scaling shortage. It might be worth noting that xxx observed a $1/a$ scaling behavior of their catalytically driven nanoparticles, especially at small particle sizes.

5.3 Thermophoresis with Near-surface Water Film: Example of 3-9 Potential

In order to examine how all three terms of Eq. (5.17) interact with the surface potential, again we employed a 3-9 surface potential as $\Phi = \frac{\varepsilon}{2}\left[\left(\frac{\delta}{Z}\right)^9 - 3\left(\frac{\delta}{Z}\right)^3\right]$. Now, we can find $M_{1,T}$ and $M_{2,T}$ of the 3-9 surface potential in Figure 5-10 and Figure 5-11 for the cases of δ = 0.375 nm, ε = 0.55, 1.73, and 5.5 kJ/mol, which all required in Eq. (5.17b and 5.17c). Apparently, the force moment and its partial derivative of temperature ramped up when closer to 100 °C since at 100 °C the water film extend to infinity as the entire fluid domain is in water form. Even the surface potential strength is much different in all three cases, the partial derivative I similar in magnitude once the water film is form. It is because of the larger the surface potential strength, the film stretch farther from 100 °C, which makes the partial derivative of temperature smaller that even out the effect of larger force induced by stronger surface potential.

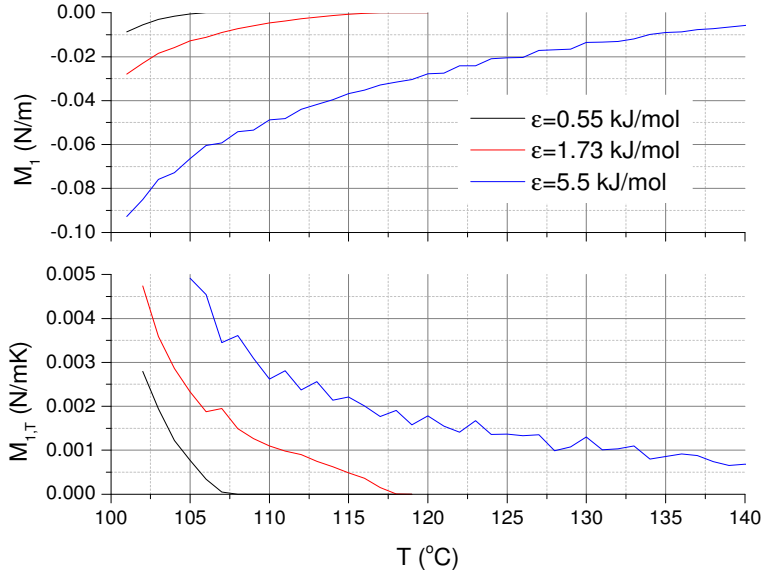

Figure 5-10 First force moment M_1 and its partial differetiation of temperature $M_{1,T}$

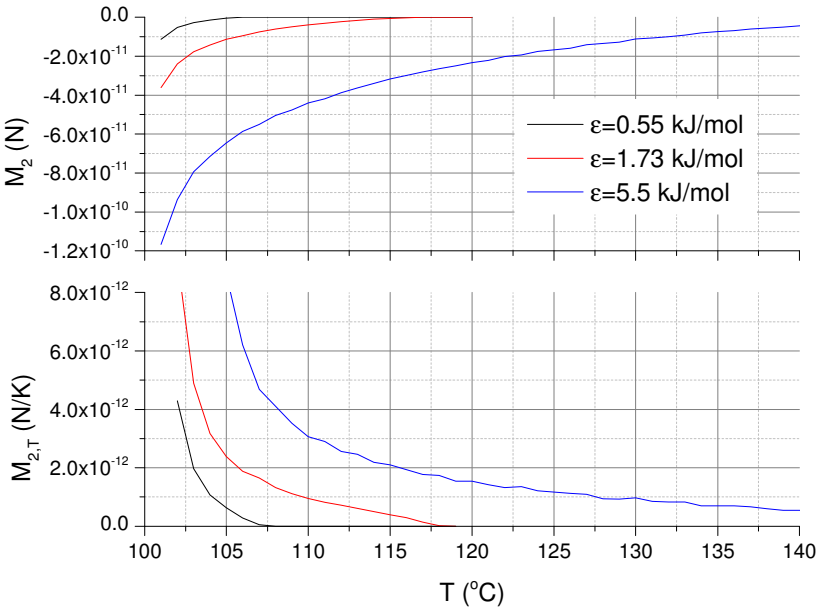

Figure 5-11 Second force moment M_2 and its partial differentiation of temperature $M_{2,T}$

The local solution that used in Eq. (5.9-11) can be found in Figure 5-12 as the case of ε = 1.73 kJ/mol, δ = 0.375 nm, and p^{∞} = 1 bar. It is very clear that the film thickness cut off the local profile that makes the difference between temperature, thus the $p_{,T}$ profile is similar with step function. Consequently, it formed the triangular shape of $\tau_{,T}$.

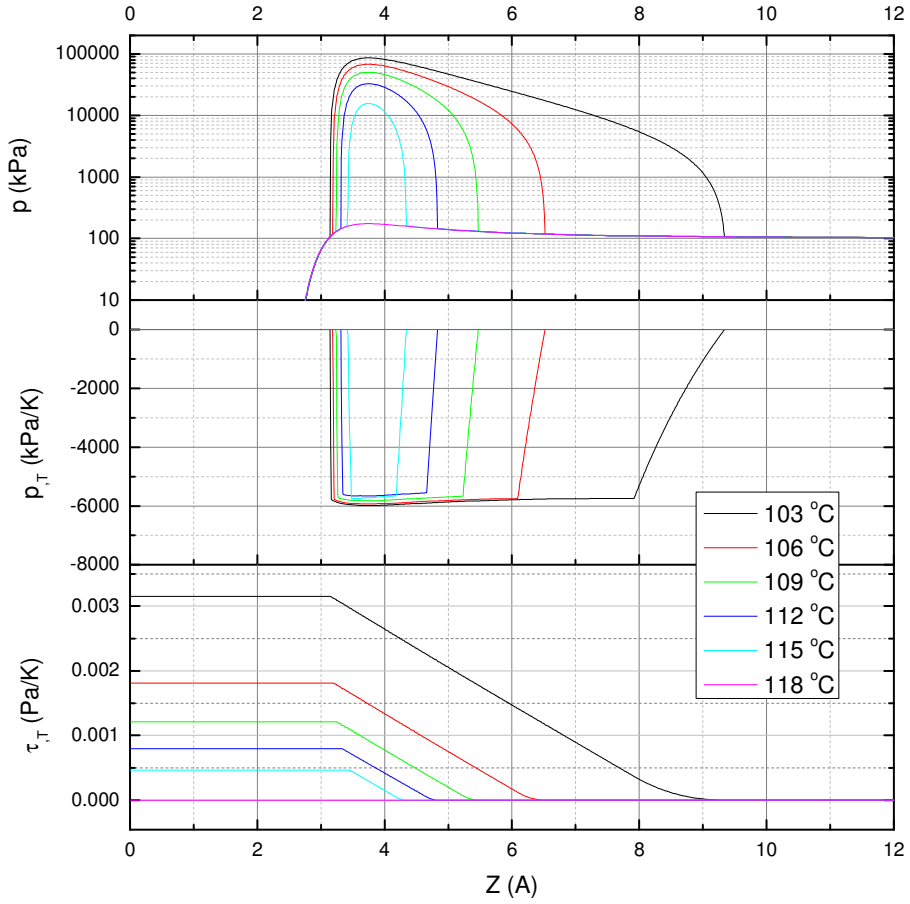

Figure 5-12 Local solution used in Eq. (5.9-11) for ε = 1.73 kJ/mol, δ = 0.375 nm, and p^{∞} = 1 bar, (a) local pressure p, (b) partial derivative of pressure to temperature $p_{,T}$, and (c) partial derivative of the local shear stress to temperature $\tau_{,T}$

The last local solution needed is the local tangential velocity u_X, which can be found in Figure 5-13 for the case for ε = 1.73 kJ/mol, δ = 0.375 nm, and p^{∞} = 1. The profile directly showed the fact that most velocity has been induced within the depletion layer since the high shear stress and low viscosity.

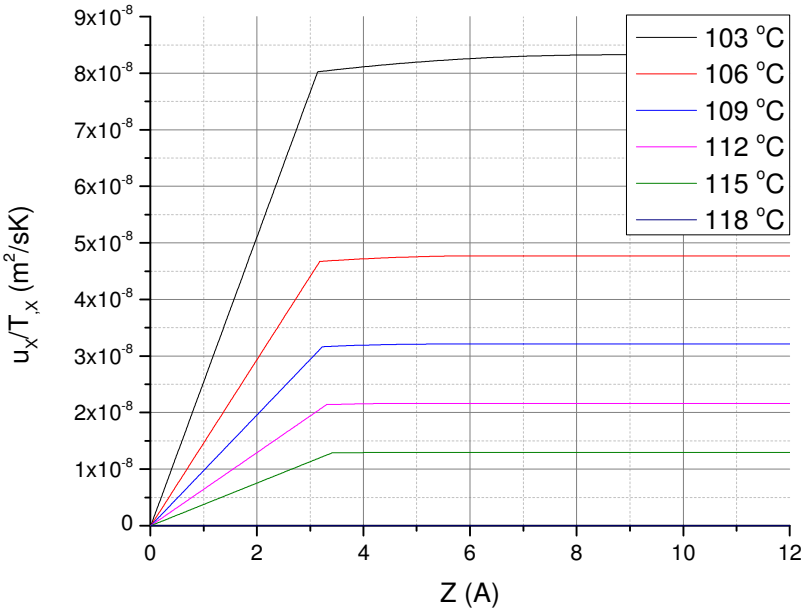

Figure 5-13 Local tangential velocity u_X for the case for ε = 1.73 kJ/mol, δ = 0.375 nm, and p^{∞} = 1.

With the information from Figure 5-10, Figure 5-11 and Figure 5-13 (and the local solution of ε = 0.55 and 5.5 kJ/mol that can be find followed the same method in Figure 5-12 and 5.13), finally we can achieve the thermoporebility as showed in Figure 5-14. We have estimated the three terms of thermophoretic mobility, D_{T1}, D_{T2} and D_{T3} with the interfacial force field predicted from the EOS of water/steam for three surface potential strengths ε = 0.55, 1.73, and 5.5 kJ/mol (Figure 2). For D_{T3}, particle radius is set to be *a* = 100 nm. The results are

shown in Figs. 5(a)-(c). It can be seen that these terms of thermophoretic mobility are effective in the ranges of temperature where a water film is existent (Figure 3). The thermophoretic mobility all rises quickly when the water films thickens near the critical point of liquid-vapor transition and all drops to zero abruptly when the water film disappears. We have also estimated the thermophoretic mobility at higher temperatures after the water film has all evaporated, showing a value of D_T five orders of magnitude smaller than that with the water film. It demonstrates that the near-surface phase transition provides tremendous amount of free energy for thermophoretic mobility. In comparison, D_{T1} is about an order of magnitude greater than D_{T2} in all three cases of different surface condition. It is due to the slip of the water layer on top of the depletion zone, i.e., $\left(\frac{1}{\eta^g} - \frac{1}{\eta^w}\right)$ in Eq. 5b. Most importantly, it can be seen that D_{T3} is greater than D_{T1} and D_{T2} for particles of size a = 100 nm, and the difference is more apparent at lower temperature when the water film is thicker. For particle sizes < 100 nm, the steam condensation/ evaporation effect on D_{T3} would become even greater because it is inversely scaled with a.

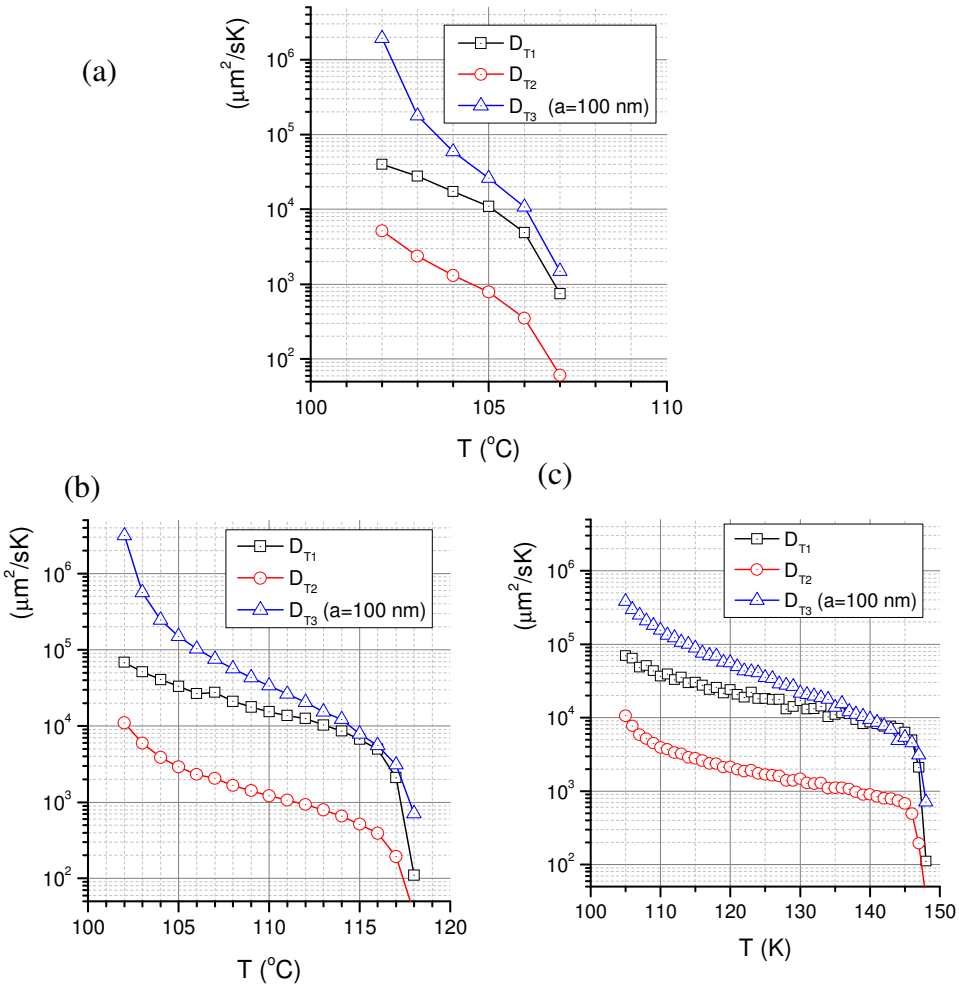

Figure 5-14 D_{T1}, D_{T2} andD_{T3} for ε = (a) 0.55, (b) 1.73, and (c) 5.5 kJ/mol.

5.4 Summary

In summary, we have computed the interfacial force field of water and steam near a LJ-type solid surface based on their EOS. The results show that the pure steam system have little different comparing with ideal gas except the situation high pressure that allow the fluid to go

near or cross the critical point of molecule phase. For the temperature that below condensation temperature of the bulk pressure, a vapor based depletion layer is formed by the near surface repulsive force. This depletion can be one reason of the surface slip boundary condition.

We have introduced a mechanism of possibly significant thermophoresis due to near-surface phase transition for the case of temperature between pure steam and water system. We argued that with a liquid film adsorbed on its surface, the typical osmotic flow in the liquid film would lead to a normal vapor flux in and out of liquid film surface in order to maintain the equilibrium film thickness. We have theoretically shown, with a particle in water/steam as an example, that this vapor flux may result in thermophoretic propulsion. Since it is inversely scaled with particle size, it would become dominant compared to other reported mechanisms as particle size decreases.

Chapter 6

Phoresis in Fluid of Highly Ordering Molecules near Surface

With the introduction of Chapter 4 and 5, we now have a very clear picture of how the interfacial body force pulls the particle toward phoretic direction through the hydrodynamics. However, fluid of reality under the interfacial potential length scale, $d\sim1$ nm, can be anisotropic and non-Newtonian for many different reasons, such as molecule ordering induced anisotropy, surface atomic, or the behavior due to the feature of molecule size, which is not able to be fully described in the simple equation of state as we did in Chapter 5.

Fluid molecules can show a highly ordering interfacial structure. Typically, ions can easily form interfacial structure, which is known as double layer (Helmholtz 1853). Molecules that hold asymmetrically distributed charge, which are defined as polar molecules, i.e., water molecules, also tend to be organized when near interface. Since most fluid molecules are asymmetrical the properties of a highly organized interfacial structure is likely to be anisotropic. The surface lumped anisotropic part of stress is known as surface tension. It can be considered as the response of anisotropic elasticity to the interfacial body force. The impact of this anisotropic preload stress can be found in phoretic mobility (since the isotropic part plays no role to the phoretic mobility), and use it as part of the loading condition.

In this chapter, in order to understand how much the ordering interfacial structure will impact the phoretic mobility, we first examine the interfacial structure of water by molecule dynamics (MD) simulation as an example of asymmetric fluid structure. We demonstrate multiple different interfacial structures that hold by different surface potential. With the profile in hand, we estimate the corresponding thermophoretic mobility (since it is a single component system) by using the anisotropic part of the stress profile from MD simulation as part of the loading condition.

6.1 Molecule Dynamic Simulation of Interfacial Structure

Molecule dynamic (Plimpton 1995) is a type of simulation that tracks the trace of each molecule by Newton's laws of motion. It estimates the forces between each pair of atoms by their position and their interatomic potential. The results can be translated into properties used in continuum thermodynamic or fluid dynamics by the relation of statistical mechanics (Irving and Kirkwood 1950). In this section, we studied the interfacial structure of water as an example of asymmetric molecule interfacial structure. We pull out the near surface properties such as density profile and stress profile of different temperatures and different surface potential to illustrate the interfacial structure and document it for the use of calculating phoretic motion.

Atom-based MD treat each atom in the simulation system as a point that holds mass but no rotational inertia, and each atom followed Newton's second law of motion. The forces between atoms can be from many different types of inter-atom potential, such as covalent bond, the Coulomb force, or the van der Walls force. Since all the inter-atomic force are considered to be conservative forces the inter-atomic potential can be assumed as $\boldsymbol{f}_{gh} = -\nabla_g \cdot \varphi_{gh}(r_{gh})$, where $\boldsymbol{f}_{gh}$ is the force of atom g take from atom h, ∇_g is the del operator for coordinate of atom g, and φ_{gh} is the potential between atom g and atom h ,which is a function of atom distance between atom g and atom h, r_{gh}. Thus Newton's second law of motion can be put as

$$\frac{d\boldsymbol{u}_g}{dt} = \frac{1}{m_g}\sum_{h\neq g}\boldsymbol{f}_{gh} = -\frac{1}{m_g}\nabla_g \cdot \sum_{h\neq g}\varphi_{gh}(r_{gh}) \tag{6.1}$$

where $\boldsymbol{u}_i$ and m_i are the velocity and mass of the atom i. Based on Eq. (6.1), MD simulation iterates the finite difference of time to predict the future profile of atom distribution.

We employed TIP3P water model (Jorgensen, Chandrasekhar et al. 1983) as an example for this chapter. TIP3P water model assumed the two hydrogen and oxygen atoms hold $0.417e$ and $-0.834e$ charge where e is the charge of one proton. The molecule structure is assumed to be elastic and relax at O-H bond distant of $r^{0\,(OH)} = 0.9572$ Å and the H-O-H angle

of $\theta^{0\,(HOH)} = 104.52°$. The elastic constant can be found in Table 6.1. The van der Waals force is approximated by the Lanard-Jones (L-J) potential that also can be found in Table 6.1.

Table 6-1 Simulation parameters of MD used in this chapter

Parameter	Value	Unit
O mass	15.9994	g/mol
H mass	1.008	g/mol
$\varepsilon_{\mathrm{O-O}}$, $\delta_{\mathrm{O-O}}$	0.1521, 3.1507	Kcal/mol, Å
$\varepsilon_{\mathrm{H-H}}$, $\delta_{\mathrm{H-H}}$	0.0460, 0.4000	Kcal/mol, Å
$\varepsilon_{\mathrm{O-H}}$, $\delta_{\mathrm{O-H}}$	0.0836, 1.7753	Kcal/mol, Å
K of O-H bond	450	Kcal/mol Å^2
K of H-O-H angle	55	Kcal/mol rad^2

The simulation box is drawn as a base of $35\ \text{Å} \times 35\ \text{Å}$ with a piston controlled height as shown in Figure 6-1. The piston is formed by a rigid group of atoms that only moves vertically, and it is evenly pushed down to represent one atmosphere pressure. There are 1500 water molecules in this box, which give approximately $10 \times 10 \times 15$ molecules for each dimension respectively. At the bottom of the simulation box, there is a L-J style 3-9 surface potential as $\Phi = \frac{\varepsilon}{2}\left(\left(\frac{\delta}{Z}\right)^9 - 3\left(\frac{\delta}{Z}\right)^3\right)$, where ε is the potential well depth, δ is the location of potential well, and Z is the distance apart from the surface. The potential is simplified by only acting on oxygen atoms, which is approximately the center of mass of a water molecule. The 3-9 surface potential is reduced from 6-12, the L-J potential, which represent the case of surface that is not charged. Horizontally the box is assumed to be periodically symmetric, thus the long range Coulomb force is simulated by PPPM method (Plimpton, Pollock et al. 1997). The time step used in the simulation is 0.5 fs. During the simulation, the atom velocity will be scaled each time step

according to the estimation of temperature as $Nk_BT = \frac{3}{2}\sum_g m_g {u_g}^2$ to fit the assigned simulation temperature, where N is for total number of atoms in the simulation box, k_B is the Boltzmann constant, and T is temperature. The simulation is set up and pre-run for 0.1 ns time steps for reaching the equilibrium and start to collect data for 1 ns time steps.

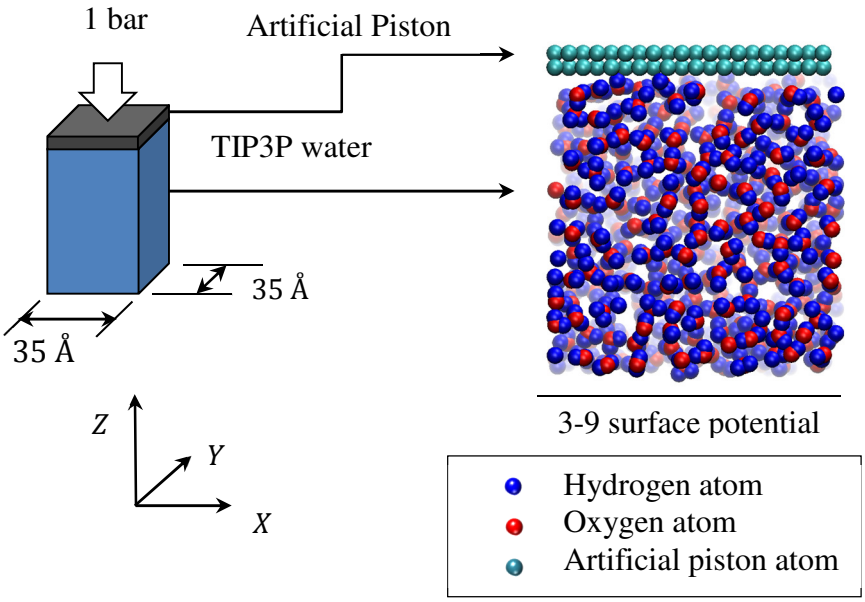

Figure 6-1 Simulation box of MD used in this chapter

The simulation results will be present as density field, interfacial body force field, and stress field. All three of them will be time averaged within the slab thickness of each $\Delta Z = 0.1$Å. The atom number density and mass density are defined as the sum of the atom count within the slab divided by the slab volume. The stress field is found by the sum of the per atom stress divided by the slab volume. The per atom stress can be found by (Sirk, Moore et al. 2013)

$$\sigma_{g;ij} = -m_g u_{g;i} u_{g;j} + \sum_{h=g}(r_{h;i} - r_{g;i}) f_{gh;j} \tag{6.2}$$

Note that per atom stress is in unit of pressure times volume, hence the dividing of slab volume as volumetric average. Finally the interfacial body force will be found by the differentiation of the stress at Z direction. Since the model is symmetric on the X and Y axis, the stress components of σ_{XY}, σ_{YZ}, and σ_{ZX} are zero. The components left are $\sigma_{XX} = \sigma_{YY}$, and σ_{ZZ}. The interfacial body force field can be found by

$$b_Z = -\sigma_{ZZ,Z}. \tag{6.3}$$

In Figure 6-2, we performed the simulation of how water reacts with different strength of interfacial potential strength. There are studies that indicate the interfacial potential strength can alter the hydrophobicity (Trudeau, Jena et al. 2009). Here we pick $\varepsilon = 0.55, 1.73, 5.5\ \mathrm{kJ/mol}$ as our study object, which have been indicated that should refer to hydrophobic, slightly hydrophobic, and slightly hydrophilic surfaces, respectively. The density profile is more aggregate to the surface when the surface potential is stronger, and the profile is pushed away when the temperature is higher in all the cases. The case of $\varepsilon = 1.73\ \mathrm{kJ/mol}$ shows a very special pattern that is slightly adsorbed at low temperature and pushed away at high temperature, which provide large density change in proportion comparing to the other two cases.

In Figure 6-3, we showed the simulation result of how water distributes with different potential well depth location. All the profiles in Figure 6-3 are subject to the same potential well depth, $\varepsilon = 1.73\ \mathrm{kJ/mol}$. Similar to Figure 6-2, all the profiles are pushed away when the temperature is higher. The feature of large density change seems not depend on the potential well location, thus it shows in all three different plots.

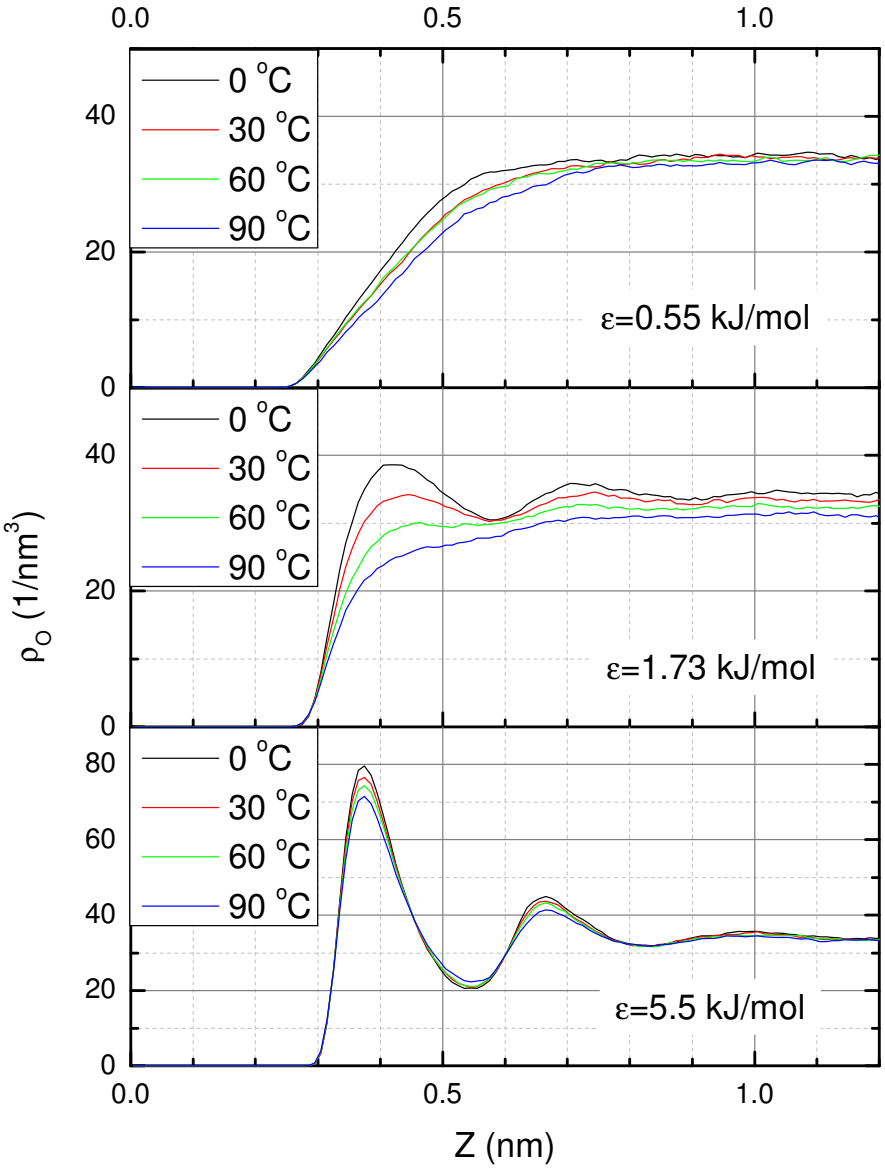

Figure 6-2 Atom number density of oxygen atom of water respond to different interfacial potential strength. All profile is subject to the same potential well location $\delta = 0.375$ nm.

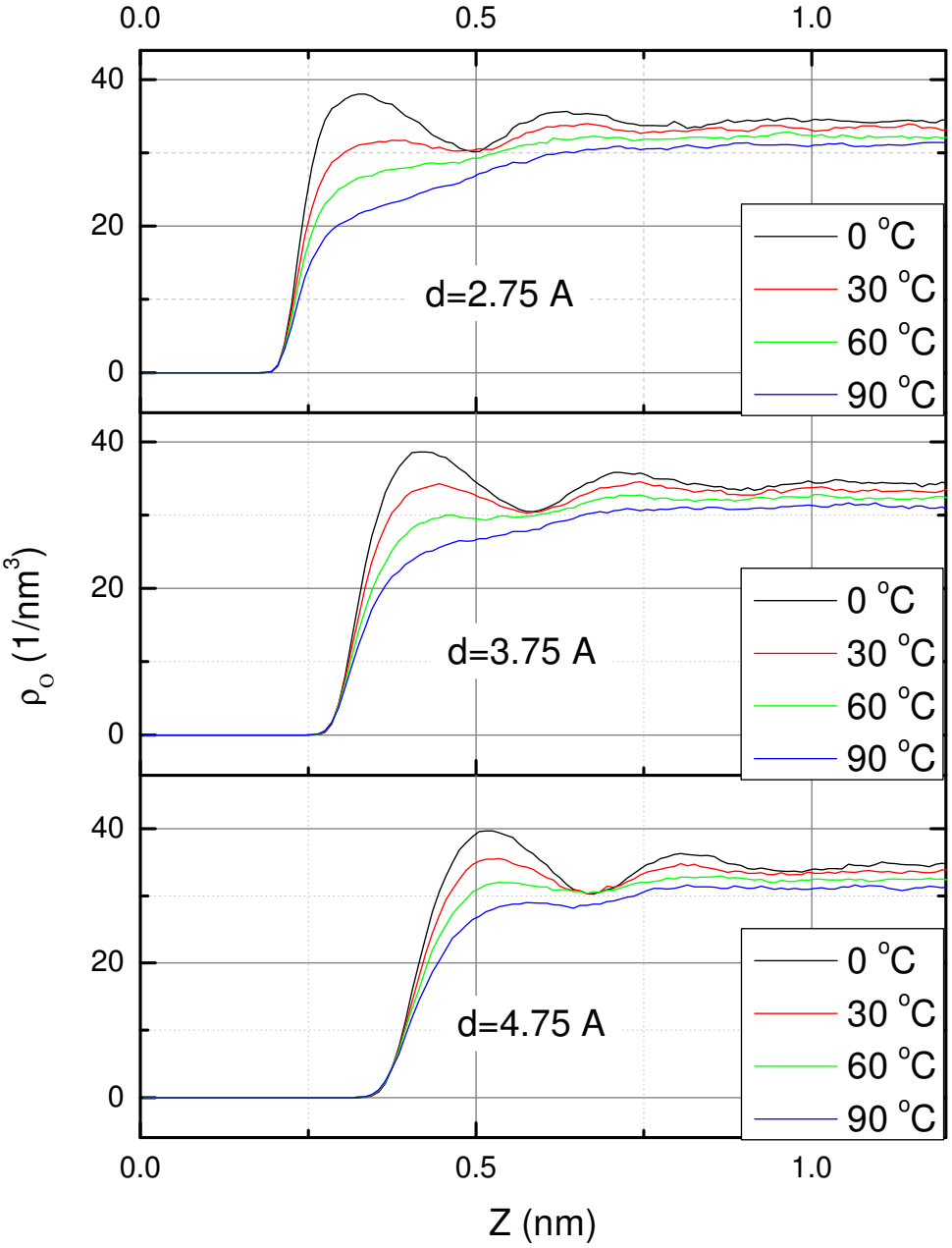

Figure 6-3 Atom number density of oxygen atom of water respond to different interfacial potential distances. All profile is subject to the same potential well depth location $\varepsilon = 1.73\ \mathrm{kJ/mol}$.

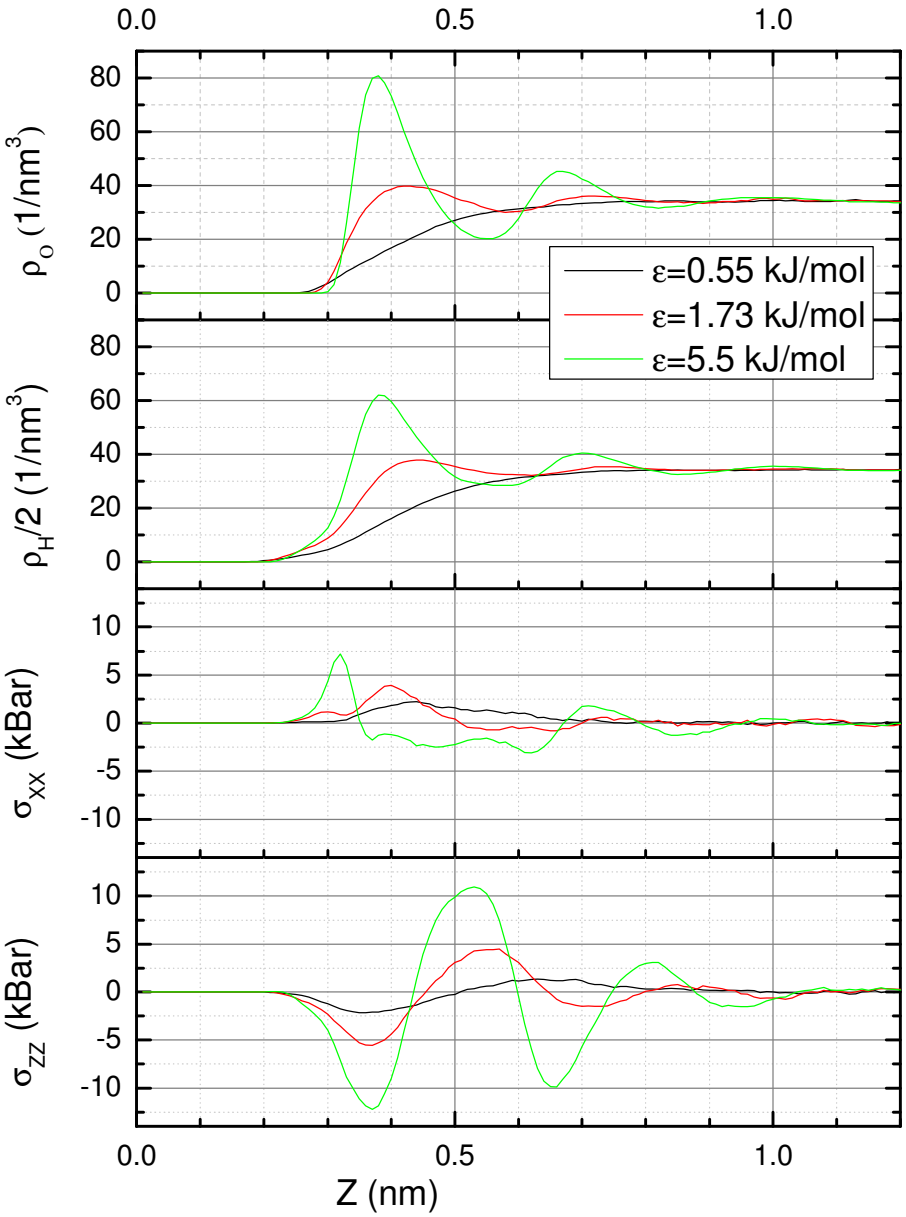

Figure 6-4 Atom number density and stress of different surface potential strengths, all profile is simulated with same potential well location $\delta = 0.375\ \mathrm{nm}$ and same temperature $T = 0℃$.

To look into the interfacial structure deeper, in Figure 6-4, we showed the atom number density of both oxygen atom and hydrogen atom with the profile of stress on normal and tangential direction. It is very clear that the peak of oxygen atom and hydrogen atom are mostly aligned, which means the water molecule near surface can be assume to be ordered laying down horizontal to the surface. The stress of normal direction is basically linear increasing with the increased potential strength, but the stress of tangential direction remains a similar scale.

6.2 Thermophoretic Speed with Considered Preloaded Stress

Considering the results from Section 6.1 as the preload condition, the thermophoretic speed can be solved by Eq. (3.16) as soon as we have the information of viscosity profile in each situation. However, at this stage, the effective time scale of viscosity of our interest is much larger than the simulation time scale of MD. Thus, even there are many research that provide viscosity by MD simulation, the skew rate is much larger than it should be. For example, a particle of size $1\ \mu\mathrm{m}$ moving at a speed of$1\ \mu\mathrm{m/s}$, the skew rate is $1\ /\mathrm{s}$. If we applying the skew rate into a $10\ \mathrm{nm}$ cubical simulation box, the top plate should move at the speed of $10\ \mathrm{nm/s}$, which take a million typical time step to travel through the box, thus the result will easily be covered by the statistical noise. To reach a valid result from MD, the skew ration must be at least a thousand times larger. Thus in this section, we just assume the viscosity profile is constant as a demonstration, which this demonstration is focusing on how much is the effect from the preloaded stress field comparing to the effect of interfacial body force field. We also assume the density profile to be uniform to even simplify the model and isolate the effect of preload stress field.

Starting from Eq. (3.16), here we rewrite the equation,

$$\widehat{\boldsymbol{F}}\cdot\boldsymbol{U}=\iiint_V\left(\widehat{\boldsymbol{u}}-\widehat{\boldsymbol{U}}\right)\cdot\boldsymbol{b}dV+\iiint_V\frac{\eta^{\infty}-\eta}{\eta}(\boldsymbol{\sigma}-\boldsymbol{\sigma}^0):\nabla\widehat{\boldsymbol{u}}dV-\iiint_V\boldsymbol{\sigma}^0:\nabla\widehat{\boldsymbol{u}}dV-\iiint_V\hat{p}\nabla\cdot\boldsymbol{u}dV. \quad (6.4)$$

Under the assumption of uniform viscosity and uniform density as we mentioned above, the equation can be reduced into

$$\widehat{\boldsymbol{F}} \cdot \boldsymbol{U} = \iiint_V \left(\widehat{\boldsymbol{u}} - \widehat{\boldsymbol{U}}\right) \cdot \boldsymbol{b} dV - \iiint_V \boldsymbol{\sigma}^0 : \nabla \widehat{\boldsymbol{u}} dV. \tag{6.5}$$

The isotropic pressure part of $\boldsymbol{\sigma}^0$ will have no effect since the uniform density of the auxiliary solution. The uniform density is leading the term $\boldsymbol{p}^0 : \nabla \widehat{\boldsymbol{u}} = p^0 \nabla \cdot \widehat{\boldsymbol{u}} = 0$, where $\boldsymbol{p}^0$ can be any isotropic pressure. In order to remove the direct effect of the interfacial body force, we deducted σ_{ZZ} to all three components. The deducted part will have no effect since it is isotropic. The stress after the deduction is ${\sigma_{ZZ}}^* = 0$, ${\sigma_{XX}}^* = {\sigma_{XX}}^0 - {\sigma_{ZZ}}^0$, and ${\sigma_{YY}}^* = {\sigma_{YY}}^0 - {\sigma_{ZZ}}^0$. We substituted $\nabla \widehat{\boldsymbol{u}} = \nabla\left(\widehat{\boldsymbol{u}} - \widehat{\boldsymbol{U}}\right)$ into the equation, which will make no difference to other terms since $\widehat{\boldsymbol{U}}$ is constant and will vanish during differentiation. By the chain rule of $\boldsymbol{\sigma}^0 : \nabla\left(\widehat{\boldsymbol{u}} - \widehat{\boldsymbol{U}}\right) = \nabla \cdot \left(\boldsymbol{\sigma}^0 \cdot \left(\widehat{\boldsymbol{u}} - \widehat{\boldsymbol{U}}\right)\right) - (\nabla \cdot \boldsymbol{\sigma}^0) \cdot \left(\widehat{\boldsymbol{u}} - \widehat{\boldsymbol{U}}\right)$, Eq. (6.5) can be reformed into

$$\widehat{\boldsymbol{F}} \cdot \boldsymbol{U} = \iiint_V \left(\widehat{\boldsymbol{u}} - \widehat{\boldsymbol{U}}\right) \cdot \boldsymbol{b} dV - \iint_S \boldsymbol{n} \cdot \boldsymbol{\sigma}^* \cdot \left(\widehat{\boldsymbol{u}} - \widehat{\boldsymbol{U}}\right) dS + \iiint_V (\nabla \cdot \boldsymbol{\sigma}^*) \cdot \left(\widehat{\boldsymbol{u}} - \widehat{\boldsymbol{U}}\right) dV. \tag{6.6}$$

One can find the second term of right hand side is zero because of the velocity on the surface equal to the particle speed. Here, we have the auxiliary solution of incompressible, Newtonian, and no-slip boundary condition as simplified version of Eqs. (3.17)-(3.19) as

$$\hat{u}_r = \widehat{U} \cos(\theta) \left(\frac{3a}{2r} - \frac{a^3}{2r^3}\right), \tag{6.7}$$

$$\hat{u}_\theta = -\widehat{U} \sin(\theta) \left(\frac{3a}{4r} + \frac{a^3}{4r^3}\right), \tag{6.8}$$

$$\hat{F} = 6\pi\eta^\infty a \widehat{U}, \tag{6.9}$$

By substitute Eqs. (6.7)-(6.9) into Eq. (6.6), we have

$$U = \frac{1}{6\pi\eta a} \iiint_V \left[\cos(\theta) \left(\frac{3a}{2r} - \frac{a^3}{2r^3} - 1\right) b_r - \sin(\theta) \left(\frac{3a}{4r} + \frac{a^3}{4r^3} - 1\right) {\sigma_{XX,X}}^*\right] dV \tag{6.10}$$

By separate the integral of radio direction and tangential direction, we have

$$U = \frac{1}{6\pi\eta a} \left[\iint_A \cos(\theta)\, dA \int_a^\infty \left(\frac{3a}{2r} - \frac{a^3}{2r^3} - 1\right) b_r \frac{r^2}{a^2} dr - \iint_A \sin(\theta)\, dA \int_0^\infty \left(\frac{3a}{4r} + \frac{a^3}{4r^3} - 1\right) {\sigma_{XX,X}}^* \frac{r^2}{a^2} dr\right]. \tag{6.11}$$

The first non-zero term of the Taylor expansion of $\frac{r^2}{a^2}\left(\frac{3a}{2r} - \frac{a^3}{2r^3} - 1\right)$ and $\frac{r^2}{a^2}\left(\frac{3a}{4r} + \frac{a^3}{4r^3} - 1\right)$ at $r = a$ is

$$\frac{r^2}{a^2}\left(\frac{3a}{2r}-\frac{a^3}{2r^3}-1\right)=-\frac{3}{2}\left(\frac{Z}{a}\right)^2+O\left(\left(\frac{Z}{a}\right)^3\right), \tag{6.12}$$

$$\text{and } \frac{r^2}{a^2}\left(\frac{3a}{4r}+\frac{a^3}{4r^3}-1\right)=-\frac{3}{2}\left(\frac{Z}{a}\right)+O\left(\left(\frac{Z}{a}\right)^2\right). \tag{6.13}$$

we have

$$U\cong\frac{1}{6\pi\eta a}\left[-\iint_A\cos(\theta)\,dA\int_0^\infty\frac{3}{2}\left(\frac{Z}{a}\right)^2 b_Z dZ+\iint_A\sin(\theta)\,dA\int_0^\infty\frac{3}{2}\left(\frac{Z}{a}\right)\sigma_{XX,X}{}^* dZ\right], \tag{6.14}$$

or the multipole form of

$$U\cong\frac{1}{6\pi\eta a}\left[-\iint_A\cos(\theta)\,dA\frac{3}{2a^2}M_2+\iint_A\sin(\theta)\,dA\frac{3}{2a}N_{1,X}\right], \tag{6.15}$$

$$\text{where } M_m=\int_0^\infty Z^m b_Z dZ \tag{6.16}$$

$$\text{and } N_m=\int_0^\infty Z^m\sigma_{XX}{}^* dZ. \tag{6.17}$$

Equation (6.17) is a general form of phoresis held an anisotropic pre load stress. For the case of thermophoresis, we assume a surface temperature profile of $T=a\cos\theta\,\nabla T$, and substitute it into Eq. (6.15) to get

$$\begin{aligned}\boldsymbol{U}&=\frac{1}{6\eta}\left(-3\int_0^\pi\cos^2(\theta)\sin(\theta)\,d\theta\,M_{2,T}-3\int_0^\pi\sin^3(\theta)\,d\theta N_{1,T}\right)\nabla T\\&=\frac{1}{3\eta}\left(-M_{2,T}-2N_{1,T}\right)\nabla T.\end{aligned} \tag{6.18}$$

With the definition of thermophoretic mobility, we have

$$\boldsymbol{U}=-D_T\nabla T=-(D_{T\,M2}+D_{T\,N1})\nabla T \tag{6.19}$$

$$\text{where } D_{T\,M2}=\frac{1}{3\eta}M_{2,T}=\frac{1}{3\eta}\int_0^\infty Z^2 b_{Z,T}dZ. \tag{6.20}$$

$$\text{and } D_{T\,N1}=\frac{2}{3\eta}N_{1,T}=\frac{2}{3\eta}\int_0^\infty Z\sigma_{XX,T}{}^* dZ \tag{6.21}$$

Here, if we put b_Z back to $\sigma_{ZZ}{}^0$ and do the integral by part, we can have

$$D_{T\,M2}=\frac{1}{3\eta}M_{2,T}=\frac{2}{3\eta}\int_0^\infty Z\sigma_{ZZ,T}{}^0 dZ, \tag{6.22}$$

which will be identical with the solution if we did not neglect the isotropic part of the preloaded stress.

The Eq. (6.22) showed how to convert the preloaded stress into thermophoresis mobility. However, due to the simulation time of MD is high. It is difficult to achieve a good data

of each temperature. Thus, we only probe the profile every $30℃$, and will only show the result without the partial differentiation of temperature.

We started with the surface potential of $\varepsilon = 0.55\text{kJ/mol}$ and $\delta = 0.375\ \text{nm}$. We integrated the stress result from MD from 0 to 1.2 nm to find M_2 and N_1. The result of M_2 and N_1 can be found in Figure 6-5. The estimated average $D_{T\,M2} = -1.23\ 10^{-11}\ \text{m/sK}$, average $D_{T\,N1} = 2.36\ 10^{-11}\ \text{m/sK}$, and average $D_T = -1.12\ 10^{-11}\ \text{m/sK}$ from the different of $0℃$ and $90℃$ with water density of $\eta = 0.001\ \text{Pa}\cdot\text{s}$. Please note that $D_{T\,M2}$ is minus in this case, which is rare. The result of M_2 and N_1 with the surface potential of $\varepsilon = 1.37\ \text{kJ/mol}$ and $\delta = 0.375\ \text{nm}$. can be found in Figure 6-6. The estimated average $D_{T\,M2} = 0.652\ 10^{-11}\ \text{m/sK}$, average $D_{T\,N1} = 1.12\ 10^{-11}\ \text{m/sK}$, and average $D_{T\,N1} = 1.78\ 10^{-11}\ \text{m/sK}$ with the same the same assumption of the case of $\varepsilon = 0.55\text{kJ/mol}$.

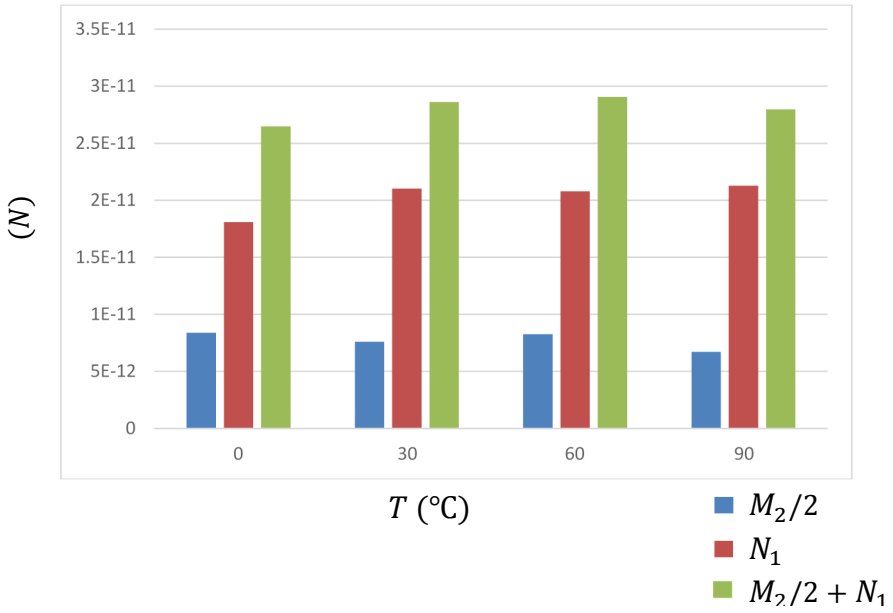

Figure 6-5 Force moments of the preloaded stress, M_2 and N_1 of $\varepsilon = 0.55\text{kJ/mol}$ and $\delta = 0.375\text{ nm}$

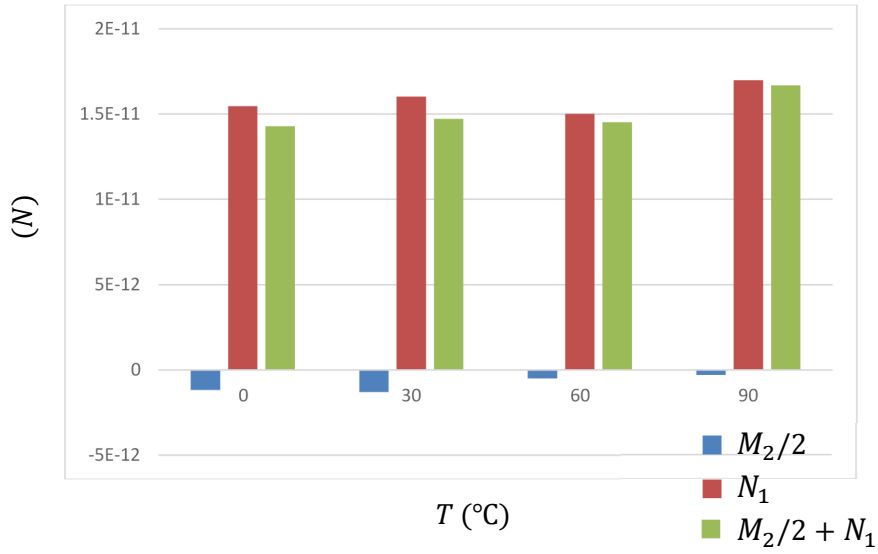

Figure 6-6 Force moments of the preloaded stress, M_2 and N_1 of $\varepsilon = 1.37\text{ kJ/mol}$ and $\delta = 0.375\text{ nm}$

6.4 Discussion

With the MD simulation, a more realistic picture of the near interfacial structure is shown. The near surface anisotropic stress, or so called surface tension, can contribute to the phoresis as the interfacial body force do at the normal direction. The simulation result showed a high variety of interfacial structure behaviors, which may involve the dependence of surface potential strength, surface potential shape, or bulk temperature. In most cases, stronger interfacial potential pull the water closer with a layer by layer structure with the water molecule lying down to the surface tangential direction. The weaker surface potential, on the other hand, tend to leave a larger surface depletion. This chapter constructed the phoretic equation with the anisotropic interfacial preload stress. With the analytical solution and the result of MD simulation, one can estimate the phoretic mobility.

Since the simulation is computational expensive, only two sets of simulation results showed in thermophoretic mobility with a large temperature gap between data. However, the method is still a systematic bottom-up approach that can provide a good insight of predicting phoretic mobility in the case of molecule ordering and large anisotropic interfacial surface.

Chapter 7

Conclusion

What we expect for a micro/nanoscale motor or robot is to reach the size scale that is way too small for human operation. Thus we expect it to move like our hands, which are expected to be fast, powerful, yet functionalized, and controllable. Through phoresis or self-phoresis, we can achieve the speed and strength that most other methods missed at small scale. However, to ensure the functionality and controllability, we have to deeply understand the underlying physics.

The key idea of this dissertation is that the non-contact force can induce flow. And since that flow is near surface, we may assume it only changes in magnitude, not charisma, when it interacts with the environment. As the result, most equations of phoresis can be broken down to a Taylor's expansion from the surface zero. This will allow us to reduce the unknown from a continuous function to few variables, such as viscosity function into slip length, or body force function into force multipole moments. This could increase the possibility of finding those parameter by experiments.

Through Chapter 4 to Chapter 6, one can find out that interfacial structure of the surrounding fluid acts as the link between the energy provided by the surrounding field and the particle mobility. For a car, this would be the piston and crank box, which translate the unbounded thermo energy into a one direction torque. It decides the charisma of this particle of phoresis. Thus, the question next is how we find more interfacial structures that can achieve better performance. This may involve the nanoscale fabrication of surface coating, such as monolayer coating, a meta-material particle, or a composition of fluid with multiple active ingredients.

Finally, the idea that interfacial body force can induce flow is not only applicable on phoresis. The counterpart, osmosis flow, can use the similar idea of this dissertation. Combining

them, there is a good picture of micor/nanoscale hydrodynamic that can be useful for the micro/nanoscale fluid system.

References

Chapter 8 Ajdari, A. and L. Bocquet (2006). "Giant amplification of interfacially driven transport by hydrodynamic slip: Diffusio-osmosis and beyond." Physical review letters **96**(18): 186102.

Chapter 9
Chapter 10 Anderson, J. L. and D. C. Prieve (1991). "Diffusiophoresis caused by gradients of strongly adsorbing solutes." Langmuir **7**(2): 403-406.

Chapter 11
Chapter 12 Argyris, D., N. R. Tummala, et al. (2008). "Molecular structure and dynamics in thin water films at the silica and graphite surfaces." The Journal of Physical Chemistry C **112**(35): 13587-13599.

Chapter 13
Chapter 14 Banigan, E. J., M. A. Gelbart, et al. (2011). "Filament depolymerization can explain chromosome pulling during bacterial mitosis." PLoS computational biology **7**(9): e1002145.

Chapter 15
Chapter 16 Baraban, L., M. Tasinkevych, et al. (2011). "Transport of cargo by catalytic Janus micro-motors." Soft Matter **8**(1): 48-52.

Chapter 17
Chapter 18 Basset, A. B. (1888). "On the motion of a sphere in a viscous liquid." Philosophical Transactions of the Royal Society of London. A: 43-63.

Chapter 19
Chapter 20 Bocquet, L. and E. Charlaix (2010). "Nanofluidics, from bulk to interfaces." Chemical Society Reviews **39**(3): 1073-1095.

Chapter 21
Chapter 22 Boguth, G., A. Harder, et al. (2000). "The current state of two-dimensional electrophoresis with immobilized pH gradients." Electrophoresis **21**(6): 1037-1053.

Chapter 23
Chapter 24 Braibanti, M., D. Vigolo, et al. (2008). "Does thermophoretic mobility depend on particle size?" Physical review letters **100**(10): 108303.

Chapter 25
Chapter 26 Chapman, D. L. (1913). "LI. A contribution to the theory of electrocapillarity." The London, Edinburgh, and Dublin Philosophical Magazine and Journal of Science **25**(148): 475-481.

Chapter 27

Chapter 28 Cooper, J. and R. Dooley (2008). Release of the IAPWS formulation 2008 for the viscosity of ordinary water substance, The International Association of the Properties of Water and Steam, Berlin, Germany.

Chapter 29
Chapter 30 Denbigh, K. and G. Raumann (1952). "The thermo-osmosis of gases through a membrane. II. Experimental." Proceedings of the Royal Society of London. Series A. Mathematical and Physical Sciences **210**(1103): 518-533.

Chapter 31
Chapter 32 Derjaguin, B., S. Dukhin, et al. (1972). "Capillary osmosis through porous partitions and properties of boundary layers of solutions." Journal of Colloid and Interface Science **38**(3): 584-595.

Chapter 33
Chapter 34 Derjaguin, B. V. (1987). Some results from 50 years' research on surface forces, Springer.

Chapter 35
Chapter 36 Dreyfus, R., J. Baudry, et al. (2005). "Microscopic artificial swimmers." Nature **437**(7060): 862-865.

Chapter 37
Chapter 38 Duhr, S. and D. Braun (2006). "Thermophoretic depletion follows Boltzmann distribution." Physical review letters **96**(16): 168301.

Chapter 39
Chapter 40 Ebbens, S. J. and J. R. Howse (2011). "Direct observation of the direction of motion for spherical catalytic swimmers." Langmuir **27**(20): 12293-12296.

Chapter 41
Chapter 42 Einstein, A. (1905). "UN THE MOVEMENT OF SMALL PARTICLES SUSPENDED IN STATIUNARY LIQUIDS REQUIRED BY THE MOLECULAR-KINETIC THEORY 0F HEAT."

Chapter 43
Chapter 44 Eslahian, K. A. and M. Maskos (2012). "Hofmeister effect in thermal field-flow fractionation of colloidal aqueous dispersions." Colloids and Surfaces A: Physicochemical and Engineering Aspects **413**: 65-70.

Chapter 45
Chapter 46 Ghosh, A. and P. Fischer (2009). "Controlled propulsion of artificial magnetic nanostructured propellers." Nano letters **9**(6): 2243-2245.

Chapter 47
Chapter 48 Gibbs, J. and Y.-P. Zhao (2009). "Autonomously motile catalytic nanomotors by bubble propulsion." Applied Physics Letters **94**(16): 163104-163104-163103.

Chapter 49

Chapter 50 Golestanian, R., T. Liverpool, et al. (2007). "Designing phoretic micro-and nano-swimmers." New Journal of Physics **9**(5): 126.

Chapter 51
Chapter 52 Goren, S. L. (1977). "Thermophoresis of aerosol particles in the laminar boundary layer on a flat plate." Journal of Colloid and Interface Science **61**(1): 77-85.

Chapter 53
Chapter 54 Happel, J. and H. Brenner (1983). Low Reynolds number hydrodynamics: with special applications to particulate media, Springer.

Chapter 55
Chapter 56 Helmholtz, H. v. (1853). "Ueber einige Gesetze der Vertheilung elektrischer Ströme in körperlichen Leitern mit Anwendung auf die thierisch-elektrischen Versuche." Annalen der Physik **165**(6): 211-233.

Chapter 57
Chapter 58 Ibele, M., T. E. Mallouk, et al. (2009). "Schooling Behavior of Light-Powered Autonomous Micromotors in Water." Angewandte Chemie International Edition **48**(18): 3308-3312.

Chapter 59
Chapter 60 Irving, J. and J. G. Kirkwood (1950). "The statistical mechanical theory of transport processes. IV. The equations of hydrodynamics." The Journal of Chemical Physics **18**(6): 817-829.

Chapter 61
Chapter 62 Israelachvili, J. N. (2011). Intermolecular and surface forces: revised third edition, Academic press.

Chapter 63
Chapter 64 Jaffe, L. F., K. R. Robinson, et al. (1974). "LOCAL CATION ENTRY AND SELF-ELECTROPHORESIS AS AN INTRACELLULAR LOCALIZATION MECHANISM*." Annals of the New York Academy of Sciences **238**(1): 372-389.

Chapter 65
Chapter 66 Jorgensen, W. L., J. Chandrasekhar, et al. (1983). "Comparison of simple potential functions for simulating liquid water." The Journal of Chemical Physics **79**(2): 926-935.

Chapter 67
Chapter 68 Lauga, E., M. Brenner, et al. (2007). "Microfluidics: the no-slip boundary condition." Springer handbook of experimental fluid mechanics: 1219-1240.

Chapter 69
Chapter 70 Luo, H. and C. Pozrikidis (2008). "Effect of surface slip on Stokes flow past a spherical particle in infinite fluid and near a plane wall." Journal of Engineering Mathematics **62**(1): 1-21.

Chapter 71
Chapter 72 Maxwell, J. C. (1879). "On stresses in rarified gases arising from inequalities of temperature." Philosophical Transactions of the royal society of London **170**: 231-256.

Chapter 73
Chapter 74 Mezger, M., H. Reichert, et al. (2006). "High-resolution in situ x-ray study of the hydrophobic gap at the water–octadecyl-trichlorosilane interface." Proceedings of the National Academy of Sciences **103**(49): 18401-18404.

Chapter 75
Chapter 76 Morris, D. L., L. Hannon, et al. (1992). "Slip length in a dilute gas." Physical review A **46**(8): 5279.

Chapter 77
Chapter 78 Morthomas, J. and A. Würger (2009). "Thermophoresis at a charged surface: the role of hydrodynamic slip." Journal of Physics: Condensed Matter **21**(3): 035103.

Chapter 79
Chapter 80 Navier, C. (1823). "Mémoire sur les lois du mouvement des fluides." Mémoires de l'Académie Royale des Sciences de l'Institut de France **6**: 389-440.

Chapter 81
Chapter 82 Paxton, W. F., A. Sen, et al. (2005). "Motility of catalytic nanoparticles through self-generated forces." Chemistry-A European Journal **11**(22): 6462-6470.

Chapter 83
Chapter 84 Platten, J. K. (2006). "The Soret effect: a review of recent experimental results." Journal of applied mechanics **73**(1): 5-15.

Chapter 85
Chapter 86 Plimpton, S. (1995). "Fast parallel algorithms for short-range molecular dynamics." Journal of computational physics **117**(1): 1-19.

Chapter 87
Chapter 88 Plimpton, S., R. Pollock, et al. (1997). Particle-Mesh Ewald and rRESPA for Parallel Molecular Dynamics Simulations. PPSC, Citeseer.

Chapter 89
Chapter 90 Pohl, H. A. and H. Pohl (1978). Dielectrophoresis: the behavior of neutral matter in nonuniform electric fields, Cambridge university press Cambridge.

Chapter 91
Chapter 92 Poynor, A., L. Hong, et al. (2006). "How water meets a hydrophobic surface." Physical review letters **97**(26): 266101.

Chapter 93
Chapter 94 Pretorius, V., B. Hopkins, et al. (1974). "Electro-osmosis: A new concept for high-speed liquid chromatography." Journal of Chromatography A **99**: 23-30.

Chapter 95
Chapter 96 Purcell, E. M. (1977). "Life at low Reynolds number." Am. J. Phys **45**(1): 3-11.

Chapter 97
Chapter 98 Roegiers, F., A. McDougall, et al. (1995). "The sperm entry point defines the orientation of the calcium-induced contraction wave that directs the first phase of cytoplasmic reorganization in the ascidian egg." Development **121**(10): 3457-3466.

Chapter 99
Chapter 100 Sen, A., M. Ibele, et al. (2009). "Chemo and phototactic nano/microbots." Faraday discussions **143**: 15-27.

Chapter 101
Chapter 102 Sendner, C., D. Horinek, et al. (2009). "Interfacial water at hydrophobic and hydrophilic surfaces: Slip, viscosity, and diffusion." Langmuir **25**(18): 10768-10781.

Chapter 103
Chapter 104 Sengers, J. and B. Kamgar-Parsi (1984). "Representative equations for the viscosity of water substance." Journal of physical and chemical reference data **13**(1): 185-205.

Chapter 105
Chapter 106 Sirk, T. W., S. Moore, et al. (2013). "Characteristics of thermal conductivity in classical water models." The Journal of Chemical Physics **138**(6): 064505.

Chapter 107
Chapter 108 Swan, J. W. and A. S. Khair (2008). "On the hydrodynamics of 'slip–stick'spheres." Journal of fluid mechanics **606**: 115-132.

Chapter 109
Chapter 110 Talbot, L., R. Cheng, et al. (1980). "Thermophoresis of particles in a heated boundary layer." Journal of fluid mechanics **101**(04): 737-758.

Chapter 111
Chapter 112 Tanaka, H. (2000). "Simple physical model of liquid water." The Journal of Chemical Physics **112**(2): 799-809.

Chapter 113
Chapter 114 Tiselius, A. (1937). "A new apparatus for electrophoretic analysis of colloidal mixtures." Transactions of the Faraday Society **33**: 524-531.

Chapter 115
Chapter 116 Tretheway, D. C. and C. D. Meinhart (2002). "Apparent fluid slip at hydrophobic microchannel walls." Physics of Fluids (1994-present) **14**(3): L9-L12.

Chapter 117
Chapter 118 Trudeau, T. G., K. C. Jena, et al. (2009). "Water structure at solid surfaces of varying hydrophobicity." The Journal of Physical Chemistry C **113**(46): 20002-20008.

Chapter 119
Chapter 120 Ünlü, M., M. E. Morgan, et al. (1997). "Difference gel electrophoresis. A single gel method for detecting changes in protein extracts." Electrophoresis **18**(11): 2071-2077.

Chapter 121
Chapter 122 Vigolo, D., G. Brambilla, et al. (2007). "Thermophoresis of microemulsion droplets: Size dependence of the Soret effect." Physical Review E **75**(4): 040401.

Chapter 123
Chapter 124 Wang, W., W. Duan, et al. (2013). "Small power: Autonomous nano-and micromotors propelled by self-generated gradients." Nano Today **8**(5): 531-554.

Chapter 125
Chapter 126 Würger, A. (2007). "Thermophoresis in colloidal suspensions driven by Marangoni forces." Physical review letters **98**(13): 138301.

Chapter 127
Chapter 128 Würger, A. (2013). "Is Soret equilibrium a non-equilibrium effect?" Comptes Rendus Mécanique **341**(4): 438-448.

Chapter 129
Chapter 130 Zhang, L., J. J. Abbott, et al. (2009). "Characterizing the swimming properties of artificial bacterial flagella." Nano letters **9**(10): 3663-3667.

Chapter 131

Chapter 132

Biographical Information

Yuan Ting Wu was born in Taipei, Taiwan. He received his Bachelor of Science degree in Mechanical Engineering from National Chiao Tung University in 2007. After one year working as a thermo-fluid engineer at Janmao Inc., he decided to go to the United State to pursue his graduate education. He received his Master of Science degree in Mechanical Engineering from Florida Institute of Technology in 2011. Immediately after that, he went to University of Texas at Arlington for his Ph.D degree.